

Charged Kaons at the Main Injector

April 15, 1998

A Proposal for a Precision Measurement of the Decay $K^+ \rightarrow \pi^+ \nu \bar{\nu}$ and Other Rare K^+ Processes at Fermilab Using the Main Injector

R. Coleman, P.S. Cooper*, M. Crisler, C. Milstene[†], E. Ramberg, R. S. Tschirhart
Fermi National Accelerator Laboratory, Batavia, IL, USA

A. Kohzevnikov, V. Kubarovsky, V. Kurshetsov, L. Landsberg, V. Molchanov, V. Obraztsov, V. Polyakov,
D. Vavilov, O. Yushchenko
Institute of High Energy Physics, Serpukhov, Russia

J. Engelfried, A. Morelos
Instituto de Fisica, Universidad Autonoma de San Luis Potosi, Mexico

K. Lang, J.L. Ritchie*
University of Texas at Austin, Austin, Texas 78712

[†] Resident at Fermilab, on leave from Tel Aviv University.

* Cospokesmen: P.S. Cooper, pcooper@fnal.gov, (630) 840-2629
J.L. Ritchie, ritchie@hep.utexas.edu, (512) 471-4488

1st edition submitted to Fermilab April 15, 1998

SUMMARY

We are proposing here an experiment to measure the branching ratio of the ultra-rare charged kaon decay $K^+ \rightarrow \pi^+ \nu \bar{\nu}$ by observing a large sample of $K^+ \rightarrow \pi^+ \nu \bar{\nu}$ decays with small background. Our physics goal is to measure the magnitude of the Cabibbo, Kobayashi, Maskawa matrix element V_{td} with a statistical precision of about 5% based upon a ~ 100 event sample with total backgrounds of less than 10 events. This decay mode is known to be theoretically clean. The only significant theoretical uncertainty in the calculation of this branching ratio is due to the charm contribution. A 10% measurement of the branching ratio will yield a 10% total uncertainty on the magnitude of V_{td} .

The experimental technique we are proposing is decay in flight in a ~ 22 GeV/c RF separated K^+ beam with a kaon flux of 30 MHz and a purity of higher than 70% K^+ generated with about 5×10^{12} 120 GeV/c protons per spill from the Main Injector. The detector will have redundant measurements for both the K^+ and π^+ with conventional high rate magnetic spectrometers and velocity spectrometers based on phototube ring imaging Cherenkov counters for each particle. A hermetic photon veto system capable of rejecting π^0 decays with an inefficiency less than 2×10^{-7} and a muon range stack capable of rejecting μ^+ with an inefficiency less than 1×10^{-5} are also required. The expected signal acceptance of this apparatus after all cuts will be $\sim 1\%$. A data collection period of 2 years should yield a ~ 100 event signal over a background of less than 10 events assuming a branching ratio of 1×10^{-10} .

This new experiment is known as “Charged Kaons at the Main injector”, or “**CKM**”.

Contents

1	Introduction	12
2	The CKM Physics Program	12
2.1	$K^+ \rightarrow \pi^+ \nu \bar{\nu}$ Theory	12
2.2	Physics reach on the $\bar{\rho} - \bar{\eta}$ plane of $K^+ \rightarrow \pi^+ \nu \bar{\nu}$	13
2.3	Related K_L^0 and B-system Measurements and Theory	14
2.4	Other K^+ Physics	16
2.4.1	$K^+ \rightarrow \mu^+ \nu_\mu \gamma$ Form Factor Measurement	17
2.4.2	$K^+ \rightarrow \pi^+ e^+ e^-$, $K^+ \rightarrow \pi^+ \mu^+ \mu^-$ Form Factor/Branching Ratio Measurements	18
2.4.3	Nonleptonic Charged Kaon decays and the Search for Direct CP Violation in K^\pm decays	18
2.4.4	Measurement of V_{us} from $K^+ \rightarrow \pi^0 e^+ \nu$ and $K^+ \rightarrow \pi^0 \mu^+ \nu$ decays	20
3	The Experimental Method	21
3.1	Experimental Overview	21
3.2	Background Sources	21
3.3	Beam Issues	24
3.4	Detector Requirements	25
3.4.1	The Momentum Spectrometer	25
3.4.2	The Velocity Spectrometer	26
3.4.3	The Kaon Entrance Angle Tracker System (KEAT)	27
3.4.4	The Beam Interaction Veto System (BIVS)	27
3.4.5	The Photon Veto Systems	28
3.4.6	The Muon Veto System	29
3.5	Stopped versus In-flight Kaon Decays	31
4	The Separated Charged Kaon Beam	34
4.1	Design Motivations of the Separated Beam	34
4.2	Design Motivations for a Debunched Beam	34
4.3	K^+ Flux and $K^+ / (\pi^+, p^+)$ ratio estimates	36
4.4	Motivation and Issues for Negative Beam Operation	36
4.5	Comparison to other RF separated beams	36
4.6	Overview of the 3-stage Design	37
4.6.1	Stage-1: Collection and Optics Preparation	37
4.6.2	Stage-2: RF Separation	37
4.6.3	Stage-3: Transport to the Experiment	37
4.7	The Superconducting RF separator system	38
4.8	Beam Line Muon and Separator Backgrounds	38
5	The Detector Systems	44
5.1	Instrumentation Overview of Detector Systems	44
5.2	The Upstream Magnetic Spectrometer	44
5.3	The Kaon RICH	47
5.3.1	Experience from the SELEX RICH	47
5.3.2	The Kaon RICH	47
5.3.3	Effect of Dispersion on the Resolution Function	49
5.3.4	Kaon RICH readout system	51

5.4	The Kaon Entrance Angle Tracker System	52
5.5	The Beam Interaction Veto System	52
5.6	The Vacuum Decay Vessel	53
5.7	The Vacuum Veto System	54
5.8	The Downstream Magnetic Spectrometer	57
5.9	The Pion RICH	60
5.9.1	Pion RICH readout system	62
5.10	The Forward Veto-Calorimeter System	62
5.10.1	The H1/HERA SPACAL Calorimetry	62
5.10.2	The PHENIX SHASHLIK Calorimetry	64
5.11	The Muon Veto System	65
5.12	The Beam Kicker Veto System	66
5.13	The Beam Dump	66
6	The Trigger and Data Acquisition Systems	66
6.1	The Trigger System	66
6.2	The Candidate Readout Frontends	68
6.2.1	SVX-3 Silicon Readout	68
6.2.2	The TMC TDC Pipeline System	69
6.2.3	CMS HCAL QIE readout system	69
6.3	The Data Acquisition System	69
6.4	Detector Performance Monitoring	71
7	Simulation Results	71
7.1	Monte Carlo Overview	72
7.2	$K^+ \rightarrow \pi^+ \nu \bar{\nu}$ Acceptance	74
7.3	Kaon Decay Backgrounds	81
7.3.1	$K^+ \rightarrow \pi^+ \pi^0$ Background Study	81
7.3.2	$K^+ \rightarrow \mu^+ \nu_\mu$	84
7.3.3	$K^+ \rightarrow \mu^+ \nu_\mu \gamma$ Background Study	90
7.4	Photon loss mechanisms in detector material	90
7.5	Beam-Detector Interaction Backgrounds	91
7.5.1	Charge-Exchange	91
7.5.2	Other Interactions in Detectors	94
7.5.3	Beam Gas Interactions	95
7.6	Accidental Background Sources	95
7.7	Background Summary	96
8	Cost, Schedule and Staffing Estimates	97
8.1	Costs	97
8.1.1	Beam Time Stamp System Costs	97
8.1.2	Upstream Magnetic Spectrometer Costs	98
8.1.3	Kaon RICH Costs	98
8.1.4	Kaon Entrance Angle Tracker Costs	98
8.1.5	Beam Interaction Veto System and Vacuum Veto System Costs	98
8.1.6	Downstream Magnetic Spectrometer Costs	100
8.1.7	Pion RICH Costs	100
8.1.8	Forward Veto System (Shashlik) Costs	100

8.1.9	Conversion Veto Plane Costs	101
8.1.10	Muon Veto System Costs	101
8.1.11	Hole Veto System, SHASHLIK design, Costs	101
8.1.12	Summary of Detector Cost Estimates	101
8.1.13	Fermilab Facility Cost Estimates	104
8.2	Milestones	105
8.2.1	First stage (physics) approval — 0.5 years	105
8.2.2	Second stage (technical and budgetary) approval — 1.5 year	105
8.2.3	Experiment construction — 2 years	105
8.2.4	Engineering run — 0.5 years	105
8.2.5	Data taking — 2 years	105
8.2.6	Analysis and publication — 1.5 years	106
8.3	Staffing	106
9	Conclusion	106
10	Acknowledgements	107

List of Figures

1	The ideal Unitarity Triangle. For illustrative reasons the value of $\bar{\eta}$ has been chosen to be higher than the fitted central value (reproduced from [13]).	14
2	A possible outcome from measurements of $K^+ \rightarrow \pi^+ \nu \bar{\nu}$, $K_L \rightarrow \pi^0 \nu \bar{\nu}$ and $B^0 \rightarrow \psi K_s^0$. The hashed annulus indicates the statistical precision of a 100 event measurement, and the total band indicates the combined statistical and theoretical errors.	15
3	Decay angle versus momentum for $K^+ \rightarrow \pi^+ \nu \bar{\nu}$ events. Three distinct analysis regions are shown.	23
4	Ring Radii for K^+ and π^+ versus their momentum for the kaon RICH system that measures the incident beam K^+ momentum and decay angle. The black band indicates the momentum resolution of the kaon RICH system described later in section 5.3. Assumed is $R = 40$ m and $n = 1.0002765$	28
5	Schematic layout of the beam line, distances in meters, reproduced from [46].	34
6	Beam envelopes for the CP/T beam. The tune of the CKM beam is the same until RF4. The apertures of the beam line elements are indicated, distances are in meters. Reproduced from [46].	35
7	(a) Vertical beam spot at the beam stopper. (b,linear) (c,log) The transmission as function of the width of the stopper (nominally 10 mm), for the CKM beam. Reproduced from [46].	39
8	Beam profiles and beam divergence at the entrance of the CKM decay volume. Reproduced from [46].	40
9	The beam momentum distribution at the entrance of the CKM decay volume. Reproduced from [46].	41
10	The CKM Detector.	42
11	Track averaged performance of a typical silicon plane in the SELEX beam tracking system over a 40-day period. The upper left figure plots the pedestal width as a function of time. The upper right figure plots the single track efficiency, and the lower left figure plots the noise readout occupancy for the nominal strip readout threshold. The lower right figure demonstrates the alignment stability over the 40 day period.	45
12	Ring radius distribution in the SELEX RICH for multi track events for tracks with momentum between 95 and 105 GeV/c. We fit a Gaussian to the pion peak of this distribution [68].	48
13	Fitted sigma of the proton ring radius distribution versus the mean radius. These fitted sigmas are larger than the 4.6 mm since they include finite track resolution and hits from overlapping rings.	49
14	Measured ring radius distribution from the SELEX prototype RICH.	50
15	left: Number of detectable photons. right: Distribution of detected photons in the kaon RICH focal plane for 1000 beam K^+ and 1000 beam π^+ events Overlaid is a proposed arrangement of the photomultipliers; 549 photomultipliers are plotted.	51
16	Possible schematic of the kaon RICH optical path. The vessel drawn has a total length of 11 m. The long arrow represents the beam; the thicker dots are the beam windows. The dashed line represents Cherenkov photons generated by a K^+ , dotted line Cherenkov photons from a π^+ . The flat mirror in the beam will only reflect part of the Cherenkov photons from the pions.	52
17	The momentum resolution of the Kaon RICH as a function of the lowest detected wavelength for different gases.	53

18	The absorption and emission spectra of the two dyes proposed for the KAMI/CKM photon veto detectors. The first dye will be used in the scintillator and the second dye will be used as a wavelength shifter in the fibers. Reproduced from [41].	54
19	GEANT results of the photon detection inefficiency of the vacuum veto counters. The top two plots show the inefficiency as a function of photon energy, for various photo electron thresholds and lead sheet thicknesses. The bottom two plots show the average inefficiency for photons below 20 MeV as a function of the lead sheet tilt angle. Reproduced from [41].	56
20	Measured photon detection inefficiency as a function of energy in lead-scintillator detectors from Ref. [42].	57
21	Schematic of a typical injection molded scintillator plate. Reproduced from [41]. . .	59
22	The functional relationship between the ring radius and the π^+ track momentum. The shaded band is the accepted momentum range. The black stripe is a 1- σ band that illustrates the momentum-radius transfer function.	61
23	Pion (a) fractional RICH momentum resolution and (b) RICH angular resolution as a function of pion momentum from the pion RICH velocity spectrometer measurements. Contributions to the resolutions from optical dispersion and multiple Coulomb scattering in the Neon radiator gas and phototube size, are included. Downstream magnetic spectrometer (DMS) (c) fraction momentum resolution and (d) angular resolution as a function of pion momentum. Contributions to the resolutions from tracking resolution and multiple Coulomb scattering in the tracker are included. . .	63
24	The KTeV Data Acquisition System.	70
25	The resolution in missing mass squared in $K^+ \rightarrow \pi^+ \pi^0$ decays for the three methods of determining it as described in the text. About 20,000 events are shown.	75
26	Distance between measured vertex location and actual decay position in $K^+ \rightarrow \pi^+ \nu \bar{\nu}$ events. The fitted resolution sigma is ~ 18 cm, with non-Gaussian tails originating from hard scatters included in the tracking simulation.	77
27	Measured distance of closest approach (<i>DOCA</i>) for the K^+ and π^+ in $K^+ \rightarrow \pi^+ \nu \bar{\nu}$ events. 78	
28	Difference in measured missing mass squared from the momentum and velocity measurements ($M_{\text{magnetic}}^2 - M_{\text{RICH}}^2$) for $K^+ \rightarrow \pi^+ \nu \bar{\nu}$ events.	79
29	Measured missing mass squared (M_{combined}^2) in $K^+ \rightarrow \pi^+ \nu \bar{\nu}$ events. The signal region is shaded.	80
30	Missing mass squared (M_{combined}^2) for $K^+ \rightarrow \pi^+ \pi^0$ events passing all cuts superimposed on the signal (light shading). The sensitivity shown in this plot corresponds to the experimental sensitivity of 72 $K^+ \rightarrow \pi^+ \nu \bar{\nu}$ events in our mass window (single event sensitivity of 1.4×10^{-12}) which are indicated with the dark shading.	83
31	Missing mass of $K^\pm \rightarrow \mu^\pm \nu_\mu$ decays where the muon is reconstructed under the pion mass hypothesis.	85
32	A GEANT simulation of a common Dalitz decay topology where the electron and positron tracks are kicked out of the photon veto system coverage by the 200 MeV/ c p_T -kick magnet. Fortunately the rejection of the remaining photon together with the low Dalitz decay branching fraction set the scale of this problem topology to be low at the outset.	86

33	A typical GEANT event where one of the decay $K^+ \rightarrow \pi^+\pi^0$ photons converts in the pion RICH gas. Photons are dot-trajectories and charged particles are dashed-trajectories. The photon entering the pion RICH volume is seen to convert in the neon gas, and the charged pion (lower track) produces a hard delta-ray in the neon gas as well.	88
34	The location of 10,000 hadronic interactions in beamline material. In the z scale of this figure (not the same as figure 10) the beam RICH spans the range $-14\text{ m} < z < -4\text{ m}$, with the mirror located at $z = -4\text{ m}$. The two beam vacuum trackers are located at $z = -2\text{ m}$ and $z = 0$	93

List of Tables

1	Theoretical Predictions and Experimental status	18
2	Theoretical predictions, world data and CKM potential for observing CP Asymmetries in charge kaon non-leptonics decays	19
3	Kaon decay modes which are potential backgrounds to $K^+ \rightarrow \pi^+ \nu \bar{\nu}$ in each of the three regions, defined in the text. The list is not exhaustive and includes only modes with relatively large branching ratios.	24
4	Required inefficiency performance of the CKM photon veto systems.	29
5	Required inefficiency performance of the KAMI photon veto systems.	30
6	Rates, occupancies and integrated material for several candidate upstream tracking technologies. Maximum cell occupancies are scaled to an incident beam rate of 51 MHz spread evenly over a 5 cm diameter beam region. The 51 MHz rate is the sum of 30 MHz K^+ , 15 MHz π^+ , and 6 MHz of upstream decays and interactions.	46
7	Some properties of radiator gases considered for the Kaon RICH.	52
8	Sampling ratio and total depth (in radiation lengths and nuclear interaction lengths) of vacuum veto counters for various angle of incidence photons. Reproduced from [41].	55
9	Comparison of the KAMI/CKM vacuum veto counters with photon veto counters from KTeV and BNL-E787. Reproduced from [41]	58
10	Comparison of scintillator used by D0, MINOS and KAMI/CKM, reproduced from [41].	58
11	Rates, occupancies and integrated material for fiber and straw tracking technologies. Maximum cell occupancies are scaled to an incident beam rate of 53 MHz spread evenly over a 5 cm diameter beam region. The 53 MHz rate is the sum of 24 MHz K^+ , 15 MHz of beam π^+ , 6 MHz of K^+ decay pions and muons, and 8 MHz of upstream decays and interactions.	60
12	Performance Summary of the H1 SPACAL Backward Calorimeter.	64
13	Performance Summary of the SHASHLIK prototype calorimeter	65
14	GEANT study of muon efficiency and pion acceptance (10 GeV) for a simple structure of 12 iron slabs, each 8.5 cm thick interleaved with 12 scintillator planes. The simple algorithm employed here is using the penetration depth in the range stack as the only discriminant. (Simulation with an algorithm based on shower length achieves a muon efficiency of less than 1×10^{-5} for a pion acceptance of 95%).	66
15	Level-1 trigger sources.	67
16	Level-1 trigger rates.	68
17	Comparison of estimated CKM data acquisition requirements and what has been achieved by KTeV and SELEX.	70
18	Parameters used in the Monte Carlo detector simulation.	73
19	Miscellaneous inefficiency table.	81
20	Background estimates in terms of effective branching ratio.	97
21	Cost Breakdown of the Beam Time Stamp System.	98
22	Cost Breakdown for the Upstream Magnetic Spectrometer.	98
23	Cost Breakdown for the Kaon RICH.	99
24	Cost Breakdown for the Kaon Entrance Angle Tracker.	99
25	Cost Breakdown for the Beam Interaction Veto System.	99
26	Cost Breakdown for the Vacuum Veto System.	100
27	Cost Breakdown of the Downstream Magnetic Spectrometer System.	100
28	Cost Breakdown for the pion RICH.	101
29	Cost Breakdown for the Forward Veto System, (assuming Shashlik).	101

30	Cost Breakdown of the Conversion Veto Plane System.	102
31	Cost Breakdown for the Muon Veto System.	102
32	Cost Breakdown for the Hole Veto System.	102
33	Cost estimate of the CKM detector systems.	103

1 Introduction

We are proposing here an experiment to measure the branching ratio of the ultra-rare charged kaon decay $K^+ \rightarrow \pi^+ \nu \bar{\nu}$ by observing a large sample of $K^+ \rightarrow \pi^+ \nu \bar{\nu}$ decays with small background. Our physics goal is to measure the magnitude of the Cabibbo, Kobayashi, Maskawa matrix element V_{td} with a statistical precision of about 5% based upon a 100 event sample. This measurement will play a critical role in testing the Standard Model hypothesis that the sole source of CP violation in nature resides in the imaginary parts of the V_{td} and V_{ub} Cabibbo, Kobayashi, Maskawa matrix elements. Attacking this question in the kaon sector is both experimentally and theoretically independent of the ongoing programs to measure these same parameters in the B meson sector. Each sector provides an independent test of the Standard Model description of CP violation. Both must measure the same parameters for that description to be correct. Such a parallel approach is critical to confirm, with confidence, both the Standard Model description of CP violation and the veracity of the individual measurements.

The $K^+ \rightarrow \pi^+ \nu \bar{\nu}$ decay mode is the theoretically cleanest laboratory in which to measure the magnitude of V_{td} [1]. The calculation of this decay rate is relative to the $K^+ \rightarrow \pi^0 e^+ \nu$ decay mode. This cancels uncertainties due to the hadronic structure of the $K^+ \rightarrow \pi^+ X$ transition. Long distance contributions to this decay have been calculated [2] [3] [4] [5] to be negligible. The only significant uncertainty in the relationship between the branching ratio and $|V_{td}|$ is a small contribution from the charmed quark which depends upon the poorly known charmed quark mass.

Evidence for this decay mode has recently been published [6] by experiment E787 at Brookhaven National Laboratory (BNL). They reported the observation of one event with an expected background of 0.08 ± 0.03 events and quote a branching ratio of $[4.2^{+9.7}_{-3.5}] \times 10^{-10}$ based on one good year of data taking at BNL. This branching ratio is consistent with the current prediction [1] of $[0.9 \pm 0.3] \times 10^{-10}$. The next important step is a measurement of this rate with sufficient precision to quantitatively challenge the Standard Model interpretation of the source of CP violation. That is the goal of this experiment. The design of our experiment has benefited enormously from the BNL E787 achievement, which has shown that all physics backgrounds to the 10^{-11} level have been identified and can be controlled.

The challenge of this measurement then is clearly experimental. A signal of 100 events if the branching ratio is at the predicted level requires that the apparatus control all backgrounds to less than the 10^{-11} level. In order to achieve a two order of magnitude increase in sensitivity per year of data taking while maintaining excellent control of all backgrounds requires an apparatus with much higher rate capabilities than has been achieved in the BNL experiment. This leads us to propose a decay in flight experiment in contrast to the stopped kaon technique used at BNL. This new experiment is known as “Charged Kaons at the Main Injector”, or “**CKM**”.

In addition to the paramount goal of measuring the $K^+ \rightarrow \pi^+ \nu \bar{\nu}$ branching ratio we also plan a series of other measurements of rare charged kaon decay properties using the CKM apparatus. The high rate capabilities and redundant measurement capabilities of the CKM spectrometer will make it well suited to such a program of measurements.

2 The CKM Physics Program

2.1 $K^+ \rightarrow \pi^+ \nu \bar{\nu}$ Theory

The branching ratio for the $K^+ \rightarrow \pi^+ \nu \bar{\nu}$ decay was first calculated for arbitrary top quark mass by Inami and Lim [7]. The result of that calculation for three light neutrino types is:

$$\frac{B(K^+ \rightarrow \pi^+ \nu \bar{\nu})}{B(K^+ \rightarrow \pi^0 e^+ \nu)} = \frac{3\alpha^2}{8\pi^2 \sin^4 \theta_W} |V_{cs}^* V_{cd} D(X_c) + V_{ts}^* V_{td} D(X_t)|^2 \frac{1}{|V_{us}|^2} \quad (1)$$

$$D(X) = \frac{1}{8} \left\{ 1 + \frac{3}{(1-X)^2} - \frac{(4-X)^2}{(1-X)^2} \right\} X \ln(X) + \frac{X}{4} - \frac{3X}{4(1-X)} \quad (2)$$

$$X_j = \left\{ \frac{m_j}{m_W} \right\}^2; \quad j = c, t. \quad (3)$$

The leading logarithmic QCD corrections for this decay have been evaluated in [8] [9] [10]. In the words of Ellis and Hagelin [8] these corrections are “...numerically significant, relatively free of theoretical ambiguities, and constitute the most important class of radiative corrections to this process.” In contrast to many measurements in the neutral kaon or B systems there is no theoretical uncertainty introduced by the structure of the initial or final state hadron. The structure of the kaon factors out of this calculation since the ratio of two kaon decay amplitudes is calculated. The structure of the $K^+ \rightarrow \pi^+ X$ transition is included with the measured $K^+ \rightarrow \pi^0 e^+ \nu$ branching ratio.

Rein and Sehgal [2] have evaluated the long distance contribution to the $K^+ \rightarrow \pi^+ \nu \bar{\nu}$ decay amplitude and find that these terms contribute 0.7×10^{-13} to the branching ratio.

Over recent years important refinements have been incorporated in the theoretical treatment of $K^+ \rightarrow \pi^+ \nu \bar{\nu}$. Long distance contributions have been estimated quantitatively [2] and were found to be negligible, as expected (smaller in size than the residual uncertainty in the charm contribution). Isospin breaking effects in the relation between the hadronic matrix elements of $K^+ \rightarrow \pi^+ \nu \bar{\nu}$ and $K^+ \rightarrow \pi^0 e^+ \nu$ have been computed [11] and found to be small. In addition, the complete next-to-leading order QCD corrections have been calculated [12] eliminating the dominant theoretical uncertainties of the leading order prediction. This is less than 1% of the lowest value predicted by the Standard Model. We will ignore the QCD and other corrections here for reasons of clarity. It is straightforward to include them. Rein and Sehgal also noted that since the calculation is done by analogy to that for the $K^+ \rightarrow \pi^0 e^+ \nu$ decay mode the kinematic distributions for the two modes should be nearly identical. Particularly the Dalitz plot projection of the missing neutral mass squared ($M_{\nu\bar{\nu}}^2$) should be identical to the ($M_{e^+\nu}^2$) distribution in $K^+ \rightarrow \pi^0 e^+ \nu$ decays. This is an important test of the validity of the calculation.

2.2 Physics reach on the $\bar{\rho} - \bar{\eta}$ plane of $K^+ \rightarrow \pi^+ \nu \bar{\nu}$

The physics of the $K^+ \rightarrow \pi^+ \nu \bar{\nu}$ decay has been well and thoroughly discussed in several recent papers [1], [13]. The figure below, which is reproduced from [13], shows the dependence of the possible measurements on the apex coordinates ($\bar{\rho}, \bar{\eta}$) of the unitarity triangle, where $\bar{\rho}$ and $\bar{\eta}$ are the modified Wolfenstein parameters [14].

The branching ratio of $K^+ \rightarrow \pi^+ \nu \bar{\nu}$ is proportional to the area of the labeled circle on the figure. This circle is described with central parameter values by:

$$Br[K^+ \rightarrow \pi^+ \nu \bar{\nu}] = [0.44 \pm 0.1] \times 10^{-10} [(1.4 - \bar{\rho})^2 + \bar{\eta}^2] \quad (4)$$

The shift of this circle's origin by +0.4 from point B is due to the contribution of the charmed quark in equation 1.0.

The precision with which the magnitude of V_{td} can be determined is one half the fractional uncertainty in the branching ratio measurement combined in quadrature with the uncertainties in the other parameters appearing in equation (4), including V_{cb} and the mass of the charmed

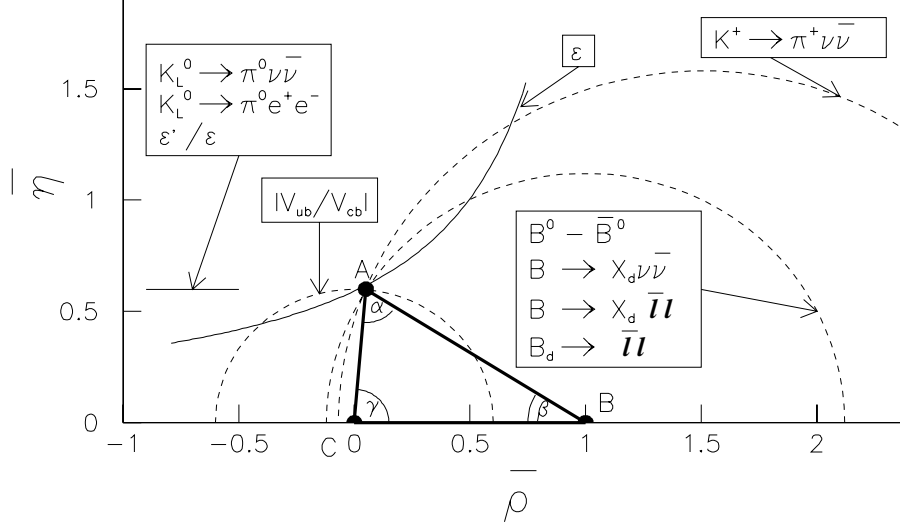


Figure 1: The ideal Unitarity Triangle. For illustrative reasons the value of $\bar{\eta}$ has been chosen to be higher than the fitted central value (reproduced from [13]).

quark. Buras [13] has projected these uncertainties and concludes that a 10% measurement of the $K^+ \rightarrow \pi^+ \nu \bar{\nu}$ branching ratio will yield a 10% determination of V_{td} . This error has a somewhat larger contribution from the uncertainties in the other parameters than from the statistics of the branching ratio measurement.

The measurement of the branching ratio of $K^+ \rightarrow \pi^+ \nu \bar{\nu}$ to the 10% precision level we propose will yield essentially all the available information which the $K^+ \rightarrow \pi^+ \nu \bar{\nu}$ decay mode can provide in determining the parameters of the CKM matrix.

Figure 2 shows a possible outcome on the $\bar{\rho} - \bar{\eta}$ plane of pre-LHC B meson and kaon experiments [15] [13]. For the case of $K^+ \rightarrow \pi^+ \nu \bar{\nu}$ the 5% statistical error we propose to achieve and the total error of 10% including theoretical uncertainties as estimated by Buras [13] are shown. 10% measurements of CKM parameters in the two rare kaon decays match well the 10% determination of $\sin(2\beta)$ anticipated from the present generation of upcoming B meson experiments at the B-factories and colliders. Note that $K^+ \rightarrow \pi^+ \nu \bar{\nu}$ and $\sin(2\beta)$ are essentially orthogonal measurements on the $\bar{\rho} - \bar{\eta}$ plane for the solution assumed [0.04, 0.32] in the figure.

2.3 Related K_L^0 and B-system Measurements and Theory

With two unmeasured parameters in the CKM matrix, parameterized here as $\bar{\rho}$ and $\bar{\eta}$, any meaningful test of the source of CP violation requires at least three different quantities to be independently measured. The spectrum of possible measurements include the ultra-rare charged and neutral decays, $K^+ \rightarrow \pi^+ \nu \bar{\nu}$ and $K_L \rightarrow \pi^0 \nu \bar{\nu}$ in the kaon system, and several observables in the B meson system including mixing, hadronic, semi-leptonic, and leptonic decay modes. Each of these measurements is difficult; more than a few may turn out to be impossible.

The goal of this whole experimental program is a critical test of the source of CP violation in

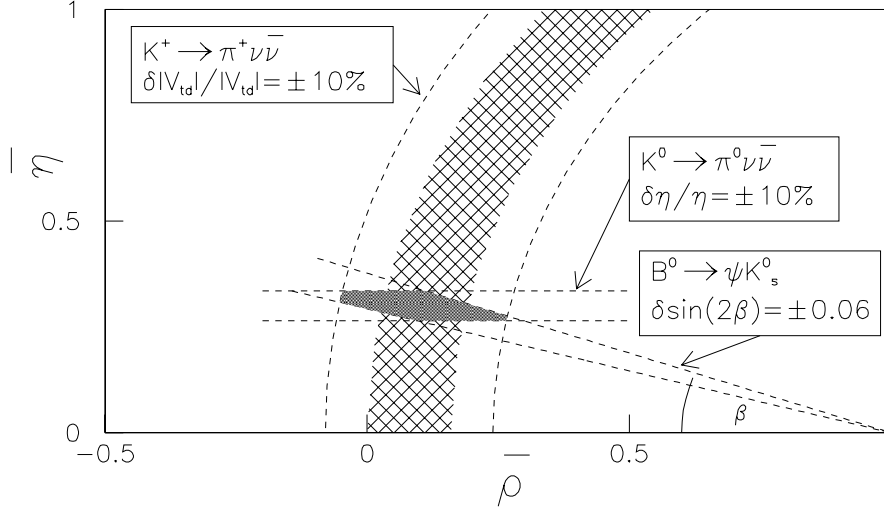


Figure 2: A possible outcome from measurements of $K^+ \rightarrow \pi^+ \nu \bar{\nu}$, $K_L \rightarrow \pi^0 \nu \bar{\nu}$ and $B^0 \rightarrow \psi K_s^0$. The hashed annulus indicates the statistical precision of a 100 event measurement, and the total band indicates the combined statistical and theoretical errors.

nature. This requires that the measurements must have sufficient integrity to compel us to abandon the Standard Model as the sole source of CP violation should that be the outcome. Each measurement has both experimental and theoretical liabilities. Experimental problems can be overcome with a different or improved experimental technique to yield a useful measurement. Theoretical limitations in the relationship between the experimental observables and the physics parameters of interest compromise whole classes of measurements until those limitations can be overcome.

The ultra-rare modes $K^+ \rightarrow \pi^+ \nu \bar{\nu}$ and $K_L \rightarrow \pi^0 \nu \bar{\nu}$ are identified by several authors as modes where the limitations of theory are contained and quantified [15] [13]. In the case of $K_L \rightarrow \pi^0 \nu \bar{\nu}$ the theoretical uncertainties are negligible, and in $K^+ \rightarrow \pi^+ \nu \bar{\nu}$ the theoretical uncertainty of the charm quark contribution is small and under control. The great attractiveness of these kaon decays is that, while the measurements are extremely challenging experimentally, there are certainly meaningful physics results when the branching ratios are reliably measured. As illustrated in figure 2; the two measurements in the kaon system can, by themselves, cleanly determine the two unmeasured CKM parameters. They cannot test the Standard Model's contribution to CP violation without a third, independent, measurement.

In the B meson system this story is much longer and more complicated. The same authors have studied the theoretical limitations of the B sector measurements [15] [13]. A summary of their conclusions is as follows:

1. The present uncertainty the magnitude of V_{td} measured with the B_d mixing parameter x_d is already dominated by the uncertainties in the lattice calculations of F_{B_d} and B_{B_d} . This is a theoretical limitation common to most of the hadronic B decays.
2. The B_s/B_d ratios of these observables is significantly less sensitive to lattice calculation un-

certainties. These require matching measurements from hadronic B production experiments with good enough tagging to distinguish B_s from B_d events to complement the measurements in the B_d decay expected from the B factories.

3. Among the conventional measurements of the unitarity triangle angles α, β and γ expected from the B factories only β as measured with $B^0 \rightarrow \psi K_s^0$ is free from significant theoretical uncertainties.
4. α measured with $B^0 \rightarrow \pi^+ \pi^-$ suffers from significant “penguin pollution” which must be overcome before this measurement can be useful for CKM parameter determinations. The isospin analysis required to control this problem requires measurements of modes which are probably too low in branching ratio to be well measured with the available luminosity.
5. The B sector analogies of the ultra-rare kaon decays; $B^0 \rightarrow X_d \nu \bar{\nu}$, $B^0 \rightarrow X_s \nu \bar{\nu}$, $B_d^0 \rightarrow \mu^+ \mu^-$ and $B_s^0 \rightarrow \mu^+ \mu^-$ are likewise theoretically clean. The Standard Model branching ratios for these modes are believed to be beyond the sensitivity of all proposed experiments.
6. x_s/x_d may make a useful contribution to constraining the apex of the unitarity triangle provided a measurement and not just a lower limit can be achieved.

The B sector experiments have more than ample experimental insurance; six experiments are under construction, Babar, Belle, CDF, CLEO-III, Dzero, and HERA-B. Their liabilities appear to be mainly theoretical; only the measurement of $\sin(2\beta)$ is known to be unambiguous. In the kaon sector the claim of our theoretical colleagues is that both ultra-rare modes are well understood. The challenge in the kaon measurements is all experimental; and formidable. Presently there is the BNL $K^+ \rightarrow \pi^+ \nu \bar{\nu}$ experiment E787 which has reported one event and KTeV at Fermilab which limits the $K_L \rightarrow \pi^0 \nu \bar{\nu}$ branching fraction to less than 1.6×10^{-6} , (90% C.L.) [16] where the theoretical expectation is $(3 \pm 1) \times 10^{-11}$ [1]. Two proposals to measure $K_L \rightarrow \pi^0 \nu \bar{\nu}$ at BNL and KEK have been scientifically approved by the respective laboratories, and these collaborations are now in the technical design phase. There are two additional $\pi \nu \bar{\nu}$ proposals; a proposal for a $K_L \rightarrow \pi^0 \nu \bar{\nu}$ experiment at Fermilab (KAMI) now in preparation and this proposal to measure $K^+ \rightarrow \pi^+ \nu \bar{\nu}$ (CKM). In addition to these efforts, elements of the Brookhaven E787 collaboration are considering upgrades that will allow the stopped K^+ technique to be pushed to the 1×10^{-11} single event sensitivity.

Figure 2 displays a test of the source of CP violation in nature using only measurements known to be free of theoretical problems. If these three measurements can be successfully accomplished and the three regions of the $\bar{\rho} - \bar{\eta}$ plane do not mutually overlap consistent with one point, the hypothesis that the Standard Model is the sole source of CP violation is untenable. The only alternatives will be to attack the veracity of the measurements or to invoke new physics. Other measurements in both the B and kaon sectors can, and hopefully will, make comparable contributions. These will be extremely valuable in confirming the Standard Model CP hypothesis. Any of those measurements which can be called into question over issues of the reliability of lattice calculations, penguin contributions or other theoretical weaknesses will not have the integrity to falsify the hypothesis of the Standard Model as the sole source of CP violation.

2.4 Other K^+ Physics

The CKM apparatus will be a charged kaon decay spectrometer of unparalleled decay rate capability with excellent resolution in space, time, momentum and velocity for all possible kaon decay daughters and grandchildren save neutrinos. Several other physics measurements should be possible in this apparatus. The goal of broadening the physics scope of the experiment is two fold. Making additional

important measurements increases the physics return on the capital and personal investments in building this new apparatus.

It has been observed [17] that by adopting the decay in flight technique we have made a radical departure from all previous experiments searching for $K^+ \rightarrow \pi^+ \nu \bar{\nu}$ and must demonstrate, anew, 11 orders of magnitude of background rejection while maintaining reasonable acceptance. While a bit overstated this argument is not without merit. The best way to develop the understanding of both hardware and analysis techniques necessary to achieve the goals for $K^+ \rightarrow \pi^+ \nu \bar{\nu}$ is to establish and achieve real physics milestones and measurements.

The boundary conditions on other physics goals for CKM are clear. There will be no compromises in the either sensitivity or background rejection required for $K^+ \rightarrow \pi^+ \nu \bar{\nu}$ in order to accommodate other physics goals. After we have designed a no-compromise $K^+ \rightarrow \pi^+ \nu \bar{\nu}$ apparatus we will investigate the possibilities for other physics goals. Modest incremental costs for apparatus additions and/or modifications and the possibility of dedicated running periods with different triggers will be seriously entertained by the collaboration at that time.

Within these boundary conditions we enumerate below several possible physics measurements which will likely be within the reach of the CKM apparatus. Not all of them may make the final cut. This is a proposal for first stage (physics) approval where a discussion of the likely physics reach and scope of the experiment is addressed. Assuming that this proposal is approved we expect that our proposal for second stage (technical and budgetary) approval will detail and cost an apparatus and its potential physics reach. If some of the topics below fall by the wayside in that design process they are just an additional sacrifice toward our primary goal of measuring $K^+ \rightarrow \pi^+ \nu \bar{\nu}$.

2.4.1 $K^+ \rightarrow \mu^+ \nu_\mu \gamma$ Form Factor Measurement

The radiative decay $K^+ \rightarrow \mu^+ \nu_\mu \gamma$ provides a important window into the hadronic structure of the charged kaon. This process is described by an effective Lagrangian in chiral perturbation theory (CHPT). Three processes contribute to the $K^+ \rightarrow \mu^+ \nu_\mu \gamma$ decay, the relatively large internal bremsstrahlung (IB) amplitude, which does not depend on kaon structure, the structure dependent (SD) emission of a photon from intermediate kaon states and the interference (INT) between the SD and IB amplitudes. Both SD and INT provide kaon structure information. The kaon vector and axial vector form factors to be measured are naturally observed in this decay mode as $(F_v - F_a)M_k$ and $(F_v + F_a)M_k$. These form factors are extracted in a Dalitz plot analysis. The large IB amplitude gives a pole in one corner of the Dalitz plot while the INT and SD contributions dominate the Dalitz plot population far from this pole.

All present measurements are tabulated below in table 1 including the values of $(F_v \pm F_a)M_k$ obtained from $K^+ \rightarrow e^+ \nu_e \gamma$ assuming universality. The predictions from CHPT are also shown. These experiments all used stopped kaons. All the experiments so far were sensitive to regions of the Dalitz plot which allow a measurement of $F_v + F_a$ and gave only limits for on $F_v - F_a$. The recent BNL787 measurement is the statistically dominant measurement with 2693 $K^+ \rightarrow \mu^+ \nu_\mu \gamma$ events, the other measurements have less than 100 events each.

From initial simulation studies of the CKM sensitivity to this mode we estimate an accepted signal rate of 300 Hz for the $K^+ \rightarrow \mu^+ \nu_\mu \gamma$ mode with about 1% of these events in the Dalitz plot regions sensitive the form factors [25]. At this rate the world statistics can be acquired with a few hours of data collection. We expect to be able to improve the measurement of $F_v + F_a$ and provide a first measurement of $F_v - F_a$.

$K^+ \rightarrow l^+ \nu_l \gamma$ Form Factors			
	mode	$ F_V + F_A M_K$	$ F_V - F_A M_K$
CHPT prediction [18] [19]		0.097	0.037
CERN PS Heard 75 [20]	$K^+ \rightarrow e^+ \nu_e \gamma$	0.147 ± 0.011	$-0.49 <> +0.49$
KEK Akiba 85 [21]	$K^+ \rightarrow \mu^+ \nu_\mu \gamma$	< 0.23	$-2.5 <> +0.30$
ITEP PS Demidov 90 [22]	$K^+ \rightarrow \mu^+ \nu_\mu \gamma$	$-1.2 <> +1.1$	$-2.2 <> +0.60$
BNL787 Convery 97 [23, 24]	$K^+ \rightarrow \mu^+ \nu_\mu \gamma$	$0.165 \pm 0.007 \pm 0.011$	unmeasured

Table 1: Theoretical Predictions and Experimental status

2.4.2 $K^+ \rightarrow \pi^+ e^+ e^-$, $K^+ \rightarrow \pi^+ \mu^+ \mu^-$ Form Factor/Branching Ratio Measurements

The precise study of the decays $K^+ \rightarrow \pi^+ e^+ e^-$ and $K^+ \rightarrow \pi^+ \mu^+ \mu^-$ opens new possibilities for the investigation of chiral perturbation theory (CHPT) in the $\Delta S=1$ weak interactions. Careful measurements of the corresponding branching ratios and Dalitz plot analyses to measure the form factors in these decay modes are tests of CHPT predictions. (See, for example, the review [26].)

The integral ratio of these two mode $R(\mu\mu/ee) = \text{Br}[K^+ \rightarrow \pi^+ \mu^+ \mu^-] / \text{Br}[K^+ \rightarrow \pi^+ e^+ e^-]$ and the differential ratios across the Dalitz plot $\rho(\mu\mu/ee)$ cancel many of the theoretical uncertainties and provide a focused comparison of CHPT predictions with these weak non-leptonic interactions. In different models the predicted values of $R(\mu\mu/ee)$ vary in the range 0.2-0.3. Measurements with experimental accuracy of $\delta R=2\text{-}3\%$ should give clean tests of the CHPT predictions to the 10% level. One early paper [27] suggested that the differential ratio $\rho(\mu\mu/ee)$ in the region of small π^+ energies is sensitive to the contribution of second order weak diagrams.

The existing data for these two decay mode are dominated by results from recent BNL K^+ experiments. BNL777 [28] observed 500 $K^+ \rightarrow \pi^+ e^+ e^-$ decays in the kinematic region above the π^0 ($M_{ee} > 150 \text{ MeV}/c$). From the shape of the di-electron mass spectrum they measured the slope of the vector form factor in the decay to be $\lambda = 0.105 \pm 0.035 \pm 0.015$ and the branching ratio $\text{Br}[K^+ \rightarrow \pi^+ e^+ e^-] = (2.75 \pm 0.23 \pm 0.13) \times 10^{-7}$ which determines one of the dimensionless CHPT parameters to be $w_+ = 0.89^{+0.24}_{-0.14}$. BNL787 [29] observed 22 $K^+ \rightarrow \pi^+ \mu^+ \mu^-$ events reporting a branching ratio of $\text{Br}[K^+ \rightarrow \pi^+ \mu^+ \mu^-] = (5.0 \pm 0.4 \pm 0.9) \times 10^{-8}$ and $R(\mu\mu/ee) = 0.167 \pm 0.036$, which is 2.2σ below the CHPT prediction $R(\mu\mu/ee) = 0.236$.

In CKM we estimate sensitivities to these two decay modes of order 10^4 and 10^3 per week for $K^+ \rightarrow \pi^+ e^+ e^-$ and $K^+ \rightarrow \pi^+ \mu^+ \mu^-$ respectively. CKM has a significant advantage with muon identification the pion RICH to suppress the background to $K^+ \rightarrow \pi^+ \mu^+ \mu^-$ from $K^+ \rightarrow \pi^+ \pi^+ \pi^-$ with two pion decays in flight.

2.4.3 Nonleptonic Charged Kaon decays and the Search for Direct CP Violation in K^\pm decays

Studies of the nonleptonic charge kaons decays, $K^\pm \rightarrow \pi^\pm \pi^+ \pi^-$, $K^\pm \rightarrow \pi^\pm \pi^0 \pi^0$, $K^\pm \rightarrow \pi^\pm \pi^0 \gamma$ and $K^\pm \rightarrow \pi^\pm \gamma \gamma$ are important for the understanding of the mechanisms of $\Delta S=1$ hadronic weak interactions and of the main properties of the chiral perturbation theory (CHPT) for these processes. In addition to precision CHPT tests, new measurements in this field with greatly enlarged statistics can in principle enable the search for direct CP violation effects through measurement of rate asymmetries in $(K^+ \rightarrow \bar{f}) / (K^- \rightarrow f)$ or Dalitz plot asymmetries.

In principle it is straightforward to operate the charged kaon beam line at both polarities,

allowing K^+ and K^- data sets to be collected at different times. In practice, the precision measurements described below will be vulnerable to the different beam background environments of K^+ and K^- running. In addition, detector efficiencies between different K^+ and K^- running periods would have to be controlled to a very high level. Nevertheless, there is some value in listing the potential measurements with the understanding that a serious attack on these physics topics requires detailed study that we have not started yet.

To control possible systematic biases in the acceptance of the apparatus it is desirable to take data with positive and negative kaon beam which are as similar in intensity and other conditions as possible. Intensity matching can be achieved by reducing the K^+ intensity by about a factor of two to match the ratio of K^+ and K^- production cross-sections. By normalizing $K^\pm \rightarrow f$ decays mode to majority decay modes like $K^\pm \rightarrow \mu^\pm \nu_\mu$ and $K^\pm \rightarrow \pi^\pm \pi^0$ acquired simultaneously it is possible to cancel many systematic effects associated with changes in the polarity of the beam and different running periods. This is the same double ratio technique used by KTeV to measure CP violation in K^0 decay.

The CP rate asymmetry modes can be observed in the rate asymmetry $\delta, /2, = [(K^+ \rightarrow \bar{f}) - (K^- \rightarrow f)] / [(K^+ \rightarrow \bar{f}) + (K^- \rightarrow f)]$ or or an equivalent asymmetry in the Dalitz plot slope parameter $\delta g/2g$. Present predictions for these asymmetries from lowest non-vanishing order in CHPT are given in table 2 along with world sample sizes and existing CP asymmetry limits [38]. The CKM events/week rates shown in table 2 are estimates based on, as yet, unsimulated running conditions.

$K^+ \rightarrow \bar{f}$ CP Asymmetry Predictions and World data					
decay	$B(K^+ \rightarrow \bar{f})$	Asymmetry	Theory Estimate	present limits world events	CKM evt/week
$K^\pm \rightarrow \pi^\pm \pi^+ \pi^-$	5.6×10^{-2}	$\delta g/2g$ $\delta, /2,$	$(-2.3 \pm 0.6) \times 10^{-6}$ [37] $(-6.0 \pm 2.6) \times 10^{-8}$ [37]	$(4 \pm 6) \times 10^{-4}$ 3.2×10^6	2×10^9
$K^\pm \rightarrow \pi^\pm \pi^0 \pi^0$	1.7×10^{-2}	$\delta g/2g$ $\delta, /2,$	$(1.3 \pm 0.4) \times 10^{-6}$ [37] $(2.4 \pm 0.8) \times 10^{-7}$ [37]	$(0 \pm 3) \times 10^{-3}$ 2×10^4	3×10^8
$K^\pm \rightarrow \pi^\pm \pi^0 \gamma$	2.8×10^{-4}	$\delta, /2,$	$< 10^{-5}$ [26, 37]	$(1 \pm 3) \times 10^{-2}$ 6500	6×10^6
$K^\pm \rightarrow \pi^\pm \gamma \gamma$	6×10^{-7}	$\delta, /2,$	$< 10^{-4}$ [36]	31 [34]	1.5×10^4
$K^+ \rightarrow \pi^+ \pi^0 e^+ e^-$	1×10^{-6}	angular dist			1×10^5

Table 2: Theoretical predictions, world data and CKM potential for observing CP Asymmetries in charge kaon non-leptonic decays

CP violation in $K^+ \rightarrow \pi^+ \pi^+ \pi^-$ decays has long been discussed in the literature [38, 37] and references therein, with the signature essentially being an asymmetry in the 3π Dalitz plot with respect to the odd-pion axis. Early estimates of this asymmetry as well as decay rate asymmetries were as high as $\sim 10^{-3}$ [35], but current estimates [37] are in the 10^{-6} — 10^{-8} range, which is beyond the statistical reach and systematic stability of the CKM apparatus.

The present theoretical predictions for CP charge asymmetries in all the non-leptonic decays appear out of experimental reach for CKM at the level of raw statistical power. It is however conceivable that the CKM apparatus could improve the existing asymmetry limits significantly, and

perhaps to the $\sim 1 \times 10^{-4}$ in decays such as $K^\pm \rightarrow \pi^\pm \pi^0 \gamma$ through experimentally stable parameters such as R defined below. Deviation of R from unity would be a signal of direct CP violation.

$$R = \frac{B(K^+ \rightarrow \pi^+ \pi^0 \gamma) / B(K^+ \rightarrow \pi^+ \pi^0)}{B(K^- \rightarrow \pi^- \pi^0 \gamma) / B(K^- \rightarrow \pi^- \pi^0)} \quad (5)$$

Such a measurement is similar in principle to measurement of $Re(\epsilon'/\epsilon)$ in the $K_L \rightarrow 2\pi$ system. Clearly a large amount of work is yet required to determine if the CKM apparatus is capable of this measurement, but it is at least encouraging that a reasonably robust experimental parameter (R) can be constructed. In addition to rate asymmetries, the angular decay plane distribution asymmetry in $K^+ \rightarrow \pi^+ \pi^0 e^+ e^-$ is also sensitive to CP violation effects in analogy with the same decay mode in the neutral kaon system.

Certainly we should consider pioneering some of these measurements at levels of sensitivity above the current predictions in order to learn to what measurements are possible with a more dedicated effort in the future. We are also well positioned to explore large charge asymmetries, as might be discovered in the present HyperCP experiment.

2.4.4 Measurement of V_{us} from $K^+ \rightarrow \pi^0 e^+ \nu$ and $K^+ \rightarrow \pi^0 \mu^+ \nu$ decays

An experiment called CKM ought to be able to measure more than one CKM matrix element. We consider here the possibility of improving the measurement of V_{us} (the sine of the Cabibbo angle) with precision measurements of the absolute branching fractions in $K^+ \rightarrow \pi^0 e^+ \nu$ and $K^+ \rightarrow \pi^0 \mu^+ \nu$ decays.

The matrix element of the K_{l3}^+ decays has the well known form [30]

$$M = \frac{G}{\sqrt{2}} V_{us} [f_+(t)p_\alpha + f_-(t)q_\alpha] \phi_\pi \phi_K \bar{u}_\nu \gamma^\alpha (1 + \gamma_5) u_l \quad (6)$$

where $p = p_K + p_\pi$ and $q = p_K - p_\pi = p_l + p_\nu$, $t = q^2$ is squared momentum transfer to the leptons. In this matrix element the $f_-(t)$ contribution is proportional to m_l^2 . Thus, only the $f_+(t)$ form factor contributes to the K_{e3}^+ decay process, and this simplest case gives the best opportunity for the determination of the V_{us} element of CKM matrix in (6).

Using the matrix element from (6) the K_{l3} decay width may be calculated:

$$\Gamma(K_{l3}) = \frac{G_F^2}{192\pi^2} M_K^5 |V_{us}|^2 C^2 I |f_+(0)|^2 (1 + \delta_{RC}) \quad (7)$$

where $C^2 = 1/2$ for $K^+ \rightarrow \pi^0 e^+ \nu_e$, $C^2 = 1$ for $K^0 \rightarrow \pi^- e^+ \nu_e$, I is the phase space factor and δ_{RC} is the radiative correction. Assuming linear approximation of the form factor

$$f_+(t) = f_+(0) \left(1 + \lambda_+ \frac{t}{m_\pi^2} \right) \quad (8)$$

measured values of the form factor slopes are $\lambda_+(K_{e3}^0) = 0.0300 \pm 0.0016$ and $\lambda_+(K_{e3}^+) = 0.0286 \pm 0.0022$ and there is a small correction to the space phase for the form factor slopes. The experimentally measured K_{e3}^+ decay width is $\Gamma(K_{e3}^+) = 2.578(1 \pm 0.02) \times 10^{-15}$ MeV.

In the SU(3) conservation limit ($m_u = m_d = m_s$) $f_+(0) = 1$ due to the conservation of the weak vector current (CVC). In reality we must take into account SU(3) breaking effects [31]. From theoretical point of view the most simple case is $K^0 \rightarrow \pi^- e^+ \nu_e$ decay. Here, as follows from the Ademollo-Gatto theorem, only second order corrections for the SU(3) breaking must be taken in the consideration ($(m_s - m_u)^2$ approximation). For $K^+ \rightarrow \pi^0 e^+ \nu_e$ decay the situation is more

complicated due to $\pi^0 - \eta$ mixing effects (isospin conservation breaking, which is effect of first order to $(m_d - m_u)$). Reference [31] obtained numerical values of form factors as: $f_+(0)_{K^0\pi^-} = 0.961 \pm 0.008$ and $f_+(0)_{K^+\pi^0} = 0.982 \pm 0.008$.

Combining all the above expressions the V_{us} matrix element is:

$$V_{us} = 0.2201(1 \pm 0.010 \pm 0.008) \quad (9)$$

where the first error is connected with experimental measurement (6) and the second error represents uncertainty in theoretical calculations.

It is possible to reduce significantly the experimental error with a new measurement from CKM. KTeV has already taken such data for the K_{e3}^0 mode. Their analysis is underway now. CKM should be able to measure the absolute branching fractions of both the $K^+ \rightarrow \pi^0 e^+ \nu$ and $K^+ \rightarrow \pi^0 \mu^+ \nu$ decays with a statistical precision of about 0.1%. Several other proposals exist for improved measurements in K_{e3}^+ [32, 26].

The possibility of a new theoretical analysis for more precise evaluation of $f_+(0)_{K^+\pi^0}$ value is unclear now. The Fermilab Lattice QCD group has undertaken to improve the theoretical uncertainty in the K_{e3}^0 mode in support of the KTeV measurement [33] with a goal of 0.1%. They say now that achieving this goal looks hard but a significant improvement beyond the present 1% level seems likely.

With significant theoretical improvements and experimental cross checks from several measurements the value V_{us} can be improved from the present value based on theory and experiments from 1984. This will permit, among other things, a better test of unitarity of the first row of the CKM matrix. The present situation is:

$$\Delta = 1 - [|V_{ud}|^2 + |V_{us}|^2 + |V_{ub}|^2] = 0.0027 \pm 0.0019 \quad (10)$$

3 The Experimental Method

3.1 Experimental Overview

The principal goal of CKM is to observe a large sample (about 100 events) of $K^+ \rightarrow \pi^+ \nu \bar{\nu}$ decays with small background. A signal of 100 events if the branching ratio is 1×10^{-10} would imply that CKM needs to reject all backgrounds to below the 10^{-11} level. Achieving this level of background rejection is the major challenge CKM faces. In addition, it is necessary to have methods for convincingly measuring the background(s), since an observation of $K^+ \rightarrow \pi^+ \nu \bar{\nu}$ will not be characterized by a clear signature, such as a mass peak. In this section we will discuss the backgrounds to $K^+ \rightarrow \pi^+ \nu \bar{\nu}$ and explore the requirements they impose on the detector.

An essential ingredient in any successful rare K decay experiment is measurement redundancy. The experience of the recent generation of rare K decay experiments clearly teaches this lesson. It would be unrealistic to seek to improve upon these experiments without building significant redundancy into the detector. Therefore, CKM will make completely redundant measurements of both beam kaons and charged decay products in the spectrometer. We will elaborate on these features of the detector after discussing the backgrounds and how they may be suppressed.

3.2 Background Sources

The most obvious potential backgrounds to $K^+ \rightarrow \pi^+ \nu \bar{\nu}$ are the decays $K^+ \rightarrow \mu^+ \nu$ and $K^+ \rightarrow \pi^+ \pi^0$, which have large branching ratios (64% and 21%, respectively). If the muon is misidentified as a pion in the former case, or if the photons from the π^0 decay are missed in the latter case, then

these modes can resemble $K^+ \rightarrow \pi^+ \nu \bar{\nu}$ decays. Rejecting these decays depends on exploiting the kinematics of two-body decays and on highly effective vetos of muons and photons. We will discuss the kinematic issues first.

In the two-body decays $K^+ \rightarrow \mu^+ \nu$ and $K^+ \rightarrow \pi^+ \pi^0$, the charged particle's center-of-mass momentum is fixed at 236 MeV and 205 MeV, respectively. In stopped- K experiments, where the center-of-mass frame and the laboratory frame are the same, this results in narrow peaks in the observed momentum of the charged particles produced in these decays, and consequently these decays can be highly suppressed simply by excluding these peaks from the $K^+ \rightarrow \pi^+ \nu \bar{\nu}$ signal region. Of course, in any reference frame (specifically in the laboratory frame of a decay-in-flight experiment), the kinematic rejection of two-body decays is possible.

In the $K^+ \rightarrow \pi^+ \nu \bar{\nu}$ decay, for a specific value of the pion center-of-mass momentum, the invariant mass $M_{\nu\bar{\nu}}$ of the lepton pair is fixed. Since the neutrinos are not observed, it is natural to think of $M_{\nu\bar{\nu}}$ as simply the missing mass in the decay. Hereafter, we will call it M_{miss} . The missing mass M_{miss} in $K^+ \rightarrow \pi^+ \pi^0$ and $K^+ \rightarrow \mu^+ \nu$ decays is simply m_{π^0} and 0, respectively. Experimentally, M_{miss} is readily obtained from measurements of the momenta and directions of the parent K^+ and the daughter π^+ . The issue which is relevant for background rejection is not whether one's detector is in any particular reference frame, but to what extent the kinematic resolution is adequate, and to what extent experimental mismeasurements lead to misclassification of events.

The measurable quantities in a decay-in-flight experiment are the momentum p_K of the parent kaon, the momentum p of the charged particle produced in the decay (which may be a muon or a pion, or an electron from a decay such as $K^+ \rightarrow \pi^0 e^+ \nu$), and the angle θ between the parent's trajectory and that of the charged daughter. In terms of these quantities, a sufficiently good approximation is that

$$M_{\text{miss}}^2 = M_K^2 (1 - p/p_K) + m^2 (1 - p_K/p) - pp_K \theta^2, \quad (11)$$

where M_K is the kaon mass and m is the mass of the charged daughter. It is instructive to consider the distribution of events from different decays in p and θ for fixed p_K . For any two-body decay, M_{miss} has a single value, so that allowed values of p and θ form a curve. For a three-body decay, p and θ can take on any pair of values which lie below a curve defined by the minimum value of M_{miss} . Figure 3 illustrates this by showing the curve (solid line) corresponding to $K^+ \rightarrow \pi^+ \pi^0$ ($M_{\text{miss}} = m_{\pi^0}$) and the distribution of points for $K^+ \rightarrow \pi^+ \nu \bar{\nu}$ decays (minimum $M_{\text{miss}} = 0$). A kaon energy of 22 GeV, which is the proposed CKM beam energy, is assumed. Figure 3 also shows a dashed curve, which corresponds to the upper boundary of $K^+ \rightarrow \pi^+ \pi^+ \pi^-$ decays. These two curves delineate regions where background rejection issues are somewhat different, as summarized in table 3. In the table the region above the solid line is referred to as "Region 1", between the solid and dashed curves as "Region 2", and below the dashed curve as "Region 3." Traditionally $K^+ \rightarrow \pi^+ \nu \bar{\nu}$ searches have focussed on Region 1. However, considerable acceptance can be gained by including Region 2 as well. Region 3 appears intractable, owing to the $K^+ \rightarrow \pi^+ \pi^+ \pi^-$ decay; it has a large branching ratio, lacks two-body kinematic rejection, lacks a particle identification veto on the observed charged particle, and has no photons to veto. In CKM our efforts thus far have been concentrated on understanding backgrounds in Region 1, but our intention is to study Region 2 as time permits and keep it as a goal.

Rejecting the two-body decay backgrounds depends upon accurately determining M_{miss} . From equation 11, we can estimate the effect on M_{miss} of mismeasurements of the underlying quantities. Simply summarizing the result, we need to measure all three quantities to about 1% of itself in order to achieve sufficient resolution on M_{miss} to make a $K^+ \rightarrow \pi^+ \nu \bar{\nu}$ search viable. Ultimately however, it is not measurement resolution which limits background rejection. Physical processes, such as multiple or single Coulomb scattering and inelastic hadronic scattering, which occur in the

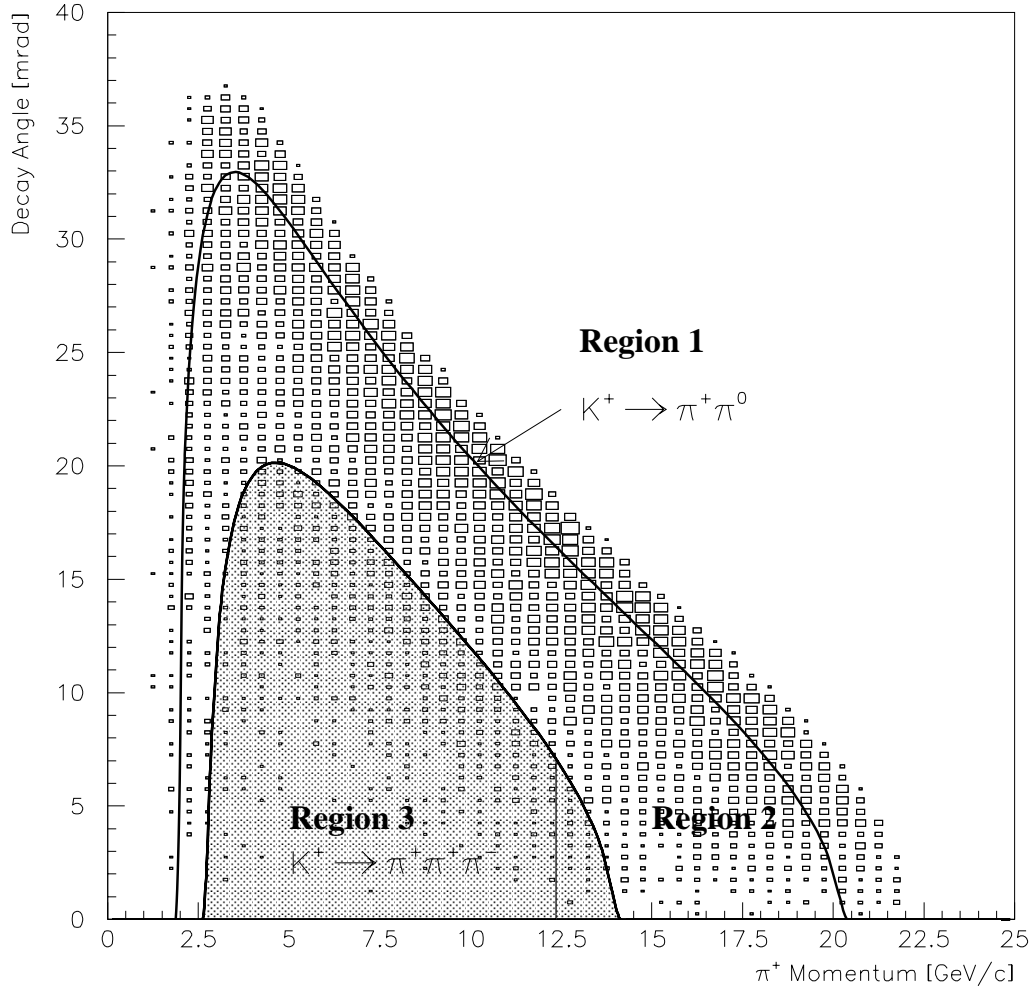


Figure 3: Decay angle versus momentum for $K^+ \rightarrow \pi^+ \nu \bar{\nu}$ events. Three distinct analysis regions are shown.

Region	K -decay Backgrounds	Branching Ratio	Minimum M_{miss} (MeV)	Rejection Methods
1	$K^+ \rightarrow \mu^+ \nu$	0.635	0	2-body kinematics, μ -veto
	$K^+ \rightarrow \pi^+ \pi^0$	0.212	135	2-body kinematics, γ -veto
	$K^+ \rightarrow \mu^+ \nu \gamma$	5.5×10^{-3}	0	μ -veto, γ -veto
2	$K^+ \rightarrow \pi^+ \pi^0$	0.212	135	2-body kinematics, γ -veto
	$K^+ \rightarrow \pi^0 e^+ \nu$	0.048	135	e -veto, γ -veto
	$K^+ \rightarrow \pi^0 \mu^+ \nu$	0.032	135	μ -veto, γ -veto
	$K^+ \rightarrow \pi^+ \pi^0 \pi^0$	0.017	270	γ -veto
	$K^+ \rightarrow \mu^+ \nu \gamma$	5.5×10^{-3}	0	μ -veto, γ -veto
	$K^+ \rightarrow \pi^+ \pi^0 \gamma$	2.8×10^{-4}	135	γ -veto
3	Same as region 2, plus $K^+ \rightarrow \pi^+ \pi^+ \pi^-$	0.056	279	charged particle veto

Table 3: Kaon decay modes which are potential backgrounds to $K^+ \rightarrow \pi^+ \nu \bar{\nu}$ in each of the three regions, defined in the text. The list is not exhaustive and includes only modes with relatively large branching ratios.

materials which make up the detector introduce unavoidable mismeasurements. These effects can only be reduced by minimizing the amount of material the charged particles traverse before the measurements are made. Minimizing material drives much of the CKM design.

For the $K^+ \rightarrow \mu^+ \nu$ and some other kaon decays which may introduce backgrounds, considerable rejection can be obtained from particle identification. As a consequence, exceptionally good particle identification is necessary for CKM.

For the $K^+ \rightarrow \pi^+ \pi^0$ and some other kaon decays which may introduce backgrounds, considerable rejection can be obtained by observing photons. As a consequence, a virtually hermetic photon veto system is required for CKM.

In addition to kaon decays, other sources of backgrounds are possible. Any process in which a K^+ enters the detector and a π^+ exits is a candidate background. An interesting example is a charge exchange interaction where the beam K^+ emerges as a K^0 which subsequently decays via $K_L^0 \rightarrow \pi^+ e^- \nu$. The electron can have arbitrarily low momentum and go unobserved, leaving an event which satisfies the $K^+ \rightarrow \pi^+ \nu \bar{\nu}$ topology. Other more mundane hadronic interaction scenarios of the beam K^+ can produce a single observed π^+ . Also, since the beam will inevitably contain some pions, it is possible for an incoming π^+ which scatters to be mistaken for a K^+ and again simulate the $K^+ \rightarrow \pi^+$ topology. Of course, handles are available to suppress these hadronic interaction backgrounds, such as requiring that the putative K^+ and π^+ make a good vertex which is well separated from any material, as well as vetoing events in which extra particles from the interactions are observed. These capabilities are important for CKM.

Finally, various accidental scenarios — for example, two kaon decays close together in time — can introduce backgrounds. Many of the same tools which remove other backgrounds are effective here, but in addition the CKM detector must be capable of precision timing.

3.3 Beam Issues

CKM must sample about 5×10^6 K^+ decays per spill in order to reach a single event sensitivity of 1×10^{-12} in two years of running at the Main Injector. This implies the beam must provide a high

flux of K^+ 's, in the neighborhood of 3×10^7 per spill. It is necessary for background rejection for CKM to measure the identity, momentum, and trajectory of each beam particle. That is, particle identification and tracking detectors must operate in this beam. A phototube-based ring-imaging Cherenkov counter can operate in this environment. Various high-rate tracking technologies are viable provided they have sufficient segmentation to reduce the rate through any single cell to an acceptable level. However, it is clear that a ~ 50 MHz beam rate (of which 30 MHz are K^+) poses significant technical challenges for tracking detectors. Therefore, it is important for CKM that the beam consist primarily of kaons.

3.4 Detector Requirements

3.4.1 The Momentum Spectrometer

The main goal of momentum spectrometer is to measure the vector momentum of each beam particle, and decay daughter(s). The technical requirements for this system is driven by the resolution required for the suppression of background processes previously discussed, the minimization of the secondary interactions in the beam, and time resolution. The 50 MHz rate of beam particles poses a significant challenge for the design of these detectors. Previous rare kaon and hyperon decay experiments have approached these rates, such as Brookhaven experiment E871 ($K_L \rightarrow \mu^\pm e^\mp$ search) which ran at ~ 20 MHz/ m^2 , and the Fermilab HyperCP experiment which ran at ~ 30 MHz/ m^2 .

Two momentum spectrometers compose the complete system: "Upstream", to measure the momentum of the ~ 22 GeV/ c beam kaons with the accuracy better than 0.5% and "Downstream", to measure the momentum of charged kaon decay daughters with an accuracy of 1%. The ultimate resolution requirement is a M_{miss}^2 resolution $\sim M_{\pi^0}^2 / 10$ for $K^+ \rightarrow \pi^+ \pi^0$ decays measured with the momentum vectors from both spectrometers.

The momentum spectrometers also provide the geometrical tracking measurements to reconstruct the position and quality of the kaon decay vertex. The distance of closest approach "DOCA" of the kaon and daughter trajectories is an important cut in rejecting interactions and decay in flight of kaon daughters.

The high beam rate requires that the detectors must have excellent time resolution. This will help to suppress accidentals, pile-up and tracking errors. ± 1 nsec time resolution is desirable for these spectrometers. Since the neither straw tube or silicon tracking technologies have the required speed to achieve this level of time resolution, a fiber tracking plane is included in each spectrometer; the "Beam Time Stamp" system in the upstream momentum spectrometer and a fiber plane at the end of the downstream momentum spectrometer that will tag candidate spectrometer tracks with precise times.

The channel count for the momentum spectrometers is driven by the rate capability of the detectors, as well as by dead time, maximum occupancy and resolution considerations. Low occupancy is important to avoid ambiguity in track reconstruction.

Both of these spectrometers have ~ 50 MHz of beam running through them. Minimizing interactions in the material of these spectrometers is critical to control backgrounds. The greatest sensitivity to material in the beam is in the planes closest to the fiducial decay volume.

The upstream momentum spectrometer must momentum analyze each beam particle. The most attractive tracking technology here is double-sided silicon microstrips with $50 \mu\text{sec}$ pitch and a conventional beamline dipoles for the spectrometer magnet. The large number of strips across the 5 cm diameter beam achieves the desired low occupancy, single channel rate and the required spatial resolution. To minimize the multiple scattering and secondary interactions the detectors must have the minimum material along the beam line. This requires integrating the tracking system into the

vacuum beam transport system either by putting the silicon into the beamline vacuum or making beam windows thin compared to the $300\text{ }\mu\text{sec}$ silicon thickness.

The downstream momentum spectrometer must momentum analyze all daughters and track undecayed beam particles out of the decay volume. Minimum material is particularly important here, and the instrumented area required is $\sim 0.6\text{ m}^2$. The tracking technology of choice is straw tubes in vacuum with either a geometrical hole or deadened wires in the beam region. The magnet requirements are a $1 \times 1\text{ m}^2$ aperture with a p_T kick of $200\text{ MeV}/c$. This requires a 0.6 T field for a 1 m effective length. The beam hole costs some acceptance but the beam rate is too high for straw technology to handle with high efficiency. We have considered and rejected a fiber tracker since multiple Coulomb scattering alone from even thin ($500\text{ }\mu\text{m}$) fibers is larger than the resolution required. There is a final plane of fiber tracker to track the beam and provide a high resolution time measurement on each track. The straw tube occupancy and rates are high but tolerable, while the material is as low as practical. This straw tracker must be located in the vacuum of the decay volume; multiple windows would be prohibitive in terms of material in the beam. This is a significant engineering challenge.

The momentum spectrometer provides completely redundant measurements of track vector momenta and times which can be compared to the complementary vector velocity and time measurements provided by the velocity spectrometers described below.

The momentum spectrometers have demanding performance parameters but are fundamentally conventional tracking magnetic spectrometers. The tracking technologies are much slower in resolving time and time resolution than the velocity spectrometers. These systems drive us to require a separated beam to keep the rates seen by these detectors within acceptable limits. Without the redundant measurements they provide the required level of background rejection is unachievable.

3.4.2 The Velocity Spectrometer

The “Velocity Spectrometer” is the most novel component of the CKM apparatus, which measures the *velocity* vectors of the incoming K^+ and the exiting π^+ . This high speed, essentially isochronous detector system measures K^+ and π^+ kinematics completely independent of the Momentum Spectrometer. The mis-reconstruction mechanisms of the Momentum and Velocity spectrometers are essentially orthogonal, which is a critical requirement of genuinely redundant detector systems.

The velocity spectrometer is composed of two phototube based “Ring Imaging Cherenkov” (RICH) systems, the “kaon RICH” and the “pion RICH” shown in figure 10. Conventional RICH systems operate well above the turn-on momentum threshold and primarily serve to separate particle species by mass. The CKM RICH systems in contrast operates in a momentum band centered on the RICH turn-on thresholds where the ring radii depend sensitively on the velocities. The π^+ and K^+ threshold curves of the kaon RICH are shown in figure 4, and in figure 22 for the pion RICH. The principles and sensitivity of the Velocity Spectrometer are determined by the simple formulae below.

Another significant difference between the CKM RICH systems and most of the previous large RICH detector systems is the Cherenkov photon detection technology. The significant challenge associated with realizing large RICH detectors based on gaseous detection of the Cherenkov photons is well known in the field. The speed requirements of the CKM RICH essentially requires the use of photomultiplier tube based photon detection. Although this is an apparent cost liability at the outset, the requirement of phototube readout has the enormous advantage that the photon detection system is built from one of the most reliable and well understood detector components available. Indeed, the recent high performance [67] [68] of the large phototube based SELEX RICH system

and earlier phototube based RICH systems (SPHINX) [40] bears this out.

In a Ring Imaging Cherenkov detector, the basic formulas apply:

$$\cos \Theta_c = \frac{1}{\beta \cdot n} \quad (12)$$

Θ_c denotes the Cherenkov angle, β is the velocity of the particle relative to the velocity of light in vacuum, and n is the refractive index of the medium.

$$N_{\text{det}} = N_0 \cdot L \cdot \sin^2 \Theta_c \quad (13)$$

N_{det} is the number of detected photons, which is given by a proportional constant N_0 , and the length of the radiator L . The spectrum of the Cherenkov Photons is given by

$$\frac{dN}{d\lambda} \propto \frac{1}{\lambda^2} \quad (14)$$

In a RICH detector the photon are focused onto a ring of radius r , which is given by

$$r = \frac{R}{2} \cdot \tan \Theta_c \quad (15)$$

R denotes here the radius of the spherical mirror. In figure 4 we illustrate equation 15 for a RICH detector with $R = 40$ m, and $n = 1.000287$.

The ring radius resolution is inversely proportional to $\sqrt{N_{\text{det}} - 3}$, which alone suggests that the largest ring radii produce the best momentum resolution. From figure 4 it is clear however that dr/dp decreases with increasing ring radius, which degrades the momentum resolution. Other contributions including multiple scattering in the RICH gas and chromatic dispersion (the dependence of the refractive index on the wavelength $n = n(\lambda)$) must also be considered in optimizing the overall resolution.

3.4.3 The Kaon Entrance Angle Tracker System (KEAT)

The material upstream of the vacuum decay volume illustrated in figure 10 corresponds to $\sim 8\%$ of a radiation length which significantly alters the K^+ entrance angle on the scale of interest. A two-plane tracking system is employed in the vacuum to precisely measure the entrance angle of the beam particle measured and tagged as a K^+ by the kaon RICH. This system must have minimal mass and have rate capability adequate to precisely track beam particles.

3.4.4 The Beam Interaction Veto System (BIVS)

Incident K^+ particles can scatter inelastically in the material upstream of the vacuum decay volume, including the KEAT system. These inelastic scatters include charge-exchange into a K^0 , which can subsequently decay via $K_L \rightarrow \pi^+ e^- \nu$ into a high momentum pion and a very soft electron. Likewise, an incident K^+ can charge exchange into a fast forward pion and a K^0 . The fast forward pion can mimic the $K^+ \rightarrow \pi^+ \nu \bar{\nu}$ signature, and hence the BIVS must be efficient for soft electrons, photons, neutral hadrons, as well as other particles associated with the inelastic collision. The Beam Interaction Veto System instruments the majority of the solid angle forward of the last plane of material before the decay volume.

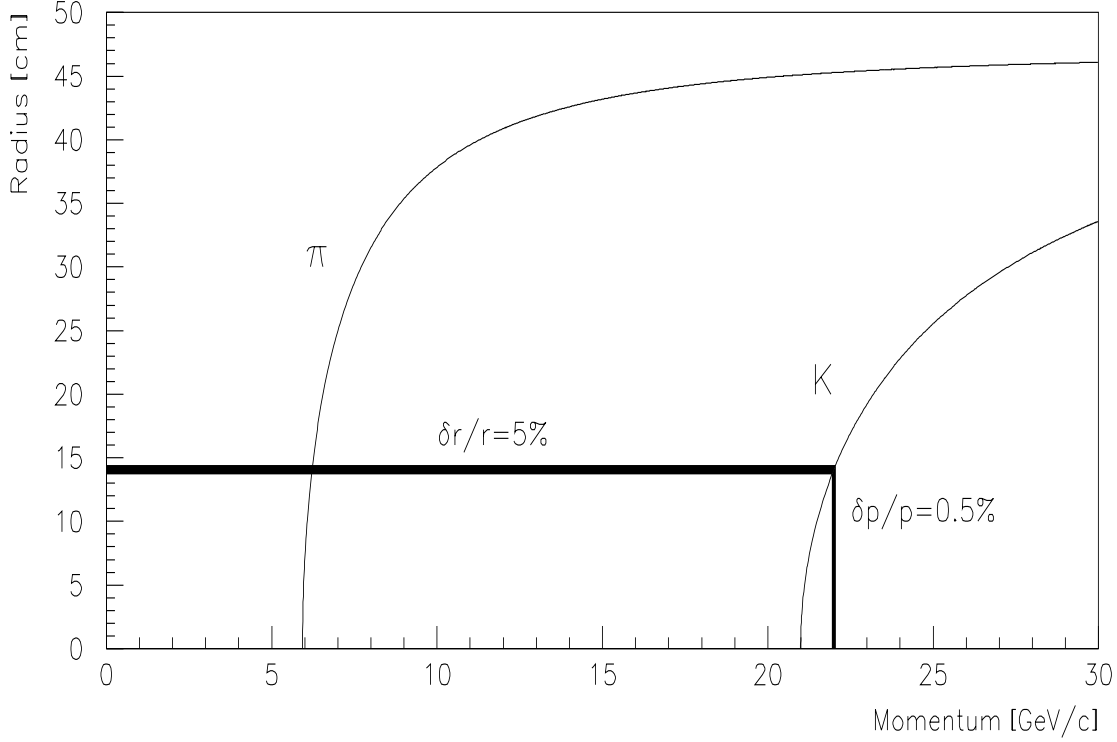


Figure 4: Ring Radii for K^+ and π^+ versus their momentum for the kaon RICH system that measures the incident beam K^+ momentum and decay angle. The black band indicates the momentum resolution of the kaon RICH system described later in section 5.3. Assumed is $R = 40$ m and $n = 1.0002765$.

3.4.5 The Photon Veto Systems

One of the most challenging detector issues facing CKM is the efficient detection of all photons produced by background events along the 20 m long vacuum fiducial decay region shown in figure 10. Complete hermeticity and efficient photon detection down to energies as low 10–20 MeV is required. In addition to photon detection, the veto systems must efficiently tag minimum ionizing particles and charged particles with $\beta, (\frac{v}{c})$ as low as 0.97. The KAMI experiment that proposes to measure $K_L \rightarrow \pi^0 \nu \bar{\nu}$ faces a similar challenge, and we have benefited greatly from their past and ongoing photon veto R&D efforts. Due to the similarity of photon veto requirements, the conceptual designs presented in this proposal are largely taken from the analogous discussion in the KAMI Expression of Interest [41].

The required level of photon veto inefficiency for CKM was determined by iterative studies of the $K^+ \rightarrow \pi^+ \pi^0$ and $K^+ \rightarrow \mu^+ \nu_\mu \gamma$ backgrounds described in sections 7.3.1 and 7.3.3. The performance required to limit these backgrounds to a negligible level is listed in table 4 for the Vacuum Veto, (VVS), Forward Veto, (FVS) and Hole Veto (HVS) Systems illustrated in figure 10. The analogous performance required for KAMI to control backgrounds which are dominated by $K_L \rightarrow \pi^0 \pi^0$ is listed in table 5. It is clear that the required KAMI veto performance is considerably more stringent than CKM, and that CKM will gain from the ongoing ambitious R&D effort to reach the KAMI level of

performance [41] is listed in table 5.

One significant KAMI photon veto challenge that CKM doesn't share is the required veto performance in the beam hole region. In KAMI the high intensity (200 MHz) neutral beam intercepts the beam hole veto system which severely complicates the task of rejecting photons, particularly at low energy. This difficulty is reflected in the inefficiency at low energy in table 5. In contrast the charged CKM beam is kicked away from the beam hole veto system before intercepting it, which affords higher (although still intermediate) veto efficiencies in the forward beam direction. The intermediate efficiencies listed for the CKM beam hole veto are the result of two effects. The first effect is pileup of low-energy photons that result from beam interactions with the pion RICH material which will no doubt raise the effective veto threshold. The second effect arises from conversion of decay photons in the pion RICH material that are then swept away from the hole veto system by the beam kicker magnet. The majority of these conversions are detected by the "Charged Veto Plane" that instruments the upstream face of the beam kicker magnet.

Photon detection inefficiency at low energy is dominated by sampling effects, where the energy deposited in active material can fluctuate below the sensitive energy threshold. At high energy the inefficiency is dominated by photonuclear absorption, where it is possible for a photon to experience a photonuclear absorption interaction before it begins to shower. If all of the secondary products in the interaction are neutrons and/or very low energy nuclear fragments that range-out in inactive material, the interaction may escape detection. Photonuclear absorption has been studied extensively in the past in various energy regions [42].

A photon veto detector for CKM will likely be based on the existing KTeV veto design. However, in order to improve detection efficiency for low energy photons, both finer sampling and more scintillation light are required. The cost of such a detector is of primary concern and a good deal of effort has gone into designing a low-cost device. The current conceptual design is described in some detail in section 5.7.

Energy Low-High (GeV)	(VVS) Inefficiency	(FVS) Inefficiency	(HVS) Inefficiency
0.0 - 0.02	4×10^{-1}	1	1
0.02 - 0.04	3×10^{-2}	5×10^{-1}	1
0.04 - 0.06	3×10^{-3}	5×10^{-2}	1
0.06 - 0.10	7×10^{-4}	5×10^{-3}	1
0.10 - 0.20	4×10^{-4}	2×10^{-3}	2×10^{-2}
0.20 - 0.40	1×10^{-4}	5×10^{-4}	5×10^{-3}
0.40 - 1.00	1×10^{-4}	2×10^{-4}	2×10^{-3}
1.00 - 3.00	3×10^{-5}	1×10^{-4}	2×10^{-3}
3.00 - 10.0	3×10^{-5}	3×10^{-5}	2×10^{-3}

Table 4: Required inefficiency performance of the CKM photon veto systems.

3.4.6 The Muon Veto System

Muon rejection in CKM is critical to background rejection. Studies of potential backgrounds from $K^+ \rightarrow \mu^+ \nu$ and $K^+ \rightarrow \mu^+ \nu \gamma$ have shown that muon rejection of 1×10^{-5} or better is needed for muons with momentum above 14 GeV. Our design goal for a muon veto system will exceed 1×10^{-5} by a conservative safety factor.

Energy Low-High (GeV)	(VVS) Inefficiency	(FVS) Inefficiency	(HVS) Inefficiency
0.0 - 0.02	2×10^{-1}	1	1
0.02 - 0.04	3×10^{-2}	1×10^{-1}	1
0.04 - 0.06	3×10^{-3}	1×10^{-2}	1
0.06 - 0.10	7×10^{-4}	1×10^{-3}	1
0.10 - 0.20	4×10^{-4}	4×10^{-4}	1
0.20 - 0.40	1×10^{-4}	1×10^{-4}	1
0.40 - 1.00	3×10^{-5}	3×10^{-5}	1×10^{-1}
1.00 - 3.00	3×10^{-6}	3×10^{-6}	1×10^{-2}
3.00 - 10.0	1×10^{-6}	1×10^{-6}	1×10^{-3}

Table 5: Required inefficiency performance of the KAMI photon veto systems.

The most common version of the problem of $\mu:\pi$ separation is that of trying to positively identify directly produced muons in an environment where pion decays contribute a background. This is the problem, for example, in a $K_L^0 \rightarrow \mu^\pm e^\mp$ search where decays of K_{e3} pions are a source of background events, or in a collider experiment attempting to use prompt muons to tag heavy quark decays. In these cases misidentification probabilities of a few percent are typical. In CKM the problem is the reverse. The requirement is to avoid misclassifying a muon as a pion. Fortunately, if a pion decays to a muon, that does not introduce background in CKM; rather it introduces a small inefficiency.

It is possible to reject muons well below the 1×10^{-5} level. The technique relies on the penetrating nature of muons versus pions. For example, a one meter thick iron absorber followed by a hodoscope can accomplish this task since most muons will penetrate and make signals in the hodoscope, while only a few pions will create such signals (via the punchthrough of cascade particles from the pion’s hadronic interaction). Those pions producing such false muon signals introduce an inefficiency, not background. The limitation on this technique is that not all muons penetrate the iron absorber. Some decay inside the absorber and others catastrophically lose a large fraction of their energy — most often but not exclusively via bremsstrahlung — and then range out in the absorber. These occurrences will fake the pion signature.

By longitudinally segmenting the absorber and instrumenting the layers, it is possible to improve the muon rejection considerably. Muon decays produce electrons which will typically induce observable electromagnetic showers. Most catastrophic energy losses will induce observable electromagnetic showers. Only a small fraction of muon interactions induce hadronic showers similar to those associated with pion interactions. That is, by standard techniques for discriminating between hadronic and electromagnetic showers, it is possible to enhance the muon rejection by a large factor. The ultimate limitation on this technique comes from the cross section for inelastic muon scattering on nuclei which creates hadronic showers.

The probability for a 14 GeV muon to decay in 1 meter is 1×10^{-5} . The probability of an interaction can be estimated from the bremsstrahlung cross section, since bremsstrahlung is the dominant interaction process. It is useful to define the “inelasticity” y of the muon interaction, $y = E_{\mu(\text{initial})} - E_{\mu(\text{final})} / E_{\mu(\text{initial})}$. If the depth of the absorber corresponds to 1 GeV of energy loss (roughly one meter of iron), then a 14 GeV muon must interact with $y > 13.5/14 = 0.96$ (assuming it interacts half-way through the absorber) in order to be lost. The bremsstrahlung cross section as

a function of $E_{\mu(\text{initial})}$ and y is given by [43]:

$$\frac{d\sigma}{dy} = \alpha Z^2 r_e^2 \left(\frac{m_e}{m_\mu} \right)^2 \frac{4}{y} \left[1 + (1-y)^2 - \frac{2}{3}(1-y) \right] \left[\ln \left(\frac{2E_{\mu(\text{initial})}}{m_\mu} \frac{\hbar}{m_\mu r_n} \frac{1-y}{y} \right) - \frac{1}{2} \right], \quad (16)$$

where r_e is the classical radius of the electron and $r_n = 0.49r_e A^{1/3}$. From this we can estimate the probability of a muon bremsstrahlung with $y > 0.96$ in 1 m of iron to be about 7×10^{-6} .

We conclude therefore that the muon rejection of a simple 1 m iron absorber followed by a hodoscope is about 2×10^{-5} . This is not as good as CKM needs, but can be improved upon by having an active absorber with multiple hodoscope layers (every 2-4 X_0) rather than a passive one, so that the characteristic shape of electromagnetic showers created by these muons can be observed. The irreducible misidentification comes from muon interactions which produce hadrons and consequently hadronic showers. This process is more than an order of magnitude smaller than bremsstrahlung, so that muon rejection better than 1×10^{-6} should be possible.

In view of this discussion, the CKM muon veto system should consist of a relatively short range stack instrumented longitudinally to provide shower shape information. Transverse segmentation will be driven by rate considerations. A traditional arrangement of iron and scintillator would be suitable, for example, provided it is free of cracks and dead material that could permit energy deposits to go unobserved. An additional complication is provided by the forward photon veto system which is immediately upstream of the muon veto system. The photon veto is where the pions (or muons) will first see significant material and begin to interact. The gap between these detectors must be small (to minimize shower blooming and muon decays) and the gap should not contain passive material which could absorb particles. These constraints must be met in the design of both systems.

3.5 Stopped versus In-flight Kaon Decays

All prior searches for $K^+ \rightarrow \pi^+ \nu \bar{\nu}$ have utilized stopped- K 's [38]. We are aware of a few instances of in-flight experiments being considered in the past, but before the 1989 Main Injector Workshop report [39] nothing seems to have been written down. A comparison of the two methods is not simple, since some subjective factors (such as how much weight to put on the accumulated experience using the stopped- K method) enter in. Nonetheless, it is an interesting question which has been discussed within the experimental kaon community for many years. Two developments make the question particularly timely today: (1) the new Main Injector will be able to provide intense K beams during Collider runs and (2) ring-imaging Cherenkov counters (RICHs) have reached a maturity that makes them viable as a core component of an experiment. Fortunately, typical energies of secondary kaons from Main Injector beams are suitable for RICH detectors.

Ultimately the comparison between a stopped- K and in-flight $K^+ \rightarrow \pi^+ \nu \bar{\nu}$ experiment depends on achievable sensitivity and background rejection. We believe an in-flight experiment at the Main Injector has advantages on both scores, but suffers from the possible criticism that, lacking prior experience, there may be unanticipated problems and/or a significant learning curve to surmount. While such criticism can be leveled against any new approach, it should be kept in mind that most kaon experiments have been conducted in-flight, so there is a huge body of experience with the in-flight technique (including rare decay experiments down to near 10^{-12} for some modes).

The branching ratio sensitivity of a rare K decay experiment is simply the reciprocal of the number of K decays which occur during the experiment multiplied by the acceptance for the decay of interest. As described elsewhere in this proposal, CKM will utilize about 5×10^{12} protons per spill (about 15% of the Main Injector) to produce a K^+ beam of 3×10^7 K^+ per spill, of which

about 17% will decay in our decay volume. For a 1.25% acceptance, the branching ratio sensitivity is 1.6×10^{-5} per spill. It is reasonable to expect 1.4×10^5 Main Injector spills per week (120 hours with 3 sec cycle time). Thus, CKM should achieve a sensitivity of about 1.1×10^{-10} per week. In 2 years of running, at 39 weeks per year, CKM would acquire 72 signal events. While 2 years is a very long run for a fixed-target experiment, it should be remembered that this running takes place in tandem with the Tevatron Collider program at low incremental cost.

To put this in context, the BNL E787 experiment has reported the observation of 1 event at the 4×10^{-10} level of sensitivity from their 1995 run, corresponding roughly to 1×10^{-8} per week. Based on discussions with BNL E787 personnel [45], the expectation is that with the current detector it would be possible to collect data at the rate of 2×10^{-9} per week at RHIC after 1999. With upgrades to the detector an addition factor of 4 to 5×10^{-10} per week might be possible. CKM has potentially 5 times better sensitivity. Of course, the price for this is a new detector.

Ultimately, sensitivity may be made irrelevant if backgrounds prevail. There are several aspects to a comparison of background rejection in the stopped- K versus in-flight approaches. We will discuss in turn redundancy, kinematic resolution, particle identification, photon vetos, and strategies for measuring backgrounds with data.

An aspect of BNL E787 which is appropriately emphasized is redundancy. In particular, the π^+ is measured three times: momentum, energy, and range. The momentum is measured by tracking in a magnetic field. The energy is measured by pulse height in an active (scintillator) range stack, which also provides a range. Comparison of the three measurements improves background rejection and relaxing cuts on one can help to understand the effect of cuts on the others. The analogous three quantities in CKM are momentum, velocity, and shower energy. Momentum of both beam particles and charged decay products will be measured by tracking through magnets. Velocities will be measured by RICH's. The shower energy for the charged decay products will be measured in the muon veto system, which is really a calorimeter. We formulate this as a parallel with E787 in these terms simply to make the point that CKM has the same high degree of redundancy in similar quantities.

More important is the fact that CKM will make redundant independent measurements of both the incoming beam particle and outgoing putative π^+ . The "momentum spectrometer" and the "velocity spectrometer" use completely independent hardware to measure vector quantities (magnitude and direction) for both the incoming and outgoing particles. For a given mass hypothesis the momentum and velocity vectors can be compared for consistency. Both measurements will have similar experimental resolutions and each spectrometer separately provides all the information needed to calculate the missing mass in the K^+ decay.

Kinematic resolution is important in a $K^+ \rightarrow \pi^+ \nu \bar{\nu}$ experiment since one wants to reject the two-body backgrounds kinematically. For stopped- K 's this is conceptually simple since the observed charged particles have fixed momentum. Of course, there is no fundamental advantage in the fact that the center-of-mass frame and the laboratory frame are the same. As a practical matter, the stopped- K technique has one clear advantage — the kaon's momentum is known to effectively perfect precision. The value of this information depends on whether other measurements are of sufficient precision to fully exploit it. BNL E787 has about a 2.5 MeV momentum resolution of the π^+ from $K^+ \rightarrow \pi^+ \pi^0$ (out of 205 MeV for the momentum). The energy and range measurements are much less precise in relative terms. In CKM we will reconstruct the missing mass M_{miss} as discussed earlier. For a given value of M_{miss} in any $K^+ \rightarrow \pi^+ X$ decay, the center-of-mass momentum p^* of the π^+ is fixed. Thus, we can compare CKM to E787 by simulating CKM in a Monte Carlo and determining how our expected p^* resolution compares to that achieved in E787. Using the RICHs alone, we expect a 3.0 MeV resolution. Using the tracking (momentum) spectrometer, we expect 3.0 MeV resolution. The combined resolution using both sets of measurements is 2.2 MeV. The

Gaussian resolution, however, is not the whole story, since non-Gaussian tails are the more likely source of background. The tails generally result from scattering, but to the extent that they are due to detector mismeasurement, CKM has the advantage of comparing two measurements with similar intrinsic errors.

Particle identification, in particular avoiding misidentification of a muon as a pion, is very good in both the stopped- K and in-flight situations. In the former the technique is to follow the entire decay chain $\pi \rightarrow \mu \rightarrow e$. In CKM both the RICH and the muon veto system independently provide powerful muon rejection. In the RICH, for example, the ring radii for 20 GeV (the highest momentum of interest) π^+ 's and μ^+ 's differ by 11.6 sigma.

Following the full $\pi \rightarrow \mu \rightarrow e$ decay chain, of course, takes time — a few microseconds to be efficient — while the RICH and muon veto time scales are at most a few nanoseconds.

Key to a $K^+ \rightarrow \pi^+ \nu \bar{\nu}$ experiment is powerful photon vetos, since $K^+ \rightarrow \pi^+ \pi^0$ and $K^+ \rightarrow \mu^+ \nu_\mu \gamma$ must be heavily suppressed based on the photon(s) in the decays. Higher photon energies favor better rejection. However, there is one caveat. A $K^+ \rightarrow \pi^+ \pi^0$ decay at rest never results in a photon below 20 MeV. In contrast, $K^+ \rightarrow \pi^+ \pi^0$ decays in-flight (for 22 GeV K^+ 's) result in photons below 20 MeV (and all the way down to zero) in about 0.1% of decays. Fortunately, since CKM will impose a maximum momentum cut of 20 GeV on the π^+ , the other photon in such decays has energy greater than 2 GeV, making such events relatively easy to veto, at least in principle. While the subject of photon vetos is a very involved one, the higher energies seem to be a net benefit and we believe π^0 rejection of 2×10^{-7} is achievable. BNL E787 has achieved $\sim 1 \times 10^{-6}$ in practice in the stopped- K case, which is limited principally by photonuclear reactions which are significant at low energies.

Another important issue is how backgrounds can be measured in the two approaches. To the extent that scattering or interactions in matter are the sources of backgrounds, the in-flight method has a fundamental advantage. In the case of stopped- K , it is necessary for the incoming K^+ to pass through enough material to stop it, an amount that depends on the K^+ beam energy. In the in-flight case, initially one minimizes the amount of matter traversed by the particles. Of course there is some practical lower limit which sets the level at which the background processes will occur. The advantage of the in-flight technique is that material can be added to the paths of the particles in a controlled way so that the backgrounds can be measured directly as a function of the amount of material. Since one cannot change the amount of material that stops a given K^+ , we believe this tool is lacking in a stopped- K experiment. Likewise, the range stack in E787 that stops the π^+ is a major piece of the detector and cannot be varied to enhance pion interactions in matter. We believe this is a major advantage of the in-flight technique.

The alternative, of course, as employed in E787 is to study backgrounds by varying cuts. To the extent that different cuts reject the same background, one can estimate the background level by relaxing the cuts in an astute way, determining the rejection of each cut separately, and then combining the separate rejections into a final background estimate. This depends rather strongly on the cuts being uncorrelated in their effects. All of these techniques are available to CKM.

In summary, considerable experience exists with the stopped- K approach to $K^+ \rightarrow \pi^+ \nu \bar{\nu}$ and BNL E787 could run during the RHIC era at BNL. Our estimate is that CKM using the in-flight technique at the Main Injector can accumulate sensitivity at a rate about five times faster per unit of running time. Backgrounds are the real issue. Clearly, CKM must have background rejection commensurate with its sensitivity. We discuss background estimates in detail elsewhere in this proposal. Our conclusion is that the in-flight technique has several potential advantages over the stopped- K method. These include powerful muon rejection at high rates, better photon rejection, and the opportunity to directly measure the dominant backgrounds. Because it is possible to combine a conventional magnetic momentum measurement with a RICH-based velocity measurement, unprecedented redundancy in measuring the kinematic quantities of interest is also possible.

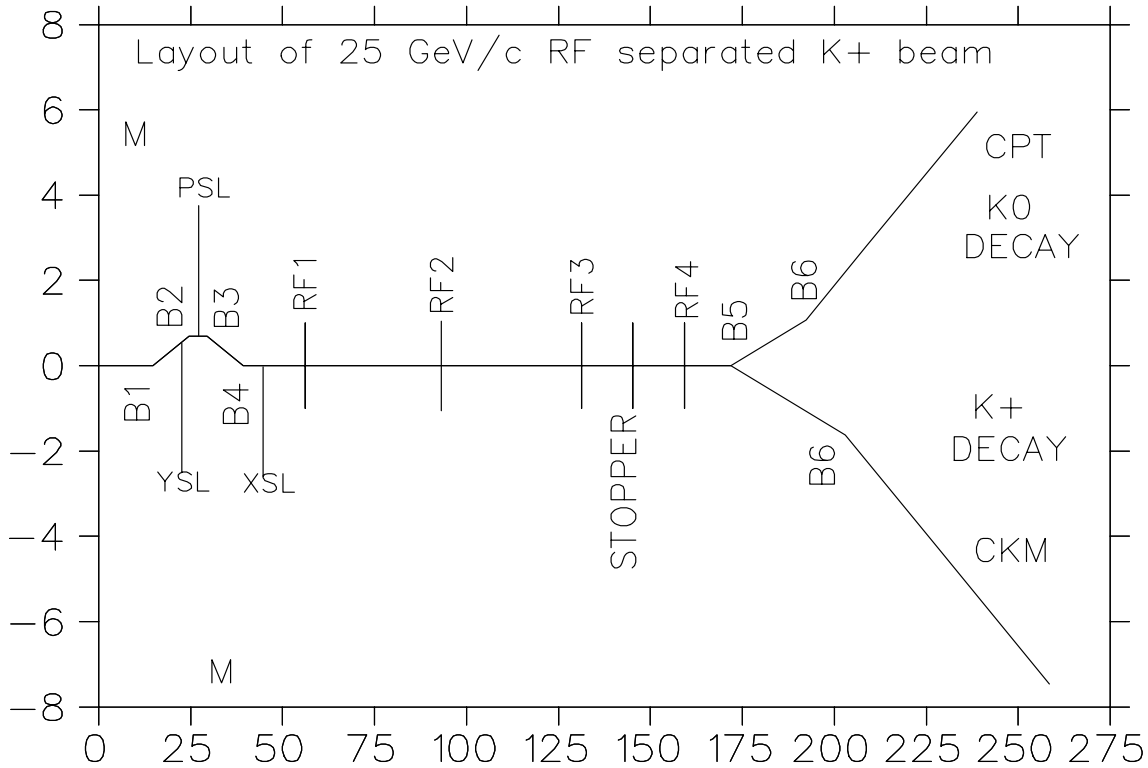


Figure 5: Schematic layout of the beam line, distances in meters, reproduced from [46].

4 The Separated Charged Kaon Beam

4.1 Design Motivations of the Separated Beam

CKM requires a beam in which charged kaons are the majority particles. At our beam energy this can only be achieved via RF separation. G. Thomson and his co-workers on the CP/T experiment initiated work on an RF-separated beam design for the Main Injector some time ago. In particular, J. Doornbos (TRIUMF) has written a design note [46] “Optics Design of a 25 GeV/c RF separated K^+ beam.” While 25 GeV is not a suitable beam energy for CKM, we have adopted the basic design as a starting point for the CKM beam. The design is flexible enough to accommodate both experiments through placement of a switching magnet in the downstream portion of the beam, as shown in figure 5. Of course the two experiments could not run simultaneously, and providing the capability of running at more than one momentum would likely add complexity and cost to the design.

This beam can provide 30 MHz of ~ 22 GeV K^+ with an estimated contamination of less than 10% π^+ with 5×10^{12} protons per spill incident on the production target. The beam divergence envelope is $\pm 100 \mu\text{rad}$ and the momentum bite is about $\pm 1\%$. The lower rates afforded by this beam purity allow charged particle tracking in the beam which is crucial for measurement of $K^+ \rightarrow \pi^+ \nu \bar{\nu}$.

4.2 Design Motivations for a Debunched Beam

In this high rate environment it is advantageous to minimize the instantaneous rate by debunching the 53 MHz beam structure. Some of the time variation of the beam must remain in order for the RF pickups to measure beam positions. The debunching of the beam has been discussed with the

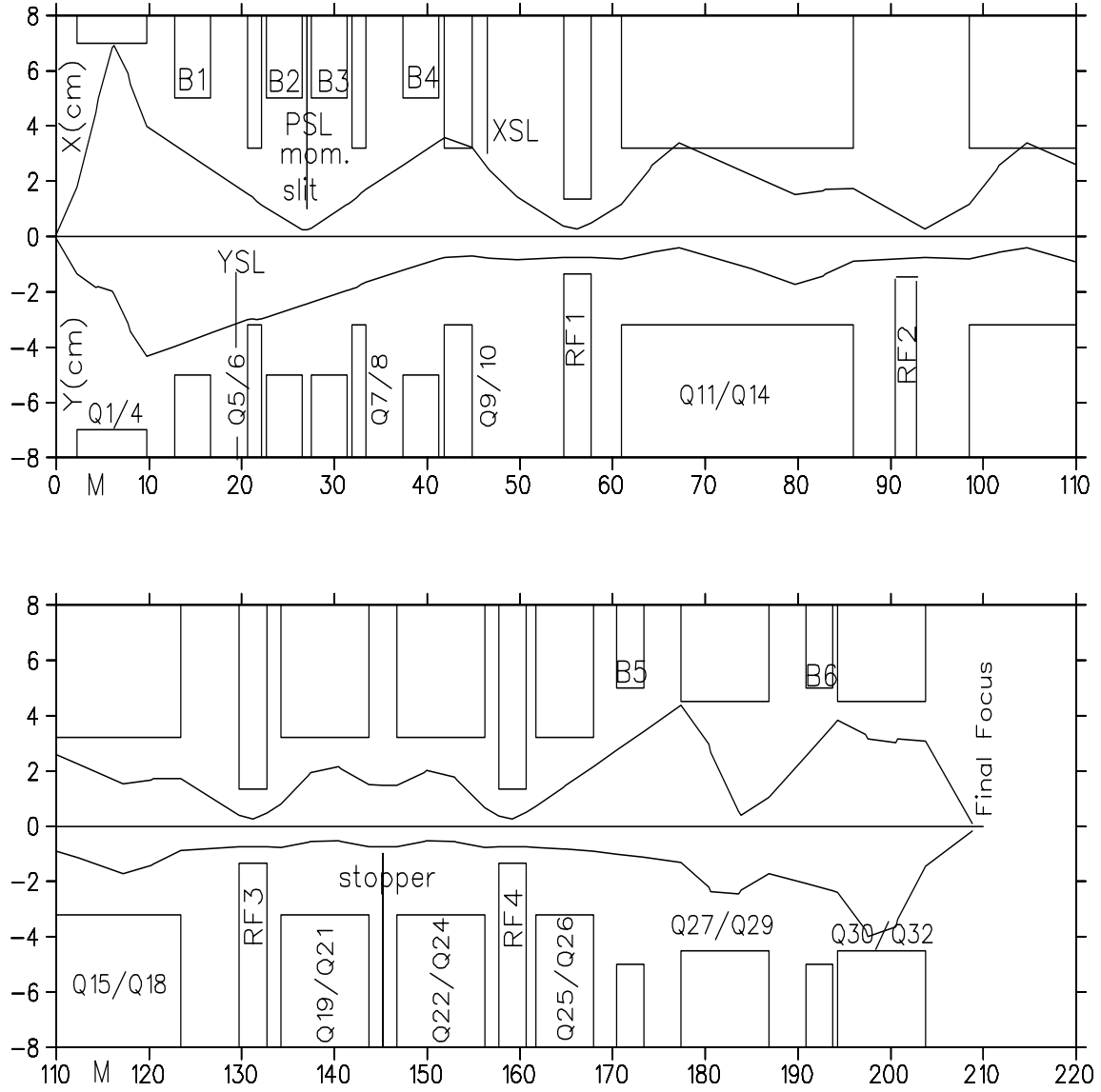


Figure 6: Beam envelopes for the CP/T beam. The tune of the CKM beam is the same until RF4. The apertures of the beam line elements are indicated, distances are in meters. Reproduced from [46].

Main Injector accelerator experts at the May 1997 “MIST” workshop on fixed target physics at the Main Injector [47]. Two different schemes to minimize the RF structure were discussed [48]. These RF manipulations may add 10% to the cycle time and care must be taken to avoid beam loading effects in the cavities which maintain the RF structure.

4.3 K^+ Flux and $K^+ / (\pi^+, p^+)$ ratio estimates

The motivation for running with a K^+ beam rather than K^- is proton economics. Estimates from several sources indicate that the K^+ yield for 22 GeV/c incident protons is about twice the K^- yield [49, 50, 51]. An RF separated beam line based on C-band (5.8 GHz) cavities is 225 m long, and 5×10^{12} protons on target yield 3.0×10^7 K^+ /sec (spill) at the detector. Without particle separation the detector would see a π^+ / K^+ ratio of $\times 34$ and a p^+ / K^+ ratio of $\times 13$ at this distance. For the S-band (2.9 GHz) solution the beam length increases to 300 m and particle ratios suffer as a result. For the S-band configuration the π^+ / K^+ ratio is $\times 43$ and the p^+ / K^+ ratio is $\times 21$ at the detector. Our working requirement for beam purity is twice as many K^+ as other particles. This leads to a required separator enhancement of $\times 94 (\times 128)$ for C-band (S-band) configurations respectively. The only other superconducting RF separated beam built [52] achieved an enhancement of $\times 31$ at 16 GeV/c. Both the CKM and CP/T experiments require significantly better enhancement.

4.4 Motivation and Issues for Negative Beam Operation

While proton economics favors a positive beam, the possibility of reducing the non-K component by simply running with a negative beam is attractive. At production using the Malensek [51] parameterization the p^- / K^- ratio is ~ 0.3 , however after 225 m and the subsequent K decays the ratio of p^- / K^- at the experiment is ~ 1.6 . In principle the RF separator scheme could be simplified by focusing on mainly eliminating pions as opposed to both pions and protons. In a 2-cavity scheme there are certain momentum bands where both pions and protons cannot be separated. Doornbos’s recent work [46] describes how a 3-cavity scheme would allow a more flexible scheme which would work at all beam momenta. In fact, this is Doornbos’s proposed solution if CP/T and CKM must operate at different energies. Most likely we can at some small additional expense of reversing switches on the beam line magnets choose to run either positives or negatives. The beam dump should be designed to work in either case. More complete ongoing studies of non-kaon contamination are needed to understand the trade-offs.

4.5 Comparison to other RF separated beams

The use of RF to separate particles is not new. Some of the original work we found are proposals by Panofsky [53], Montague [54], and Schnell [55] for two-cavity schemes. In 1965 two-cavity RF separated beams were in use at the AGS [56] and CERN [57]. Later at CERN in 1967 a 3-cavity separator system was successfully in operation [58]. An excellent review of the early activity in the field is given by P. Bernard [59]. In particular, for the 1967 CERN 3-cavity beam line (U3) the particle enhancement (desired species/background) for a K^+ 19.2 GeV/c beam was $\times 700$. The observed ratio of desired particles to all particles was 80%. The background particles were 15-20% muon and 3-5% hadrons. The inter-cavity distance was 50 m, and the cavities operated at 2.9 GHz (S-band). However the pulse length of the RF separator did not exceed 8 microseconds, restricting the separation to very low duty-factor beams. The very high rate nature of the CKM experiment requires the relatively large duty factor of the Main Injector (30%). The 1-second long Main Injector spill leads to the use of superconducting RF separators from power consumption considerations.

As described earlier a superconducting RF separated beam was built at CERN in 1978 [52]. There a two-cavity scheme was operated at S-band with an 83 m inter-cavity distance. The design goal for the these cavities was 2 MV/m compared with achieved values of 1.2 – 1.4 MV/m. The enhancement factor observed for K^-/π^- was $\times 31$ at 16 GeV/c.

4.6 Overview of the 3-stage Design

4.6.1 Stage-1: Collection and Optics Preparation

The first stage (see figures 5 and 6) consists of a quadrupole triplet Q1 – 4 with a large aperture (radius = 7.62 cm) which collects up to ± 7 mrad horizontally and ± 4.5 mrad vertically. Following the triplet is a set of four 4 bends defining momentum selection. Collimators in Stage-1 restrict momentum, horizontal and vertical angles. The primary proton beam can be dumped just after B1. Q5 and Q6 are vertically focusing quadrupoles that are used to tune the beam to the first RF cavity which has a radius of 2.7 cm for the C-Band solution. Q6 and Q7 are horizontally focusing quadrupoles added to make the beam achromatic (*i.e.* independent of momentum at the small aperture of the first cavity). Finally Q9 and Q10 focus the beam on the first cavity. At RF1 the maximum vertical angle 4.5 mrad becomes 0.45 mrad. This is much smaller than the maximum deflection of RF1 which for $2\text{ m} \times 20\text{ MeV}/c$ is 0.8 mrad. Horizontally the beam is controlled well enough to fit the next quadrupole Q11 even though it is horizontally defocusing.

4.6.2 Stage-2: RF Separation

In the simplest RF separation scheme only RF1 and RF3 are needed. For C-band (5.8 GHz) cavities the period between RF1 and RF3 is 172.5 psec for the 75 m separation. The time-of-flight difference between pions and kaons at 25 GeV is 45 psec or 93.6 degrees. The difference between protons and pions is ~ 360 degrees. Q11-Q18 provide a unitary transformation matrix between RF1 and RF3. So for pions (and protons) the angular kick from RF1 is preserved to RF3 where it gets an equal and opposite kick which cancels the kick from RF1. For kaons which arrive 45 psec later from RF1 to RF3 there is no cancellation and the kaons are fanned out vertically after RF3. A quadrupole triplet Q19-21 transforms this angle into a position at the beam stopper as show in figure 7. Pions and protons are dumped in the beam stopper and a large fraction of the kaons pass around the stopper. Care is taken in the optics [46] so that the position at the stopper depends only on the angle and not the y position at production target or RF3. The beam at the stopper is parallel in both x and y which is important to minimize leakage since the stopper vertical width is small ~ 1 cm.

In general it is not possible to separate out pions and protons at all momenta with 2 cavities [46, 59]. If CKM and CP/T cannot run at the same beam energy then a 3-cavity solution is required to achieve the same separation at different momenta, and this is the purpose of RF2. The optimum frequency is the highest that is practically achievable. If for example, S-Band (2.9 GHz) cavities were used instead of C-Band, then the RF separation stage would grow in length from 75 m to 150 m. The kaon yield per proton would drop by $\sim 30\%$ due to more kaon decays in the longer beam line. Additional quadrupoles would also have to be added to the beam transport.

4.6.3 Stage-3: Transport to the Experiment

In the current design after the RF separation stage the beam has a dipole switch (B5) which depending on polarity sends the beam to CKM or CP/T. The transport properties for CKM and CP/T differ significantly. CKM requires a nearly parallel ($\pm 100\text{ }\mu\text{rad}$) beam while CP/T must focus the K^+ beam on to a charge-exchange target to produce neutral kaons. The challenge is to

control the large vertical divergence introduced by the RF separation section. With the beam system described, kaons enter the CKM decay region still separated into two lobes in position vertically. With an additional RF cavity (RF4) it is possible to recombine the beam into a single spot with much better optics and cleaner transport. Recombining the beams can also significantly improve the kaon yield per proton. In all our simulations to follow we have assumed the recombined beam configuration. The spatial distribution and divergence of the kaon beam transported to the CKM experiment is shown in figure 8 with and without the RF4 recombination cavity. The momentum distribution of kaons at the CKM experiment is also shown in figure 9 with and without the RF4 cavity.

Adaptation of the Doornbos design to Fermilab magnets and locations has been done [61]. All magnets have been identified and a small number need to be re-gapped. The location of the beam line and the CP/T and CKM experiments looks feasible in either the Meson East or Meson Test beam tunnels with some civil construction needed in either location.

4.7 The Superconducting RF separator system

Superconducting S-band (2.9 GHz) cavities are a mature technology which would require little R&D development [60]. However, there are compromises to the K^+ flux and beam purity as discussed above. The C-band technology requires R&D. Together with the CP/T group we have been working with the Fermilab Beams Division to determine and initiate an R&D plan. This plan was outlined in a presentation [62] on January 9th to the Fermilab Physics Advisory Committee. A list of R&D goals from that report follows:

1. Conceptual design choices, how to achieve 10 MV/m per cavity.
2. Test the (4.7 GHz) TM110 transverse mode of an existing 2.9 GHz S-band cavity.
3. Understand the cryogenics power demands, initial estimates are ~ 100 Watts/m at 5.8 GHz.
4. Address possible construction problems associated with the number of cells and the operating modes.
5. Cavity shape and fabrication alternatives and associated equipment.
6. Model cavity fields and test.
7. Prototype, test, and RF system development.

4.8 Beam Line Muon and Separator Backgrounds

There are several sources of background in the detector from the beam. Muons arise from primary protons interacting in the production target and the beam dump, pion decays upstream of the stopper and kaon decays all along the beam line which produce about 6 MHz of muons at the entrance of the experiment. From kaon decays in the detector we expect an additional 6 MHz of muons which will illuminate the downstream elements of the apparatus. Our goal is to reduce the entrance muons to significantly less than the 6 MHz detector rate, and this can be achieved with judicious upstream shielding placement.

Muon backgrounds also arise from interactions in the beam collimators, (at least one momentum slit and two angle slits), RF cavities, as well as any scrapping along the beam channel. In addition, direct interactions of the beam with RF cavity windows, the beam tagging system, and detector material in the beam can produce muons and other background particles. Our CP/T colleagues have

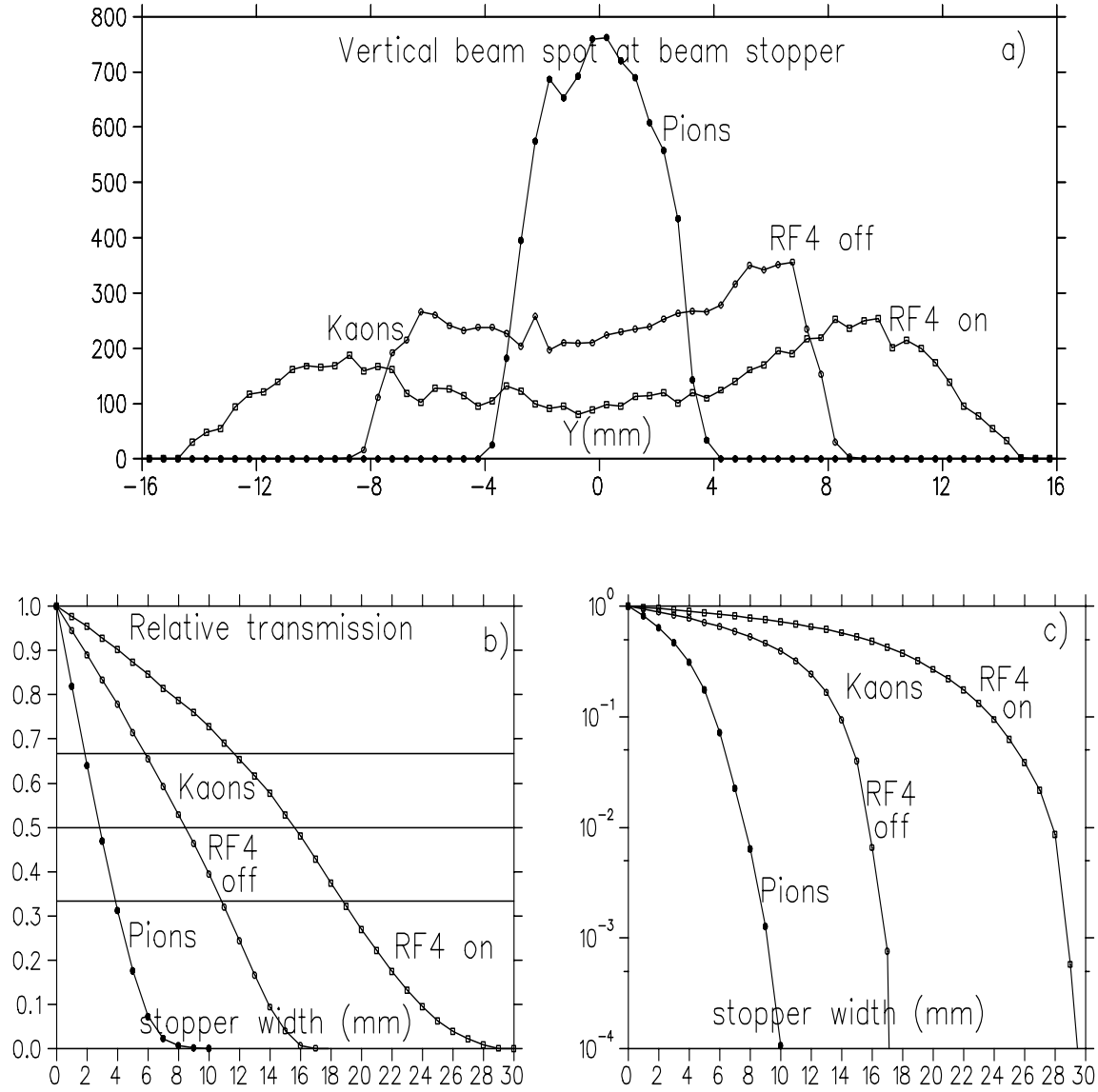


Figure 7: (a) Vertical beam spot at the beam stopper. (b,linear) (c,log) The transmission as function of the width of the stopper (nominally 10 mm), for the CKM beam. Reproduced from [46].

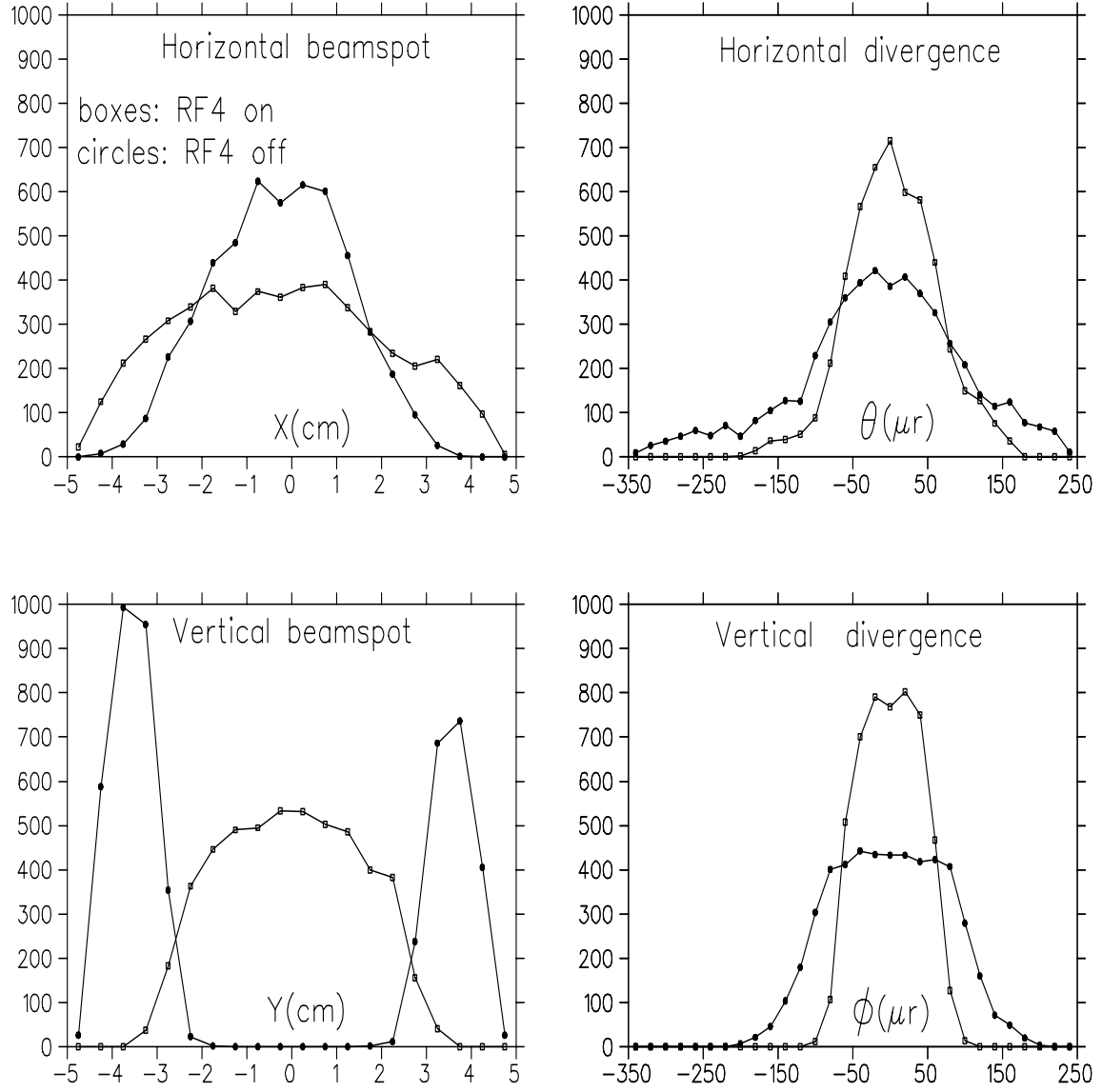


Figure 8: Beam profiles and beam divergence at the entrance of the CKM decay volume. Reproduced from [46].

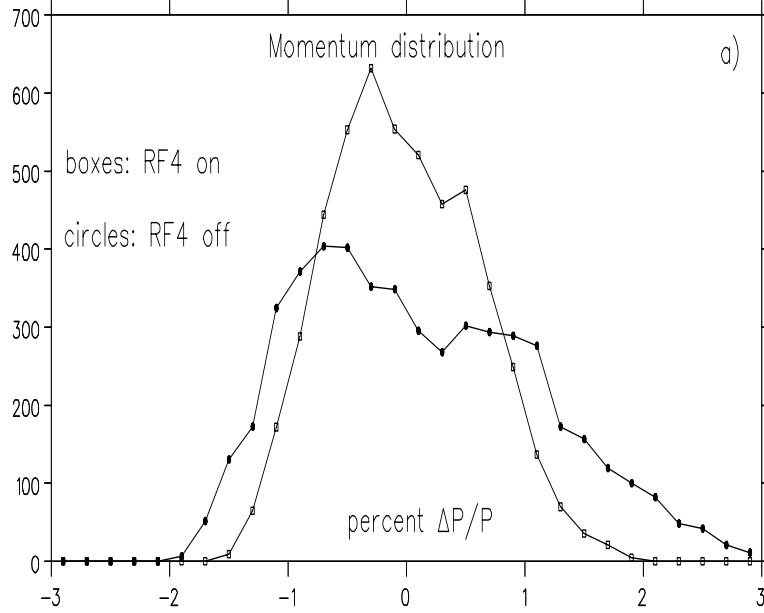


Figure 9: The beam momentum distribution at the entrance of the CKM decay volume. Reproduced from [46].

investigated both the beam stopper and window-collimator background sources. Their results [63] suggest that the stopper backgrounds are very small while upstream scattering in the collimators can be more troublesome. Preliminary estimates [46] are $\sim 15\%$ contamination for standard copper collimators for CKM in the recombination mode. Additional collimators placed downstream of the stopper and/or denser collimator materials such as tungsten are expected to make further reductions in contamination.

We will soon begin background calculations based on the beam line described including the details of the Fermilab magnets and collimators available for this beam. We plan to use GEANT for which we have a model of the beam and CKM detector. We will probably also use the standard Fermilab programs: Decay Turtle and HALO to investigate these backgrounds. Eventually we will incorporate the actual beam enclosures and detector area that will be used to include realistic shielding options.

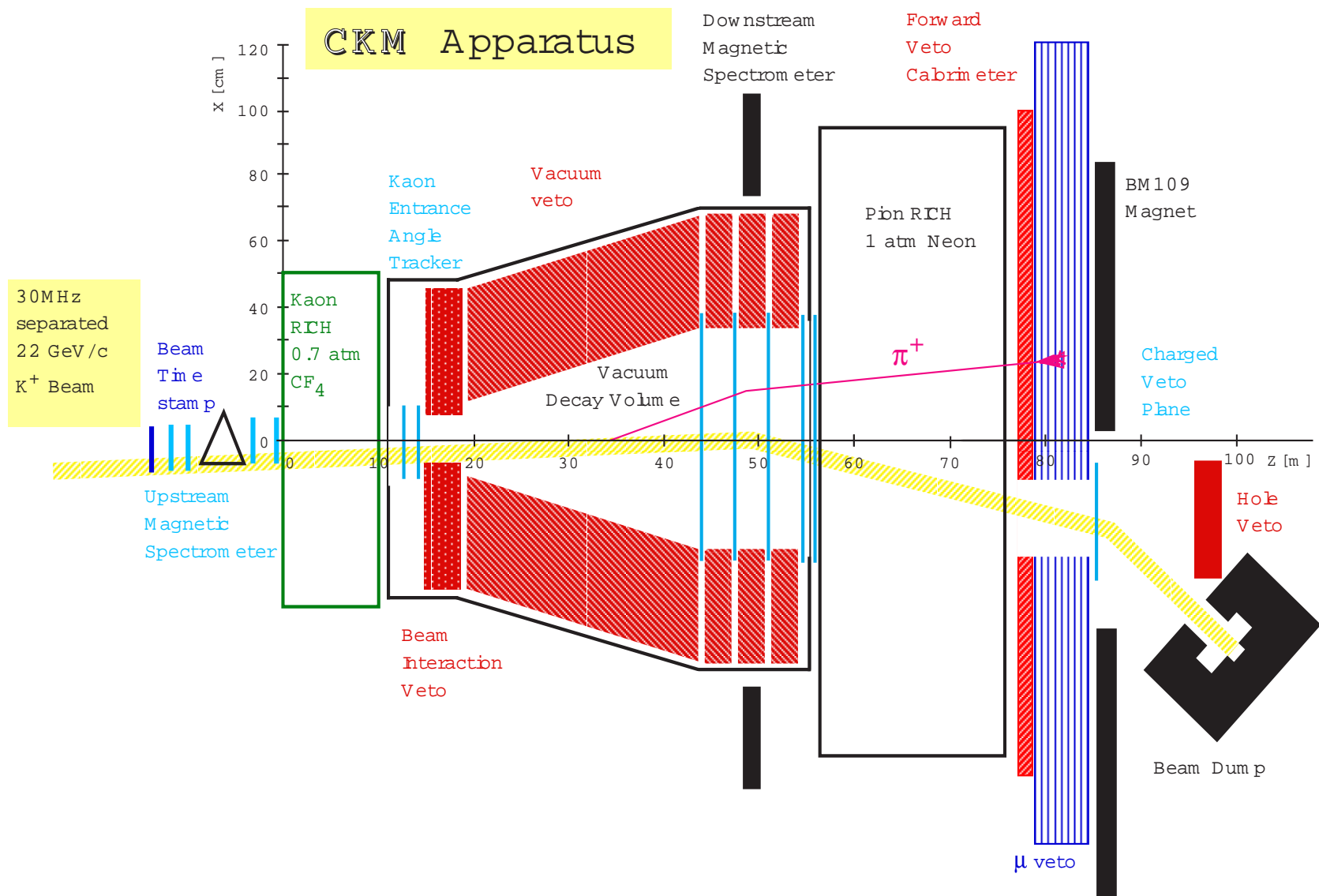


Figure 10: The CKM Detector.

5 The Detector Systems

5.1 Instrumentation Overview of Detector Systems

The guiding principles for the CKM instrumentation are:

1. Very high rate capability in the sub-detectors to fight known and yet to be discovered backgrounds that arise from conspiracies between accidental activity and mis-reconstructions. All detector elements must have deadtimes less than 25 nsec, and provide time resolution of better than ± 1 nsec to reject accidental activity. Detector materials that compose the magnetic and RICH spectrometers must be kept to an absolute minimum in order to reduce beam interaction backgrounds and track scattering.
2. A simple trigger system, designed for an essentially DC beam where any residual microstructure is at the 10% level. (Note: the separated beam RF system will modulate the beam at 2–5 GHz. This very high frequency structure will be invisible to the detectors being considered, and hence not an issue.) The trigger system discussed starts with an asynchronous Level-1 system capable of supporting a deadtimeless rate of 200 kHz. This rate of triggers is fully readout and buffered as input for online filter processors. The buffering and architecture of the online filtering is modeled after the KTeV and SELEX DART applications.
3. A data acquisition system that supports deadtimeless readout of Level-1 triggers that are piped to buffered memory where they are processed by online software filters.

5.2 The Upstream Magnetic Spectrometer

The Upstream Magnetic Spectrometer (UMS) shown in figure 10 must measure the momentum of the ~ 22 GeV beam particles incident on the detector to better than 0.5%. Achieving this resolution within the geometric constraints of the detector requires a track-hit resolution of at least $150\ \mu\text{m}$. The upstream spectrometer must present a minimal amount of material to the beam so to minimize corruption of the momentum measurement. The expected rates, occupancies, and integrated scattering material for candidate tracking technologies are listed in table 6. To minimize scattering and interactions, the tracking detector planes and spectrometer magnet must be integrated into the beam transport vacuum system. Integration of tracking planes into the vacuum beam transport and decay vessels is a significant engineering challenge that CKM must meet for both the upstream and downstream tracking systems.

Of the tracking technologies listed in table 6 Silicon and Mini-drift detectors are most attractive in terms of minimal material and rate capability. These two attractive solutions are additionally motivated by the proven in-field experience of Fermilab experiments E781 (SELEX) [64] and E690 [65]. Both these technologies were employed in the incident beam of these fixed target experiments. The silicon tracker planes were used in SELEX, and were double-sided $300\ \mu\text{m}$ thick detectors with $50\ \mu\text{m}$ strip pitch. These detector planes would provide more than adequate point resolution for CKM. In this design the upstream spectrometer would be realized by two sets of silicon detector planes on either side of a Fermilab beamline dipole magnet as shown in figure 10. The silicon planes will be configured as two slightly ($200\ \mu\text{m}$) overlapping panels providing an instrumented beam area of ($8\text{ cm} \times 10\text{ cm}$).

The $\sim 16\text{ K}$ silicon strips of the four stations would be readout at the edges of each detector plane with a modified versions of the SVX-3 readout chip being developed for CDF. Required modifications to the SVX readout chip and other technical issues associated with this readout system are described in section 6.2. The expected integrated radiation dose is low enough that both

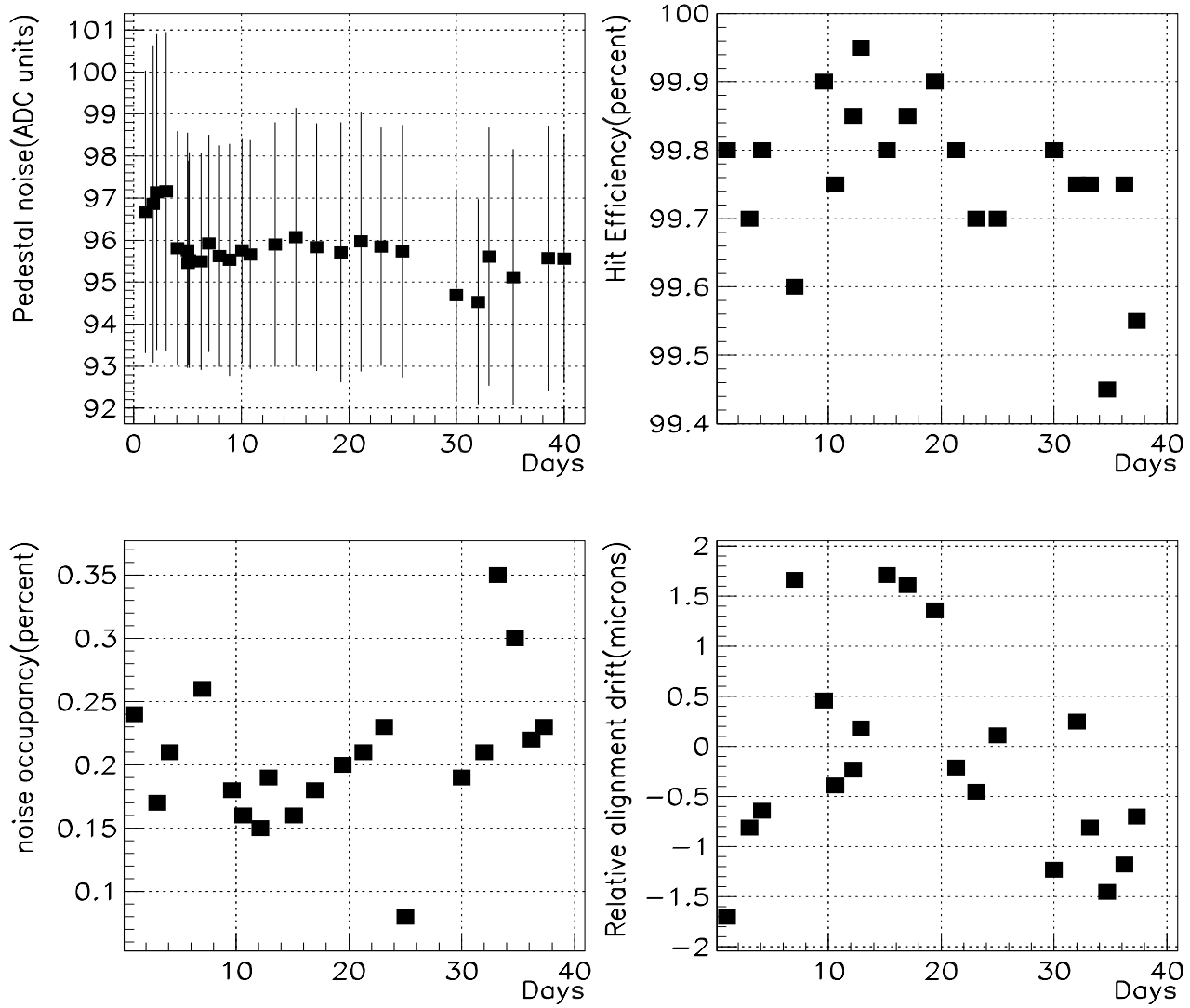


Figure 11: Track averaged performance of a typical silicon plane in the SELEX beam tracking system over a 40-day period. The upper left figure plots the pedestal width as a function of time. The upper right figure plots the single track efficiency, and the lower left figure plots the noise readout occupancy for the nominal strip readout threshold. The lower right figure demonstrates the alignment stability over the 40 day period.

	Cell Size	Average Rate	Cell Deadtime	Average Cell Occupancy	Total ΣX_0	Total $\Sigma \lambda_T(K^+)$
Silicon(x,y)	50 μm	60 kHz	132 nsec	0.6%	$4 \times 0.32\%$	$4 \times 0.07\%$
Mini-Drift(x,y,u,v)	1 mm	1.2 MHz	25 nsec	3.0%	$4 \times 0.40\%$	$4 \times 0.09\%$
Straws(x,y,u,v)	5 mm	6.0 MHz	25 nsec	15.0%	$4 \times 0.32\%$	$4 \times 0.16\%$
Fibers(x,y) [†]	500 μm	600 kHz	25 nsec	1.6%	$4 \times 0.71\%$	$4 \times 0.37\%$

[†] Including a 50% overhead for carbon composite structure.

Table 6: Rates, occupancies and integrated material for several candidate upstream tracking technologies. Maximum cell occupancies are scaled to an incident beam rate of 51 MHz spread evenly over a 5 cm diameter beam region. The 51 MHz rate is the sum of 30 MHz K^+ , 15 MHz π^+ , and 6 MHz of upstream decays and interactions.

the silicon detectors and readout electronics can be fabricated with “rad-soft” CMOS technology. In the SELEX experiment the rad-soft beam silicon was exposed to 1 MHz/cm² (~ 1 Mrad) of charged particles with no observable damage. In CKM the rate per cm² will be 50 MHz / 50 cm², which is comparable to the SELEX exposure.

The silicon readout is deadtimeless in 132 nsec time slices, where two contiguous slices are read out for each strip over threshold. The SELEX silicon beam tracking system read out 0.2% of the channels due to noise hits above threshold. This readout threshold typically delivered single track efficiency of 99.8%. The performance of a typical plane of beam silicon in the 47K channel SELEX system is shown in figure 11. In CKM a typical event will have ~ 30 hit silicon strips due to noise, and about *ten* silicon tracks per event (due to the sum of two 132 nsec time slices) leading to an additional 80 hits. Despite the fact that there are ten silicon tracks in each event, the individual track reconstruction efficiency will be high since the tracks are essentially parallel and suffer little scattering.

The “Beam Time Stamp” (BTS) system upstream of the UMS silicon planes is a $\{x, x', y, y'\}$ fiber tracking plane with a relatively high (D0-type, 12 p.e./mip) photo-electron yield to provide an accurate time stamp (± 1 nsec). for each track in the silicon tracker. A (± 1 nsec) time resolution will allow the upstream spectrometer to reduce the list of candidate upstream tracks to one with high efficiency. In addition, the charge sharing between the two contiguous silicon readout slices will provide some timing redundancy as well. The ~ 600 channels of the BTS system will be readout with VLPC electronics being developed for D0. The VLPC signal is digitized with a the pipeline TDC system (TMC) described in section 6.2. The fiber/VLPC readout scheme is described in greater detail in section 5.8.

The “mini-drift” tracking system employed in Fermilab experiment E690 was composed of two sets of chambers, (6 in \times 4 in) and (15 in \times 8 in) operating at 30 psig and 7 psig respectively. A design to accommodate the 4 in diameter CKM beam would be intermediate between these two chamber sizes. Given the hyperbaric operation of these chambers it is likely that this design could be incorporated into the vacuum beam transport in a straightforward manner. Both size chambers delivered better than 150 μm of resolution, with the small chamber delivering better than 100 μm . Each of the E690 tracking stations had four views with the efficiency of each view better than 99.5%. Operating with a (82% Ar, 15% isobutane, 3% methylal) mixture the maximum drift time of the small chamber was 20 nsec, and 30 nsec for the larger chamber. The 1600 channels of the four planes of each of the four stations would be readout with the pipeline TDC system (TMC) described below. The time resolution of the mini-drift chambers provide a sufficient time stamp (± 1 nsec), so that an upstream

scintillation plane would not be required for this solution.

The optimal design for the upstream spectrometer is still under active development. The two designs outlined above principally serve as an existence proof of the required performance.

5.3 The Kaon RICH

The kaon RICH provides a very high level of K^+ tagging against $\beta=1$ particles (π^+ , μ^+ , e^+) and sub-threshold particles (p^+) that are in the ~ 22 GeV beam. The momentum of tagged K^+ particles must be measured to an accuracy better than $\pm 0.5\%$.

5.3.1 Experience from the SELEX RICH

Fermilab experiment 781 (SELEX) built and operated successfully a phototube based RICH detector [66, 67, 68]. This detector used neon gas at atmospheric pressure as the radiator, a $R = 20$ m mirror, and the photon detection was performed with an array of 2848 1/2" photomultipliers. Performance parameters [68] of special interest are described here. For Hamamatsu R760 photomultipliers, the figure of merit achieved was $N_0 = 162 \text{ cm}^{-1}$. The single hit resolution excluding the contribution of tracking errors is 4.6 mm, with a contribution of 4 mm from the size of the phototubes, and 1.3 mm from optical dispersion $n(\lambda)$ for a $\beta = 1$ particle. The typical π^+ / K^+ separation for a narrow momentum band is shown in figure 12

The single hit resolution is essentially independent of the ring radius, as shown in fig. 13. This result was obtained by fitting a Gaussian to the measured ring radii of proton tracks in narrow (1 GeV/c) momentum bins.

In order to achieve the required kinematic rejection ($\sim 1 \times 10^5$) of the $K^+ \rightarrow \pi^+ \pi^0$ background from the $K^+ \rightarrow \pi^+ \nu \bar{\nu}$ signal when the π^0 is not detected, it is crucial that the ring radius (velocity measurement) resolution function be well understood and Gaussian over many decades. The ring radius resolution function for single tracks in the SELEX prototype 10 m Neon RICH is shown in figure 14. Non-Gaussian tails start to appear at the 1×10^{-3} level on the low side, and only at the 1×10^{-4} level on the high side. The high-side of the resolution function is directly relevant for rejecting $K^+ \rightarrow \pi^+ \pi^0$ decays from the measured kinematics of the π^+ track. The non-Gaussian low side tail is expected to arise from a small contamination of non- $(\beta = 1)$ particles in the beam. The non-Gaussian high side tail is likely to be the result of the coarse time measurement (180 nsec gate) and relatively noisy photomultiplier tubes. The time resolution in CKM will be at least $\times 60$ better, and the noise performance of the photomultiplier tubes will be significantly better. This improved time resolution should drive the measured 1×10^{-4} tail well below the required 1×10^{-5} level.

In all further projections of kaon and pion RICH performance we will assume that we can achieve $N_0 = 150 \text{ cm}^{-1}$, and that the single hit resolution will be 5 mm.

5.3.2 The Kaon RICH

The kaon RICH physically is a 10 m long radiator gas vessel with an internal optical system that images the Cherenkov photons to an array of 549 1/2" photomultiplier tubes that measure the the ring image.

The $L = 10$ m long CF_4 or N_2 radiator has a refractive index of $n = 1.0002765$, which yields on average $N_{\text{det}} = 10$ detected photoelectrons for a 22 GeV K^+ . To reduce the occupancy of a single photomultiplier tube, a focal length $F = 20$ m will be used that magnifies the size of the ring image by $\times 2$ at the photomultiplier focal plane array. The optical path will be folded with one or two flat mirrors so to fit into a vessel of 10 m length. The mirror that first reflects the Cherenkov photons must sit in the beam and will be a minimal mass small flat mirror. The details

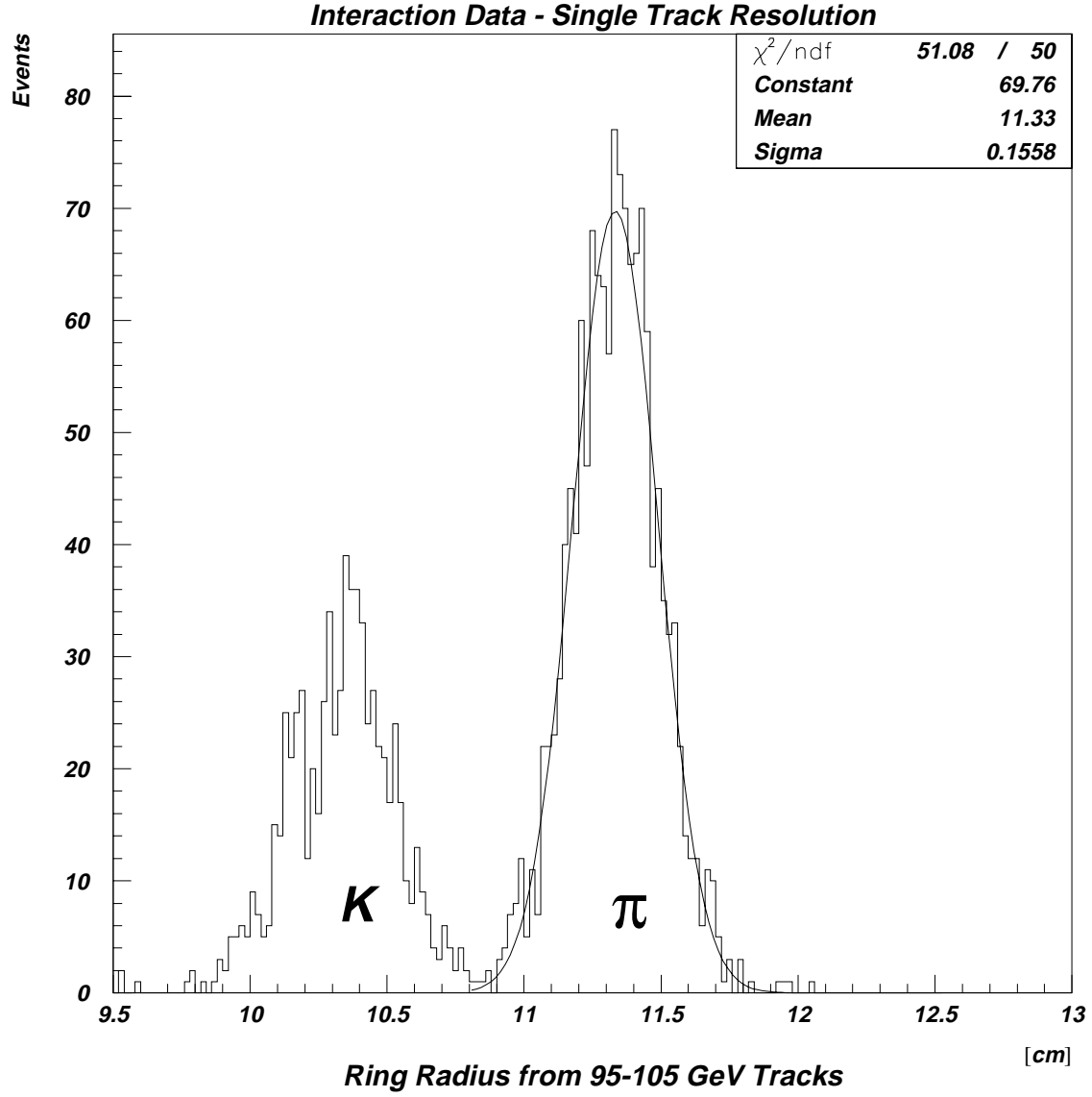


Figure 12: Ring radius distribution in the SELEX RICH for multi track events for tracks with momentum between 95 and 105 GeV/c. We fit a Gaussian to the pion peak of this distribution [68].

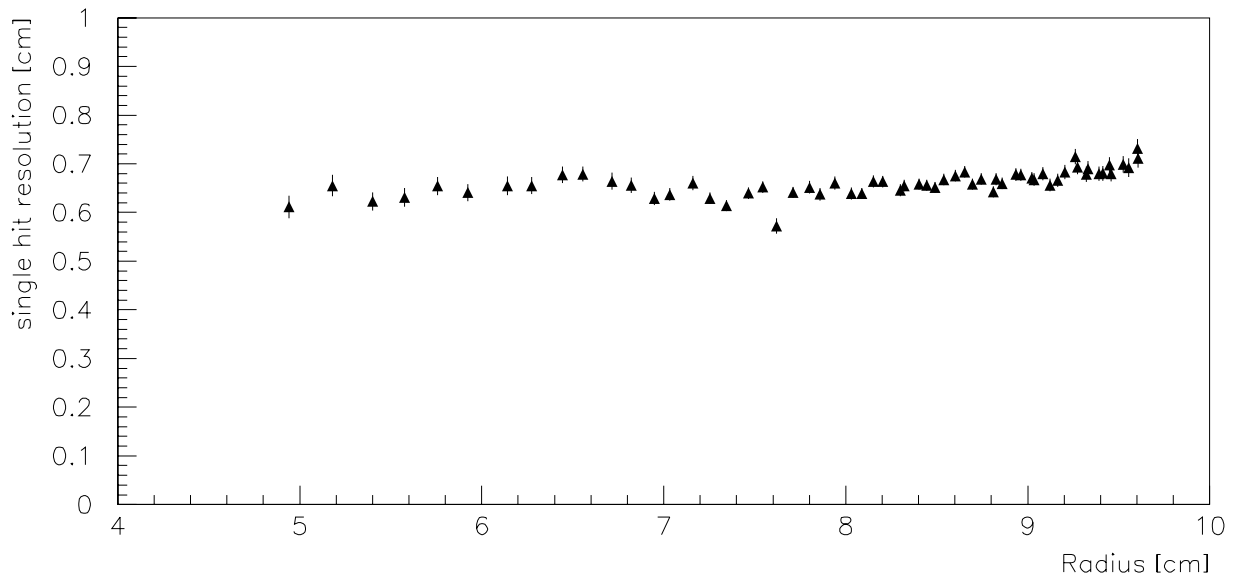


Figure 13: Fitted sigma of the proton ring radius distribution versus the mean radius. These fitted sigmas are larger than the 4.6 mm since they include finite track resolution and hits from overlapping rings.

of the optical path and focal plane array are currently under active study. Figure 15 shows a candidate arrangement photomultipliers at the focal plane array. The system defined here provides a K^+ momentum resolution of 0.5% as shown in figure 4, which illustrates the Cherenkov threshold curve for this design.

Figure 16 illustrates a candidate optical path inside the kaon RICH. Also plotted in figure 15 is the distribution of detected photoelectrons for 1000 beam kaons and 1000 beam pions. A beam momentum of $22 \text{ GeV}/c$ ($\pm 1\%$), a beam divergence of $\pm 100 \mu\text{rad}$, $L = 10 \text{ m}$, $F = 20 \text{ m}$, $N_0 = 150 \text{ cm}^{-1}$ and $n = 1.000287$ are assumed. The two rings in fig 15 correspond to the K^+ (inner) and π^+ (outer) respectively. To reduce the number of photomultipliers, we will only instrument part of the π^+ ring region. The arrangement shown corresponds to an average of 10 detected photoelectrons for beam pions. In this proposed arrangement the average rate in the phototubes on the kaon ring (for a 30 MHz kaon beam) will be 1.4 MHz and the maximum rate will be 2.8 MHz. Although these rates are high, the tubes are counting single photo-electrons so this should be tolerable with fast high quality tubes such as the Hamamatsu R760 tube.

5.3.3 Effect of Dispersion on the Resolution Function

Dispersion (dependence of the refractive index on the wavelength of the Cherenkov photon) is a small fraction of the resolution function for the SELEX RICH since the particles considered are high on the threshold curve where the Cherenkov angle is changing slowly. In contrast, CKM operates on the steep region of the threshold curve where the Cherenkov angle is changing rapidly. Dispersion effects are more significant near threshold, since the fractional contribution to the resolution function is inversely proportional to the Cherenkov angle. To minimize this effect we have been considering [69, 70, 71] only low dispersion radiator gases such as helium, neon, Freon-14 (CF_4), and nitrogen. The

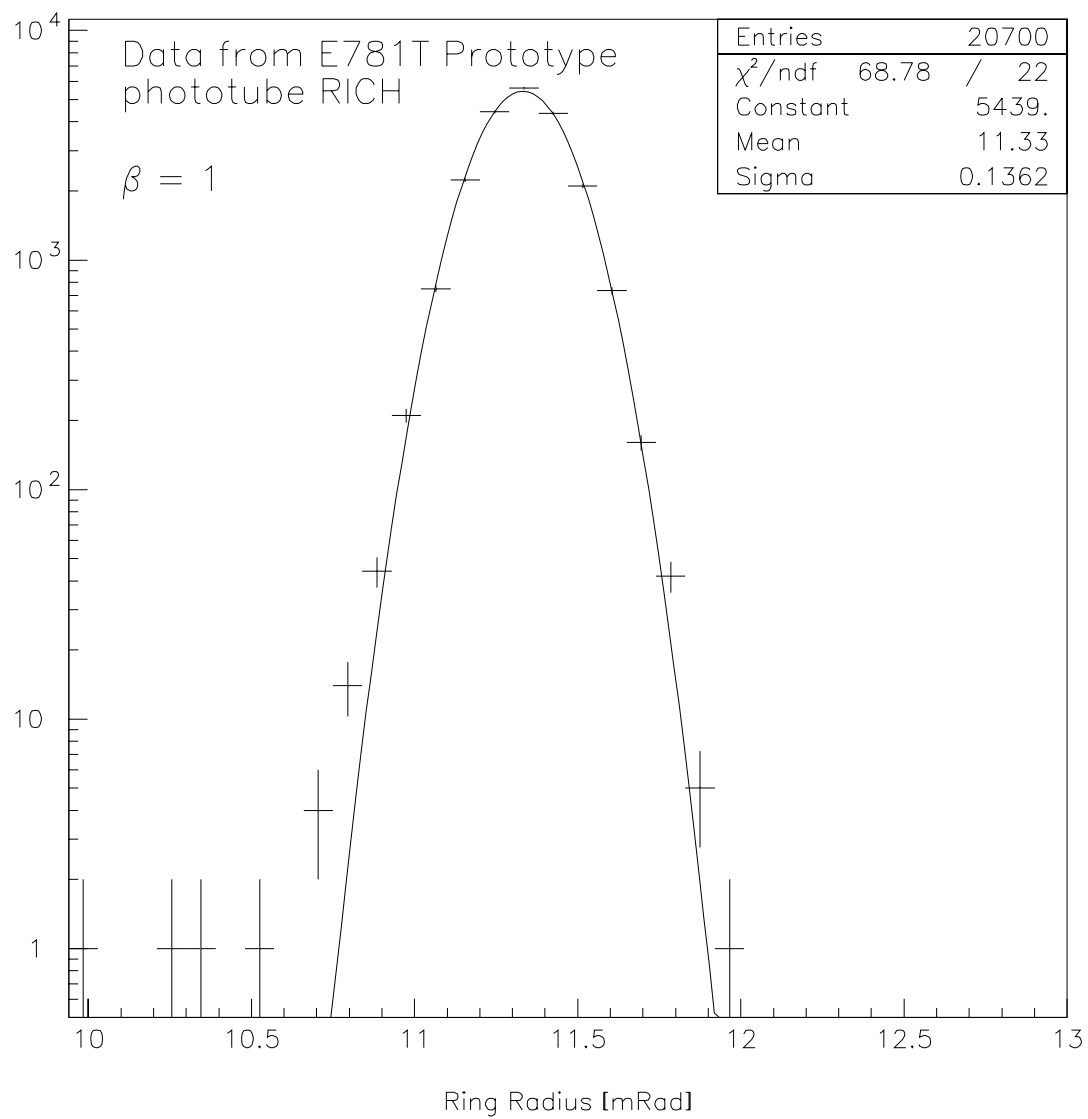


Figure 14: Measured ring radius distribution from the SELEX prototype RICH.

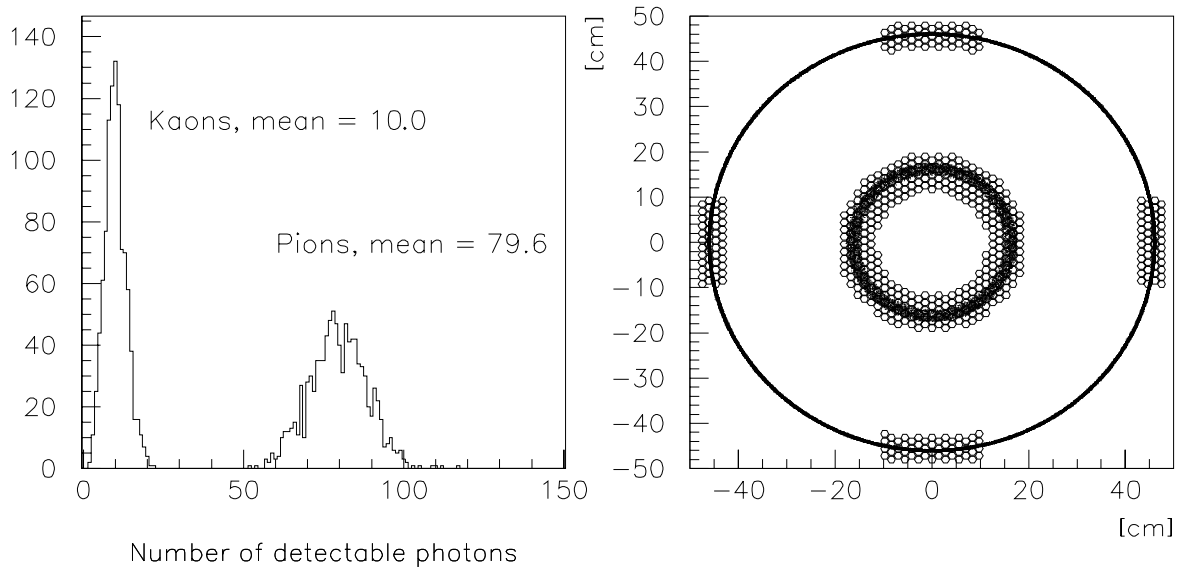


Figure 15: left: Number of detectable photons. right: Distribution of detected photons in the kaon RICH focal plane for 1000 beam K^+ and 1000 beam π^+ events Overlaid is a proposed arrangement of the photomultipliers; 549 photomultipliers are plotted.

optimal radiator gas is actively under study, and will likely be one of these four gases.

Since dispersion is more pronounced at shorter wavelength, it is in principle possible to reduce its influence by using an appropriate window which is nontransparent below a certain wavelength. To study this, we folded the Cherenkov spectrum (equation 14), the dependence of the refractive index on the wavelength (from [69, 70, 71]), and the Hamamatsu R760 photodetection efficiency [72] (cutoff at 160 nm) to obtain the contribution of the dispersion; to simulate the cutoff at low wavelength, the efficiency was set to 0. The obtained error was then added in quadrature to the geometrical resolution obtained from the SELEX rich, with the assumption that we will detect an average of 10 photons. The result of this study is shown in figure 17. For all gases we can reach the required 0.5 % momentum resolution. The reduction in dispersion has to be offset by a higher refractive index, which means more gas and hence more multiple scattering, to obtain the same number of detected photon (since with the filter we lose photons). The results are summarized in table 7.

5.3.4 Kaon RICH readout system

The photomultiplier tubes (PMTs) that instrument the kaon RICH focal plane must have excellent timing and noise characteristics. PMT tubes under consideration now (Hamamatsu 1/2" R760) have timing resolutions better than ± 1 nsec, and deadtimes less than 25 nsec. PMTs are intrinsically very low noise devices, and extrapolating from the SELEX experience the CKM RICH systems should have noises rates of less than 500 Hz/tube. One serious engineering consideration that remains to be addressed is the vulnerability of the PMTs to helium gas and to a lesser extent neon gas. A

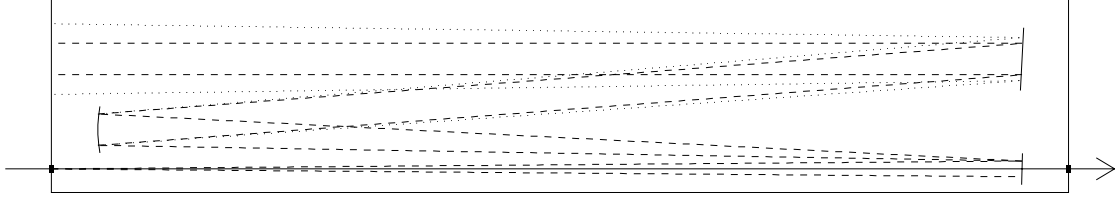


Figure 16: Possible schematic of the kaon RICH optical path. The vessel drawn has a total length of 11 m. The long arrow represents the beam; the thicker dots are the beam windows. The dashed line represents Cherenkov photons generated by a K^+ , dotted line Cherenkov photons from a π^+ . The flat mirror in the beam will only reflect part of the Cherenkov photons from the pions.

Gas	Rad Length [g/cm ²]	minimum			at 0.5 %	
		resolution	pressure	Rad Length	pressure	Rad Length
N_2	32.99	0.34 %	1.25 atm	4.7 %	1.11 atm	4.2 %
Ne	28.94	0.28 %	5.60 atm	17.0 %	4.70 atm	15.0 %
He	94.32	0.26 %	10.1 atm	1.9 %	8.94 atm	1.7 %
CF_4	33.	0.30 %	0.77 atm	9.2 %	0.66 atm	7.90 %

Table 7: Some properties of radiator gases considered for the Kaon RICH.

helium based system requires a significant engineering effort to ensure that the helium radiator gas is isolated from the PMT array. The 549 PMTs are readout with the pipeline TDC (TMC) system described in section 6.2.

5.4 The Kaon Entrance Angle Tracker System

The integrated material of the kaon RICH significantly alters the incident angle of the kaon entering the vacuum decay volume through both Coulomb and nuclear scattering. The Kaon Entrance Angle Tracker System (KEATS) shown in figure 10 is a minimal-mass tracking system at the upstream end of the vacuum decay volume that measures the entrance kaon angle to an accuracy of $\sim 40 \mu\text{rad}$. Candidate tracking technologies and attendant readout systems are the same as those described for the upstream spectrometer: Double-sided Silicon or Hyperbaric Mini-Drift systems.

5.5 The Beam Interaction Veto System

Despite the minimal material of the KEAT system, elastic and inelastic interactions in the KEAT mass can be a source of background particles as well as corrupt the incident kaon momentum. The role of the Beam Interaction Veto (BIVS) illustrated in figure 10 is to veto particles associated with inelastic scattering of beam particles in the material upstream. The inner layer of the BIVS must be very efficient for electrons, muons, pions, and protons that arrive within a 5 nsec timing gate. Detection of charge particles is realized with a hermetic layer of 1 cm of scintillator as the innermost

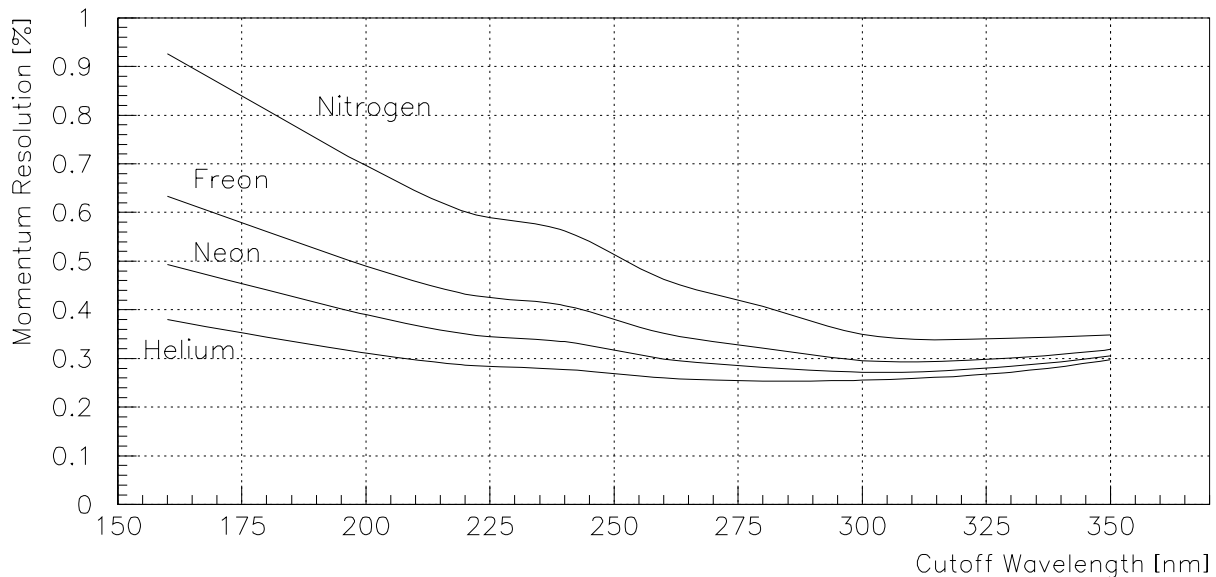


Figure 17: The momentum resolution of the Kaon RICH as a function of the lowest detected wavelength for different gases.

BIVS layer.

Studies by Inagaki et al. [42] show that detection inefficiencies of less than 1×10^{-5} can be achieved with 1 cm of plastic scintillator for minimum ionizing (1 GeV) charged particles. The inefficiency for low energy electrons (2 MeV) will not be as good as this due to inevitable energy loss mechanisms, and in our background simulations we conservatively set the inefficiency to be 100% in 0 – 2 MeV, 10% 2 – 20 MeV, 1% 20 – 40 MeV, and the profile listed in table 4 for energies above 40 MeV. For muons, pions and protons that arrive within the 5 nsec time gate, we assume an inefficiency of 1%. The BIVS must also detect neutral hadrons such as K^0 , neutrons, and hyperons with moderate efficiency.

The BIVS Photon veto efficiency as a function of energy needs to be as good as the vacuum veto system performance listed in table 4. The detector system is as close to the beam (~ 10 cm radius) as the halo allows, and is 5 m in length, and resides within the vacuum decay volume. The BIVS photon veto modules are essentially equivalent to the Pb/Scintillator modules of the vacuum photon veto systems described below. The PMTs that read out the charged and photon-veto BIVS scintillator have the time and deposited energy digitized with the pipeline TDC (TMC) and CMS QIE readout systems described in section 6.2.

5.6 The Vacuum Decay Vessel

The vacuum decay vessel is 45 m long increasing from an upstream outer diameter of 100 cm to an outer downstream diameter of 140 cm. The upstream and downstream windows are composed of a mylar-kevlar sandwich similar to the KTeV vacuum windows. The inner walls of the vacuum decay volume are tiled with photon veto system modules illustrated in figure 10. The vacuum system must maintain a pressure of less than 1×10^{-6} torr in the presence of a significant outgassing load of the scintillator that composes the photon veto and BIV systems.

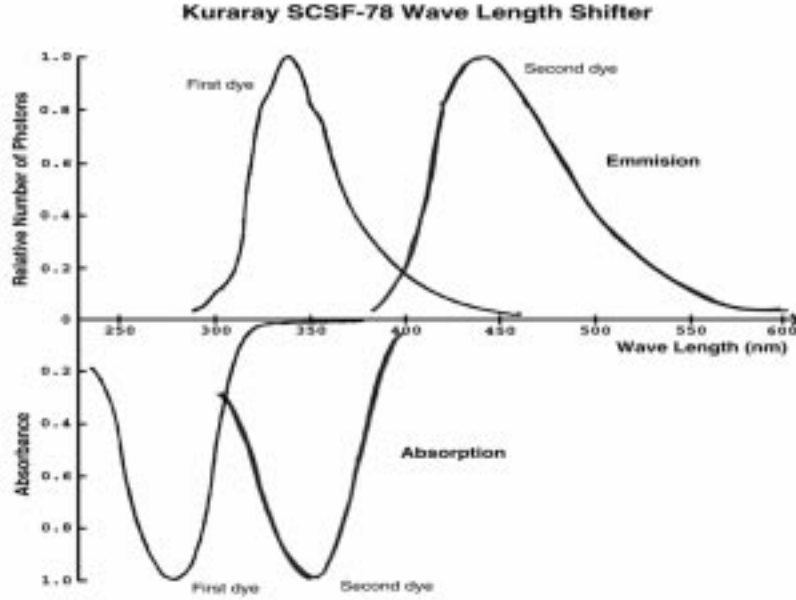


Figure 18: The absorption and emission spectra of the two dyes proposed for the KAMI/CKM photon veto detectors. The first dye will be used in the scintillator and the second dye will be used as a wavelength shifter in the fibers. Reproduced from [41].

5.7 The Vacuum Veto System

The vacuum veto system shown in figure 10 is a fine sampling calorimeter consisting of 1 mm thick lead sheets and 5 mm thick plastic scintillator. The veto system has an orthogonal depth $12X_0$ radiation lengths (40 cm). All of the materials are located on the inside wall of the vacuum tank to avoid any dead material at the boundary of the tank and the veto detector. As with the BIVS, the VVS must be very efficient for charged particles. This is realized with a hermetic layer of 1 cm scintillator as the innermost VVS layer. In our background studies we assume the same charged particle inefficiency profile for the VVS as the BIVS discussed previously.

Wave length shifting fibers are inserted in the scintillator stacks to efficiently collect photons and to transport them to photomultipliers which are to be mounted outside of the vacuum tank for easy access. We are investigating the possibility of using the two wave length shifting dyes which are used in Kuraray SCSF78 scintillator. The absorption and emission spectrum of two dyes are shown in figure 18. We plan to use the first dye in the scintillator plates, and the second dye in the scintillator fibers.

We are now investigating the optimal segmentation scheme and are currently assuming a model of 8 azimuthal sectors in 20 cm intervals in the z direction. The fibers from each sector will be bundled to a 2" photomultiplier tube, summing to 1440 channels for the entire system. In and near the spectrometer magnet, fine mesh photomultipliers must be used.

The lead sheets in the vacuum veto modules will be tilted by 45 degrees relative to the beam direction (z -axis) in the fiducial decay region to provide the best sampling ratio for 45 degree incident photons and to avoid any cracks for angles of incidence up to 90 degrees. Table 8 shows the sampling ratio and total depth as a function of the opening angle of photons.

GEANT simulations of a possible photon veto design show that with 1 mm lead sheets and 5 mm

Photon opening angle (degree)	Sampling frequency (mm)	Total depth (X_0)	Total depth (λ_0)
0	1.41	(Infinite)	(Infinite)
5	1.31	138	4.3
10	1.22	69	2.3
15	1.15	46	1.5
20	1.10	35	1.2
30	1.04	24	0.8
45	1.00	16.9	0.56
60	1.04	13.8	0.46
75	1.15	12.4	0.41
90	1.41	12.0	0.40

Table 8: Sampling ratio and total depth (in radiation lengths and nuclear interaction lengths) of vacuum veto counters for various angle of incidence photons. Reproduced from [41].

thick scintillator tiles, better than 80% detection efficiency for very low energy photons with energies between 2 – 20 MeV can be achieved. The results of this GEANT simulation are summarized in figure 19.

A benchmark of achievable inefficiency at higher energies is Brookhaven experiment E-787 which directly measured their veto inefficiency $K^+ \rightarrow \pi^+\pi^0$ decays. The results of this measurement is shown in figure 20 together with a simulation of the sampling and photo-nuclear components. The design of the E-787 veto system is summarized below in table 9.

For high energy photons (above 1 GeV), the inefficiency of the vacuum vetos must be smaller than 3×10^{-5} to reduce the number of $K^+ \rightarrow \pi^+\pi^0$ and $K^+ \rightarrow \mu^+\nu_\mu\gamma$ background events to a tolerable level. As mentioned previously, a small fraction of photons will undergo a photonuclear interaction and produce only neutrons. As shown in table 8, the proposed vacuum veto detector has multiple nuclear interaction lengths for shallow-angle, high-energy photons. This should allow detection of secondary neutrons and minimize the inefficiency which results from photonuclear interactions.

A crucial measurement of the photonuclear cross section to multi-neutrons is ongoing (April 1998) at the INS Electron Synchrotron at Tokyo University in Japan. This test-beam effort is a collaboration of the Fermilab (KAMI), KEK, and BNL groups who propose to measure $K_L \rightarrow \pi^0\nu\bar{\nu}$. A variety of candidate photon-veto detector modules will be studied, including the lead-scintillator sampling configuration described in this proposal. The observation of the multi-neutron cross section is only indicative of the total photonuclear loss, since the cross section into exclusively slow charged fragments that stop in the lead is unobservable. It is likely that this “stealth” component of the cross section will not be significantly larger than the cross section that includes at least one neutron. This stealth component will be studied by comparing the inefficiency of lead-scintillator modules with completely active scintillating (CsI) modules after accounting for shower fluctuation differences that can be reliably calculated. The results of this measurement will have direct bearing of the viability of the required photon-veto detection efficiencies for both $K_L \rightarrow \pi^0\nu\bar{\nu}$ and $K^+ \rightarrow \pi^+\nu\bar{\nu}$ measurements.

In table 9, the vacuum veto counters are compared to the photon veto detectors for KTeV and BNL-E787. The KAMI/CKM design is based on the same WLS fiber readout scheme as KTeV, but has the same fine sampling ratio as BNL-E787.

Currently, inexpensive scintillator is under investigation by the MINOS Collaboration. By ex-

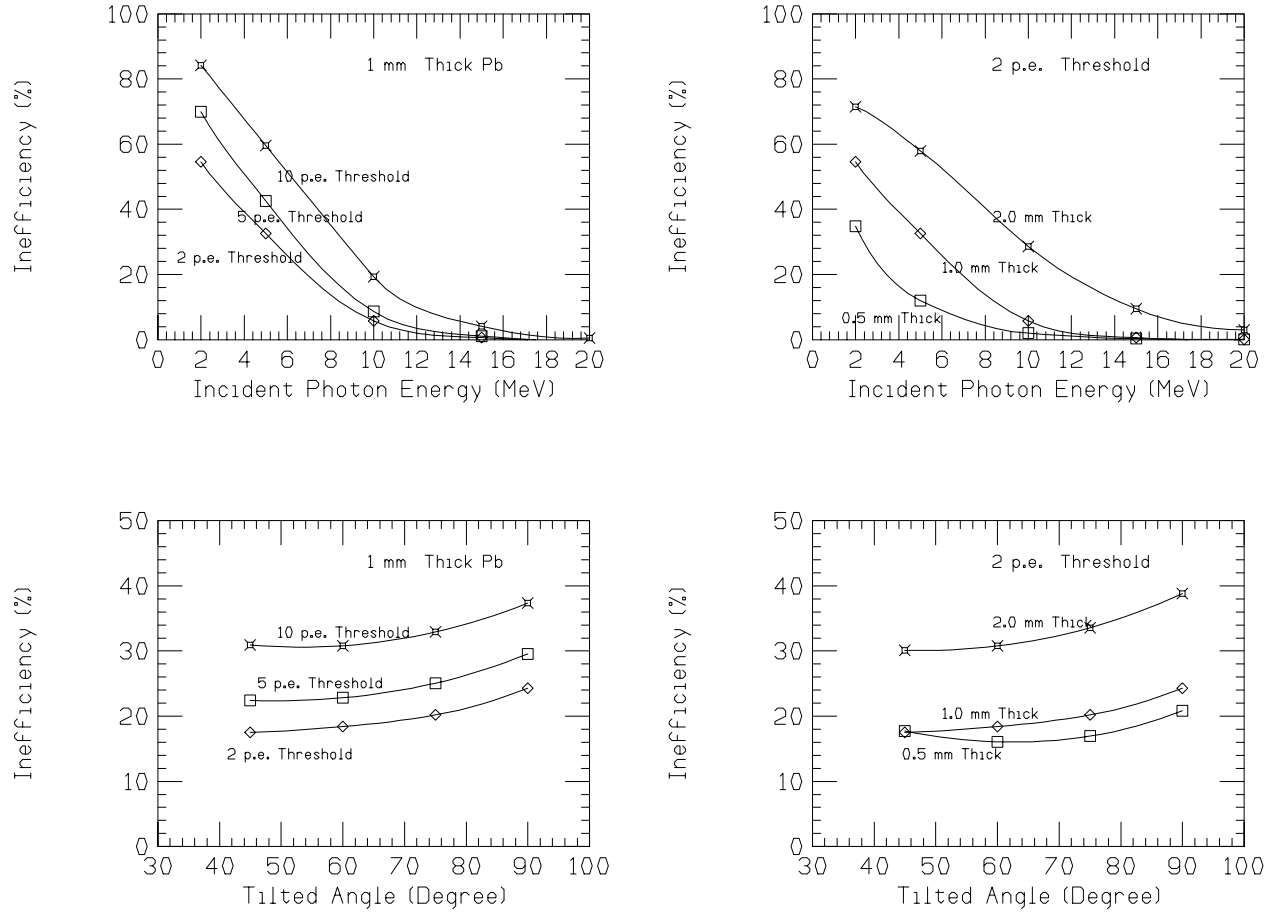


Figure 19: GEANT results of the photon detection inefficiency of the vacuum veto counters. The top two plots show the inefficiency as a function of photon energy, for various photo electron thresholds and lead sheet thicknesses. The bottom two plots show the average inefficiency for photons below 20 MeV as a function of the lead sheet tilt angle. Reproduced from [41].

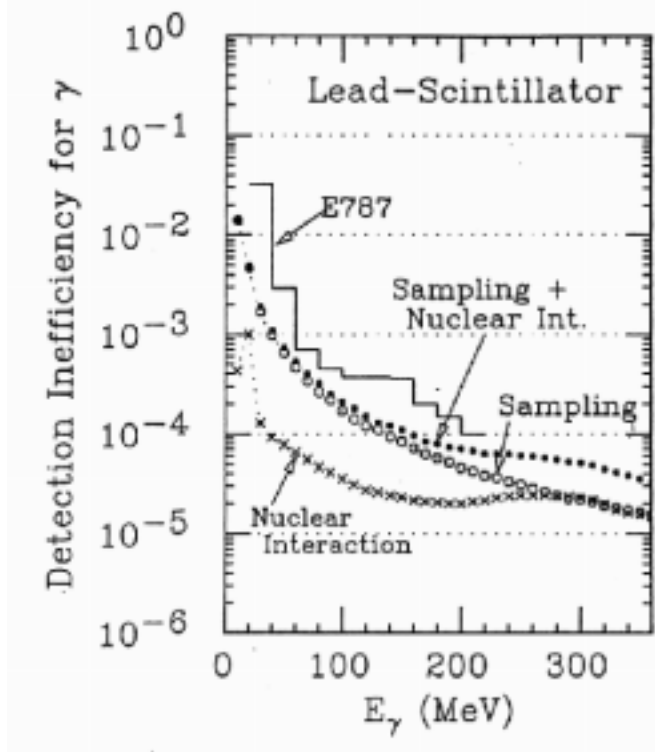


Figure 20: Measured photon detection inefficiency as a function of energy in lead-scintillator detectors from Ref. [42].

truding polystyrene, the cost can be reduced by an order of magnitude compared to the conventional commercial product. D0 has already made such extruded scintillator for their pre-shower detector. Table 10 summarizes the scintillator types and performance for D0, MINOS and KAMI. Another possibility is to use injection molded scintillator. The PHENIX collaboration at BNL has developed scintillating tile for their SHASLIK Calorimeter using this technology. KEK's $K_L \rightarrow \pi^0 \nu \bar{\nu}$ group is also developing such scintillator for a similar veto system. A schematic of a typical scintillator is shown in Fig 21.

5.8 The Downstream Magnetic Spectrometer

The Downstream Magnetic Spectrometer (DMS) is composed of a moderate field dipole (6 kG) 200 MeV p_T -kick analysis magnet bracketed by four tracking stations within the decay vacuum volume. As motivated in section 3.4.1 the tracking stations require an active circular area of 80 cm in diameter, and must provide a resolution of at least $150 \mu\text{m}/\text{hit}$. Peak rates in the beam region are similar to the upstream spectrometer, and vastly dominate the total rate. The rates, occupancies, and integrated material of candidate tracking technologies are listed below in table 11. The beam-region rates (6 MHz/wire) exceed the rate capability of straw drift tubes and hence any straw based solution can't instrument the beam region. The peak rate requirements outside the beam region are relatively modest (120 kHz/wire), and straw drift tubes can reasonably be employed there. Brookhaven experiment E871 has successfully [73] operated a large straw-based tracking system with rates per wire up to 750 kHz that delivers $160 \mu\text{m}$ of resolution per straw.

Although it is likely that a fiber based solution could tolerate the rate with the hole instrumented, the amount of material is too great to reliably achieve a momentum resolution of $\sim 1\%$ due to

	KTeV	BNL-E787	KAMI/CKM
Lead sheet thickness	2.8 mm	1 mm	1 mm
Scintillator thickness	2.5 mm	5 mm	5 mm
Total Depth	16 X_0	14.3 X_0	$> 12 X_0$
Number of Layers	24-32	75	> 45
Light Guide	WLS fiber (1 mm ϕ single clad 3 cm spacing)	Clear light pipe	WLS fiber (1 mm ϕ double clad 1 – 2 cm spacing)
No. of p.e. /MIP/layer	2.4 pe	10 pe	10 pe
No. of p.e. /MIP	60 pe	750 pe	> 1000 pe
No. of p.e. /MeV	0.3 pe/MeV	5 pe/MeV	5 pe/MeV

Table 9: Comparison of the KAMI/CKM vacuum veto counters with photon veto counters from KTeV and BNL-E787. Reproduced from [41]

	D0	MINOS	KAMI/CKM
Cross section	Triangle 5 mm \times 9 mm	Rectangular 1 cm \times 2 cm	Rectangular 2 cm \times 5 mm
Length	2.8 m	8 m	2 m
WLS fiber	0.84 mm ϕ	1 mm ϕ	1 mm ϕ
Type of WLS	3HF	BCF91	SCSF78
Emission lambda	550 nm	520 nm	450 nm
Photo detector	VLPC (QE=60%)	PMT (QE=12%)	PMT (QE=25%)
No. of p.e. /MIP/layer	15 p.e.	8 p.e. (at 2m)	10 p.e. exp'd

Table 10: Comparison of scintillator used by D0, MINOS and KAMI/CKM, reproduced from [41].

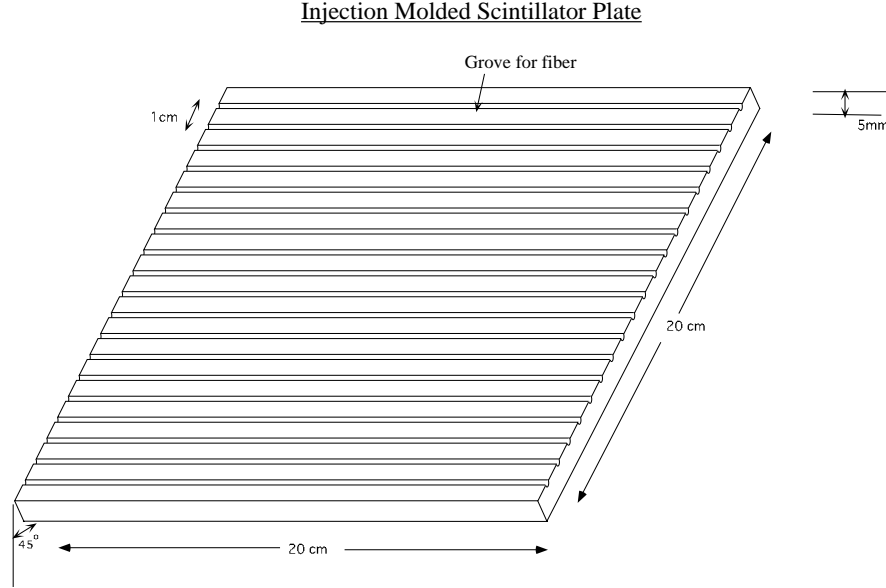


Figure 21: Schematic of a typical injection molded scintillator plate. Reproduced from [41].

multiple scattering. We have studied the resolution achievable with a system based on thin $500\text{ }\mu\text{m}$ fibers and have concluded that multiple scattering alone contributes $> 1\%$ to the resolution for the relevant momenta. In contrast, the relatively low mass of a straw based system affords more planes/station for added redundancy, and has a resolution figure that is dominated by measurement error (assuming $150\text{ }\mu\text{m}$) rather than scattering. The momentum and angular resolution of a straw-based DMS is shown in figure 23. The momentum and angular resolution of the pion RICH is shown as well in figure 23 for comparison.

Therefore, in order to achieve the best possible momentum resolution while minimizing the spectrometer material our default design for the DMS is a straw drift tube based system with the hole region uninstrumented. Exactly how we deal with the hole region is a design issue that is being actively discussed, but the beam region will either be traversed by straws with deadened wires, or the straw plane-pattern per station will be designed with a hole in the center. In either case the default system has four views ($\{x, y, u, v\}$) for the three downstream tracking stations for redundancy and improved space-point resolution. The first tracking station will have $2\frac{1}{2}$ views (5 straw planes, $\{x, y, \frac{1}{2}u\}$) in order to minimize material in this scattering-critical plane.

Each view in a station is composed of two staggered (x, x') planes, leading to eight straw planes per downstream station, and 29 straw planes for the entire system. This system then is composed of ~ 8000 straws, where each straw is instrumented with a preamplifier and TMC TDC channel.

In order to maintain some level of tracking in the beam region, our default design includes a fiber plane outside the vacuum volume immediately downstream of the vacuum window. It is conceivable that this fiber plane could serve as the sole fourth tracking station, and that option is currently under study. This fiber plane is composed of ~ 4000 fibers in an $\{x, x', y, y'\}$ geometry that spans the 80 cm diameter clear aperture of the vacuum window. This tracking plane will be used to ensure that the incident K^+ tracked in the KEAT system actually decayed by requiring that the KEAT

vector doesn't track to a beam-region hit in the DMS fiber plane. The fiber plane will also be useful in fighting backgrounds that include a track in the downstream beam region that would be missed by the straw planes and possibly the pion RICH.

Our choice of fiber readout technology for this downstream plane is motivated by the development work of the D0 collaboration and others at Fermilab who are shaping high speed fiber tracking into a mature technology. The D0 fiber tracker consists of 2.5 m long, $835\text{ }\mu\text{m}$ diameter scintillating fibers spliced to more than 5 m long, $835\text{ }\mu\text{m}$ diameter clear fibers [74]. The light emerging from the clear fibers is viewed by Visible Light Photon Counters (VLPC) detectors. Noise levels of VLPC detectors are less than one photoelectron, enabling low-occupancy readout thresholds of 1.0-1.5 photoelectrons. The D0 prototype detector produces 9 p.e. per MIP with the expectation of 12 p.e. per MIP with their final detector, which would provide a high ($> 99.9\%$) single track efficiency. The fluorescence decay time of the D0 fibers is 7 nsec, which leads to a deadtime of less than 25 nsec per fiber. The time resolution of the fiber-VLPC system has been measured [74] to be better than ± 1 nsec.

The detection efficiency of the D0 prototype device in the presence of a very high 40 MHz background rate has been measured to be better than 98% by D0 [74]. The maximum rate per fiber in CKM is expected to be ~ 600 kHz. A position resolution of $92\text{ }\mu\text{m}$ has been achieved using double layers of fibers. The high quantum efficiency of VLPC detectors ($> 60\%$) make them particularly attractive, although they must operate at liquid Helium temperature to achieve the above mentioned noise levels.

	Cell Size	Beam Region Cell Rate	Cell Deadtime	Max Beam Cell Occupancy	Total ΣX_0	Total $\Sigma \lambda_T(K^+)$
Straws (x,y,u,v)	5 mm	6.0 MHz	25 nsec	15.0%	$4 \times 0.32\%$	$4 \times 0.16\%$
Fibers [†] (x,y)	$500\text{ }\mu\text{m}$	600 kHz	25 nsec	1.6%	$4 \times 0.71\%$	$4 \times 0.37\%$

[†] Including a 50% overhead for carbon composite structure.

Table 11: Rates, occupancies and integrated material for fiber and straw tracking technologies. Maximum cell occupancies are scaled to an incident beam rate of 53 MHz spread evenly over a 5 cm diameter beam region. The 53 MHz rate is the sum of 24 MHz K^+ , 15 MHz of beam π^+ , 6 MHz of K^+ decay pions and muons, and 8 MHz of upstream decays and interactions.

5.9 The Pion RICH

The pion RICH provides a very high level of π^+ tagging against sub-threshold K^+ and p^+ , and ($\beta \sim 1$) e^+ and μ^+ particles from decays and the beam. The relationship between ring radius and π^+ track momentum is shown in figure 22, with the accepted momentum band indicated as a shaded band. The momentum and track angle resolution as determined from the fitted ring radius and ring center is shown in figure 23. The momentum resolution is better than 2.0% over the full accepted π^+ momentum band. For comparison the momentum and track angle resolution of the Downstream Magnetic Spectrometer is shown as well in figure 23.

The pion RICH physically is a relatively large diameter (2 m) 20 m long vessel of neon operating at atmospheric pressure. Maintaining acceptance for decay particles requires that the pion RICH apertures be sealed with relatively large thin windows which practically limits the operating pressure to the ambient atmospheric level. As discussed previously neon is a low dispersion gas, and is additionally motivated by the high performance achieved with the large SELEX RICH. The 20

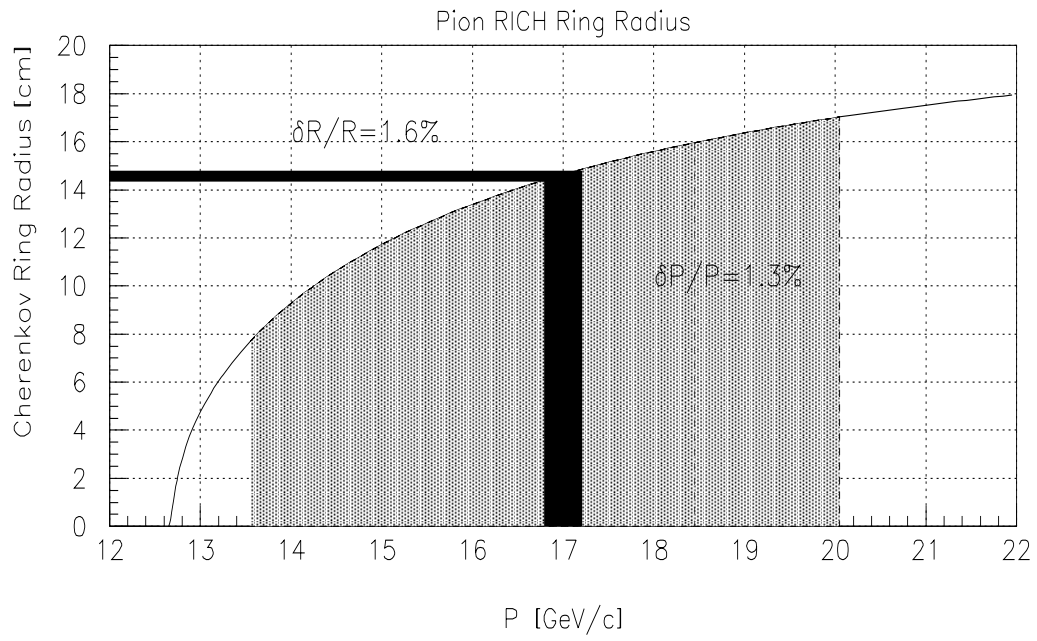


Figure 22: The functional relationship between the ring radius and the π^+ track momentum. The shaded band is the accepted momentum range. The black stripe is a $1\text{-}\sigma$ band that illustrates the momentum-radius transfer function.

meters of neon radiator gas present about 6% and 2% of radiation and interaction lengths to the beam and traversing decay particles.

In contrast to the kaon RICH, the relatively large mirrors in the pion RICH optical system preclude the use of the flat thin mirror scheme outlined in the proceeding kaon RICH section. The downstream end of the pion RICH is fitted with a matrix of spherical mirrors mounted on a low mass rigid carbon-fiber lattice structure. The mirrors and mounting system present an additional 7.0% and 2.0% radiation and interaction lengths to the beam and traversing decay particles. The spherical mirrors image the ultraviolet Cherenkov photons to a close-packed array of 3000 1/2" photomultiplier tubes that measure the the ring image. Photomultiplier tubes that would be illuminated by the ($\beta = 1$) beam-particle ring are removed due to rate considerations. Photomultiplier tubes in this beam ring would run at an average rate of 30 MHz, which is far too high for reliable operation. This dead beam ring on average removes 2 hit tubes from decay pion rings. Candidate rings for analysis are required to have at least eight photoelectrons. The rate/tube outside the ($\beta = 1$) ring from all kaon decays is about 20 kHz.

5.9.1 Pion RICH readout system

The photomultiplier tubes (PMTs) that instrument the pion RICH focal plane have excellent timing and noise characteristics. PMT tubes under consideration now (Hamamatsu 1/2" R760) timing resolutions better than ± 1 nsec, and deadtimes less than 25 nsec. PMTs are intrinsically very low noise devices, and extrapolating from the SELEX experience the CKM RICH systems should have noises rates of less than 500 Hz/tube. The 3000 PMTs are readout with the pipeline TDC (TMC) system described in section 6.2.

5.10 The Forward Veto-Calorimeter System

The forward veto/calorimeter system must provide veto efficiencies listed previously in table 4 as well as reasonable electromagnetic calorimetry $\{dE/E \sim (7 - 10)\%/\sqrt{E} + 2\%\}$ for systematic and background studies for $K^+ \rightarrow \pi^+ \nu \bar{\nu}$ and other modes of the CKM physics program. Rate and pion shower effects in the forward region will likely limit the low energy performance of the forward veto system to that listed in table 4. Candidate calorimeter-veto solutions must be extremely hermetic, very fast, and radiation hard. Currently we are considering SPACAL (Pb-Scintillating fiber spaghetti style calorimetry) and SHASHLIK (Pb-Scintillating tile/fiber style calorimetry). Both these technologies have been studied extensively [75] [76], and large scale SPACAL [77] and SHASHLIK [78] have been realized recently in the H1/HERA and PHENIX/RHIC detectors. The application of these two technologies for the CKM Forward Veto-Calorimeter system is discussed below.

5.10.1 The H1/HERA SPACAL Calorimetry

The H1 SPACAL backward-region calorimeter has attractive characteristics for the CKM forward veto-calorimeter system. The characteristics of this calorimeter are summarized below in table 12. The H1 device has a depth of 28 radiation lengths in order to contain high energy showers. This depth would compromise the total CKM π^+/μ^+ separation since this calorimeter is not longitudinally sampled. The required π^+/μ^+ separation is described in the following section. Employing SPACAL for the CKM/FVS would require only $(16X_0)$ to contain showers up to 15 GeV, which will not significantly degrade the longitudinal sampling profile of the experiment. Of equal importance to the integrity of the π^+/μ^+ longitudinal sampling profile is the minimization of dead gaps. The H1 SPACAL calorimeter has a 30 cm dead gap immediately downstream for photomultiplier tube

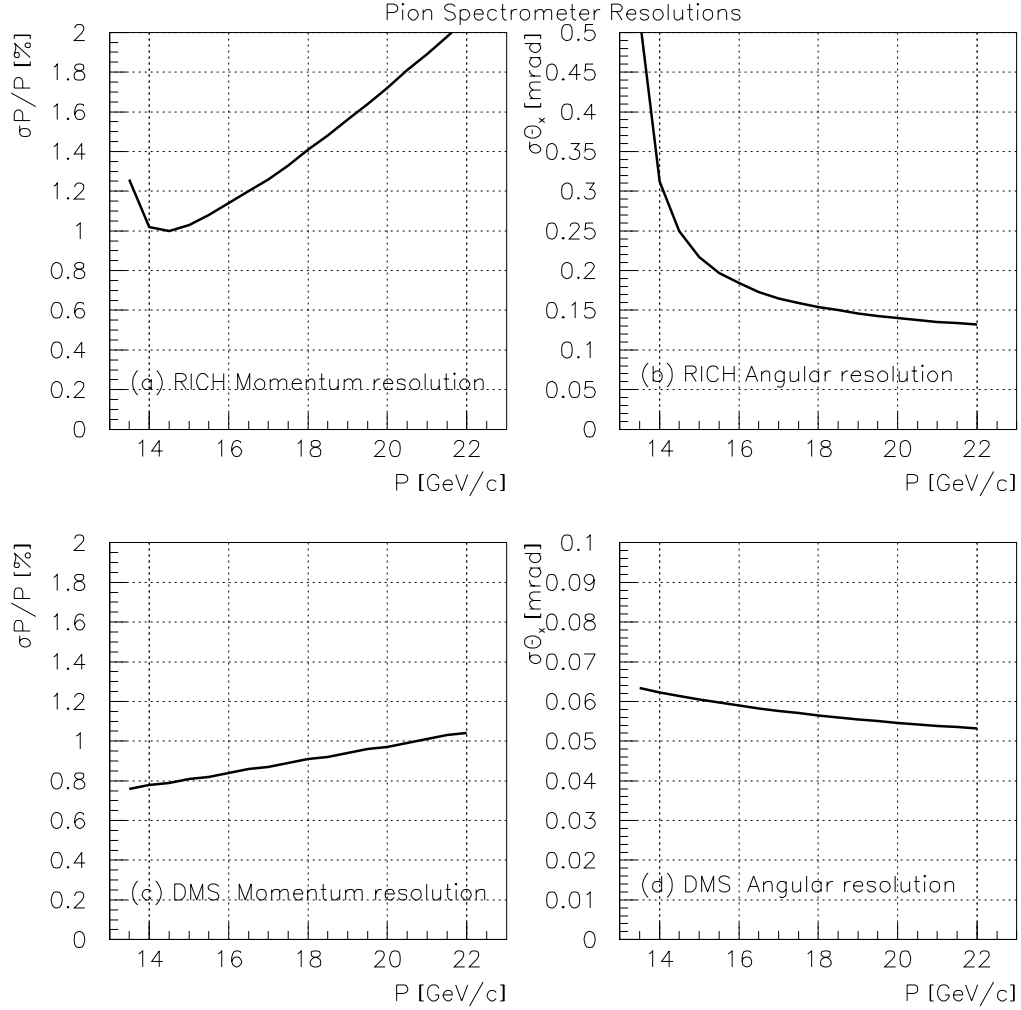


Figure 23: Pion (a) fractional RICH momentum resolution and (b) RICH angular resolution as a function of pion momentum from the pion RICH velocity spectrometer measurements. Contributions to the resolutions from optical dispersion and multiple Coulomb scattering in the Neon radiator gas and phototube size, are included. Downstream magnetic spectrometer (DMS) (c) fraction momentum resolution and (d) angular resolution as a function of pion momentum. Contributions to the resolutions from tracking resolution and multiple Coulomb scattering in the tracker are included.

instrumentation, which is probably acceptable but currently under study. This gap needs to be minimal in CKM in order to maximize the π^+/μ^+ separation capability.

A significant concern with SPACAL calorimetry is the effect of “channeling” where an incident photon aligns with the fiber direction or the lattice geometry of the lead-fiber matrix. Clearly application of this technology in the CKM/FVS would require that the fibers be non-projective, and that the lattice planes be maximally randomized. Lattice-plane randomization is a key design feature of the H1/SPACAL calorimeter and has limited channeling nonuniformity to less than 8%. The effects of channeling on low-energy veto performance is an ongoing topic of study for CKM. The required CKM transverse segmentation is similar to the H1 design, and each $5\text{ cm} \times 5\text{ cm}$ module would be readout with a fast photomultiplier tube. Both the deposited charge and time of each PMT must be readout, which will be implemented with the CMS QIE readout system and the TMC pipeline TDC described in section 6.2.

	H1/SPACAL	CKM/FVS
Outer Diameter.	170 cm	200 cm
Inner Diameter (Beam Hole).	14 cm	16 cm
Transverse Cell Size.	$4.0 \times 4.0\text{ cm}^2$	$5.0 \times 5.0\text{ cm}^2$
Number of Cells.	1192	1242
Longitudinal Depth.	25.0 cm	14.0 cm
Downstream Dead Gap.	30 cm	30 cm
Radiation Length Depth.	$28X_0$	$16X_0$
Interaction Length Depth.	$1.0\lambda_I$	$0.6\lambda_I$
Time Resolution.	0.4 nsec	1 nsec
Channel Deadtime.	25 nsec	25 nsec
Energy Resolution.	$7\%/\sqrt{E} + 1.0\%$	$(7 - 10)\%/\sqrt{E} + 2.0\%$
Position Resolution.	$4.4\text{ mm}/\sqrt{E} + 1.0\text{ mm}$	$5.0\text{ mm}/\sqrt{E} + 1.0\text{ mm}$
Transverse Non-uniformity.	8% max.	5% max.
Fiber Diameter.	0.5 mm	—
Lead/fiber ratio.	2.3 : 1	—
Lead-fiber Density.	7.3 g/cm^3	—
Moliere Radius.	2.55 cm	—

Table 12: Performance Summary of the H1 SPACAL Backward Calorimeter.

5.10.2 The PHENIX SHASHLIK Calorimetry

The SHASHLIK readout scheme extracts the scintillation light from behind a Pb-scintillator stack with an array of wavelength shifting fibers that skewer the stack with a typical density of $\sim 1\text{ fiber/cm}^2$. This architecture has the potential for being extremely hermetic, and is similar in principle to the architecture of the Vacuum Veto System where the scintillator slabs are readout with imbedded wavelength shifting fibers. In contrast to SPACAL technology, one can reasonably consider large super-modules built from continuous sheets of lead with the scintillator planes segmented by narrow grooves cut in the scintillator sheet. A similar segmentation technique is being employed in the CMS HCAL design. For CKM we have discussed a design of four overlapping super-modules in the Forward Veto System, with a transverse segmentation of $5\text{ cm} \times 5\text{ cm}$ cut into the scintillator planes.

The lower SHASHLIK fiber density as compared to SPACAL densities reduces the amount of collected light, and consequently the energy resolution suffers somewhat. Despite this lower light yield, a SHASHLIK prototype calorimeter tested at CERN [76] produced 12 photons/MeV, which corresponds to approximately ~ 50 photo-electrons for the lowest energy (20 MeV) photon that the FVS must detect with a 50% efficiency as listed in table 4. The lower SHASHLIK fiber density also reduces losses and distortions due to channeling effects. Operating at a non-projective angle of 3% the SHASHLIK prototype nonuniformity envelope was $\pm 3\%$ as a function of position and angle. The performance of the SHASHLIK calorimetry employed in the PHENIX detector is listed below in table 13.

	PHENIX/SHASHLIK	CKM/FVS
Outer Diameter.	Large barrel, $48m^2$	200 cm
Inner Diameter (Beam Hole).	—	16 cm
Transverse Cell Size.	$5.25 \times 5.25 \text{ cm}^2$	$5.0 \times 5.0 \text{ cm}^2$
Number of Cells.	15552	1242
Longitudinal Depth.	37.5 cm	14.0 cm
Downstream Dead Gap.	$\sim 20 \text{ cm}$	30 cm
Radiation Length Depth.	$19X_0$	$16X_0$
Interaction Length Depth.	$1.4\lambda_I$	$0.6\lambda_I$
Time Resolution.	0.1 nsec	1 nsec
Channel Deadtime.	25 nsec	25 nsec
Energy Resolution.	$8\%/\sqrt{E} + 1.5\%$	$7\%/\sqrt{E} + 1.0\%$
Position Resolution.	$6 \text{ mm}/\sqrt{E} + 1.5 \text{ mm}$	$5.0 \text{ mm}/\sqrt{E} + 1.0 \text{ mm}$
e/π separation at Transverse Non-uniformity.	3% max .	5% max .
Fiber Diameter.	1.0 mm	—
Lead/Scintillator thickness.	1.5 mm/4 mm	—
Fibers/cell	36	—
Moliere Radius.	3.40 cm	—

Table 13: Performance Summary of the SHASHLIK prototype calorimeter

5.11 The Muon Veto System

As described in section 3.4.6. the Muon Veto System (MVS) must identify muons between 14 GeV and 20 GeV with a muon mis-id rate of of less than 1×10^{-5} while maintaining high acceptance ($A_{MVS} = 95\%$) for the $K^+ \rightarrow \pi^+ \nu \bar{\nu}$ signal.

A plausibility argument for achieving this extraordinary level of mis-id integrity was presented in section 3.4.6 by considering μ -decay, μ -bremsstrahlung, and μ -(Deep Inelastic Scattering) (DIS) processes separately. Preliminary studies of the interplay and topology of these processes with respect to $K^+ \rightarrow \pi^+ \nu \bar{\nu}$ pion showers have been studied with GEANT simulations for a range stack described in table 14.

In order to achieve 1×10^{-5} muon efficiency at 95% pion acceptance it is necessary for the outer radial aperture of the MVS to be 20 cm greater than that of the FVS to allow for multiple scattering in the MVS.

About 15 MHz of incident tracks will range out to a rate of ~ 10 MHz of penetrating muons over the 2.4 m diameter fiducial area. There is a beam hole in the muon system of diameter 14 – 16 cm

Planes penetrated:	< 12	< 11	< 10	< 9	< 8	< 7	< 6
Muon Efficiency ($\times 10^{-5}$):	2.4	1.8	1.5	1.2	1.1	0.9	0.7
Pion Efficiency:	0.93	0.90	0.85	0.79	0.70	0.58	0.44

Table 14: GEANT study of muon efficiency and pion acceptance (10 GeV) for a simple structure of 12 iron slabs, each 8.5 cm thick interleaved with 12 scintillator planes. The simple algorithm employed here is using the penetration depth in the range stack as the only discriminant. (Simulation with an algorithm based on shower length achieves a muon efficiency of less than 1×10^{-5} for a pion acceptance of 95%).

that passes the 50 MHz charged beam. The transverse segmentation of the scintillator in the range stack is determined by the rate of ranging particles, and is currently under study. The counters will be readout with the pipelined TMC TDC system, as well as the CMS HCAL QIE system to digitize the deposited charge.

5.12 The Beam Kicker Veto System

The beam transport downstream of the pion RICH and through the FVS/MVS is inside a 10 meter long atmospheric helium bag which terminates on a $20 \text{ cm} \times 20 \text{ cm}$ Charged Veto Plane (CVP) composed of scintillating fibers. This veto plane is crucial to veto of photons that have converted in the upstream pion RICH material, as well as tagging beam particles. This system must have excellent time resolution ($\pm 1 \text{ nsec}$), and have a charged particle efficiency of at least 99.0%. In order to ensure excellent time resolution and high efficiency, relatively thick and bright D0 fibers ($830 \mu\text{m}$, 12 p.e./mip) will compose the CVP plane. The CVP system is readout with VLPCs instrumented with the pipeline TDC (TMC) described in section 6.2. Immediately downstream of the CVP the beam is kicked by a Fermilab BM-109 magnet (1 GeV p_T -kick) to the charged beam dump 20 meters further downstream. Photons that remain in the upstream beam acceptance are intercepted by the Hole Veto System (HVS) which must provide a photon inefficiency performance listed in table 4.

5.13 The Beam Dump

In order to minimize backslash and the ambient neutron gas level, the charged kaon beam must terminate in a borated reentrant cave 20 meters downstream of the Hole Veto System.

6 The Trigger and Data Acquisition Systems

6.1 The Trigger System

In order to minimize backgrounds from accidental sources, it is critical that both the average *and* instantaneous trigger rates be as low as possible. The average trigger rates will be driven by the required experiment sensitivity, and the instantaneous trigger rate will be minimized by debunching the Main Injector proton beam as described in section 4.2 Assuming the goal [48] of less than 10% beam microstructure can be achieved, then the actual trigger rates will not deviate far from calculated average trigger rates. Of equal importance to time-microstructure is the quality and kaon purity of charged beam. The recent experience [79] of the KTeV beam is very encouraging in that

it demonstrates careful design can deliver a high-rate beam environment where trigger rates are dominated by kaon decays.

The conceptual design of the CKM trigger system is based on the experience of high rate trigger systems employed in the $K_L \rightarrow \mu e$ experiment (E-871) at Brookhaven, the SELEX experiment at Fermilab, and KTeV. The first level trigger (Level-1) is an asynchronous system based on the following relatively simple coincidence and veto condition:

$$\text{Level} - 1 = \text{KRICH}(K^+) * \overline{\text{KRICH}(\pi^+)} * \text{PRICH}(\pi^+) * \overline{\text{VVS}(1 \text{ GeV})} * \overline{\text{MuonVS}}$$

where the trigger elements are defined in table 15.

Trigger Source	Definition
$\text{KRICH}(K^+)$	At least six hit PMTs in the kaon RICH.
$\text{KRICH}(\pi^+)$	At least six hit pion arm PMTs of the kaon RICH.
$\text{PRICH}(\pi^+)$	At least eight hit PMTs in the pion RICH.
$\text{VVS}(1 \text{ GeV})$	At least 1 GeV in the Vacuum Veto System.
MVS	At least one hit in the Muon Veto System. (Estimate of total $K_{\mu 2}$ and halo.)

Table 15: Level-1 trigger sources.

The challenge here is to realize this simple logic while minimizing accidental vetos and coincidences from the high rate sources. We assume that the global trigger coincidence deadtime will be 10 nsec, which corresponds up to a 15% loss from accidental vetos at the trigger level. To determine this upper limit, we assume that the muon beam halo plus the *total* kaon decay rate between the upstream end of the kaon RICH and down through to the MVS can veto the trigger through accidental VVS and MVS vetos. This is clearly an overestimate, but it allows some cushion for uncertainties in the upstream beam halo and beam-detector interactions.

We are considering implementation of the Level-1 trigger in either semi-custom electronics based on commercially available logic modules and relatively few high-speed custom coincidence components or a custom digital pipeline scheme based directly on the pipeline TDC data. The semi-custom “traditional” cable-delay solution has the advantage of relying principally on available commercial hardware that is proven in the field, but has the disadvantage sub-optimal timing resolution. A custom pipelined trigger based on locally digitized PMT signals can achieve the best time resolution and provides an optimal trigger/readout scheme to understand and quantify accidental trigger effects. The feasibility of both Level-1 trigger systems described is currently under study.

This simple Level-1 trigger reduces the ~ 12 MHz of kaon decays occurring between the kaon RICH and the Muon Veto System to 220 kHz as listed in table 16. The trigger rates listed include the effect of 15% trigger deadtime. These rates are comparable to the Level-1 trigger rates of the Brookhaven E871 and KTeV experiments. The Level-1 trigger rate can be further reduced by vetoing on the total energy in the Forward Veto System and/or requiring significant hadronic energy in the muon range stack. These additional criteria can reduce the Level-1 rates substantially but at the risk

$K^+ \rightarrow \pi^+ \pi^0$	155 kHz
$K^+ \rightarrow \pi^0 e^+ \nu$	64 kHz
$K^+ \rightarrow \pi^+ \pi^+ \pi^-$	1 kHz
Total	220 kHz

Table 16: Level-1 trigger rates.

of an acceptance loss to the $K^+ \rightarrow \pi^+ \nu \bar{\nu}$ signal from the showering requirements on the charged pion. These additional cuts are currently under study, and it is likely that requiring for example less than 10 GeV in the FVS and/or at least 5 GeV of hadronic energy in the range stack can reduce the trigger rate to less than 100 kHz with a small ($\sim 5\%$) loss of signal acceptance. In parallel with the principal $K^+ \rightarrow \pi^+ \nu \bar{\nu}$ trigger other triggers will collect prescaled minimum-bias $K^+ \rightarrow \pi^+ \nu \bar{\nu}$ samples as well as triggers that address the CKM physics modes other than $K^+ \rightarrow \pi^+ \nu \bar{\nu}$ described in section 3.

For completeness we allow for the possibility of a hardware Level-2 trigger system, although from the previous discussion it is at least plausible that a relatively simple Level-1 will be adequate for the $K^+ \rightarrow \pi^+ \nu \bar{\nu}$ mode. Upon receipt of a Level-1 trigger the data acquisition system described below transfers data from the deadtimeless frontends to buffered memory. The “Level-3 trigger” is actually a software filter that is integrated into the data acquisition software environment. This data filtering architecture worked very well in both the SELEX and KTeV data acquisition “DART” systems described below. The amount of buffering and processing power must be large enough so that the Level-3 filter code isn’t a source of deadtime. Although the Level-3 and data acquisition architecture is still under design, we expect that the system will be comparable to the existing SELEX or KTeV systems. The CKM filter software will reconstruct $K^+ \rightarrow \pi^+ \nu \bar{\nu}$ events with online constants and will tag and prescale events based on electron-id, photon-id, and missing mass. As with the Level-1 trigger, a prescaled minimum-bias stream of events will be tagged with the Level-3 decision and recorded. Detailed selection criteria for the other elements of the CKM physics program will be implemented in the Level-3 filter software.

6.2 The Candidate Readout Frontends

6.2.1 SVX-3 Silicon Readout

This deadtimeless readout system is being developed for CDF, and runs with 132 nsec clock periods, with a pipelined depth of 42 ticks. Two modifications are required for CKM; a shorter pipeline and charge integral integrity across a clock boundary to support asynchronous operation. The CKM pipeline depth is determined by the latency of the Level-1 trigger, which will likely be 10 ticks (1.32 μ sec) or less long. This is a straightforward and simplifying modification to the SVX-3. Unfortunately the modification for asynchronous operation is more difficult. The current SVX-3 design is not truly pipelined, in that it is not deadtimeless over the full 132 nsec clock phase. The CDF design resets the integrated charge at the end of each clock period, which seriously degrades the Signal/Noise ratio when charge is deposited in the later half of the gate. In order to maintain an acceptable Signal/Noise as a function of clock phase, it is necessary for both the leading and

trailing slices be readout with minimal disruption at the clock boundary. Clearly R&D is required to realize this SVX-3 upgrade. Fortunately the eventual application in the field for CKM will not have to be radiation-hard since the readout electronics will be outside the beam.

6.2.2 The TMC TDC Pipeline System

The TMC TDC pipeline readout chip [80] has been under development for more than ten years now, and is quite mature. It will be employed in the D0 muon system, and much of the ATLAS tracking system [81]. The system is genuinely deadtimeless, with a base clock of 40 MHz (LHC crossing rate). Upon readout the TMC provides an ordinal number for the base clock period and a 5-bit period vernier corresponding to a least count of 0.8 nsec, with a measured sigma of 250 psec. The chip has a pipeline depth of 4 μ sec which is adequate for our application. A relevant limitation of this readout system is that the Double Pulse Resolution (DPR) is limited to the base clock period of 25 nsec. That is, a hit trailing a previous one by less than 25 nsec is lost. The impact of this deadtime is currently under study. For veto systems that are particularly vulnerable to deadtime effects the charge pulse will be digitized with the QIE system described below as well as the TMC. The deadtimeless charge profile accessible with the QIE system should enable recovery of the TMC double-pulse deadtime loss.

6.2.3 CMS HCAL QIE readout system

The CMS HCAL QIE readout system is a pipelined charge integrating system with 13 bits of dynamic range and 5 bits of resolution implemented through the “floating point” QIE readout system developed by KTeV [82]. The CMS application is the readout of the hadron calorimeter systems. This system will operate at 40 MHz, providing a 3-bit exponent and 5 bit mantissa for each 25 nsec sample contributing at most 0.7% to the resolution term from the digitization. This system has demonstrated very low noise performance in the field, so a low meaningful threshold can be imposed on the veto and calorimeter systems. The CMS QIE readout will have sufficient asynchronous performance, allowing a straightforward sum of two contiguous slices to recover the deposited charge. Every channel over threshold would have four contiguous slices readout with (3+5) bits/slice, including one early slice, two in-time slices, and one late slice. This system together with the TMC can provide a powerful digitization of each veto channel, and would likely address the deadtime concerns of the TMC system.

6.3 The Data Acquisition System

The conceptual design of the CKM data acquisition system is an extrapolation of the SELEX and KTeV “DART” systems. A block diagram of the KTeV DART system is shown in figure 24. The matrix architecture illustrated in figure 24 allows for capacity and throughput of the system to be easily expanded or contracted depending on need. Estimates of data volume and required throughput are listed in table 17 and compared to nominal and maximum KTeV & SELEX performance.

Although the estimated CKM data volume and throughput requirements are comparable to the maximum KTeV performance, the rate of events (and hence record boundaries) into buffered memory is much greater. Consequently the dual-ported buffer memory (DPM) controllers and event builder software and hardware will have to be upgraded to handle the much higher event rate. In addition, the processing power will have to be increased with respect to KTeV in order to reconstruct and filter CKM events at 60 kHz.

	CKM Requirement	KTeV Nominal	KTeV Maximum	SELEX Maximum
Spill length/Duty-factor:	1 sec/30%	20 sec/30%	20 sec/30%	20 sec/30%
Event rate to DPM:	200 kHz	10 kHz	24 kHz	5 kHz
Event size in DPM:	$\sim 1kB$	$7kB$	$64kB$	$6kB$
Data rate into DPM:	200 Mb/sec	70 Mb/sec	160 Mb/sec	30 Mb/sec
Level-3 recon. rate:	60 kHz	2 kHz	16 kHz	2 kHz
Level-3 rate to tape:	~ 1 kHz	300 Hz	4 kHz	0.2 kHz

Table 17: Comparison of estimated CKM data acquisition requirements and what has been achieved by KTeV and SELEX.

The KTeV Data Acquisition System

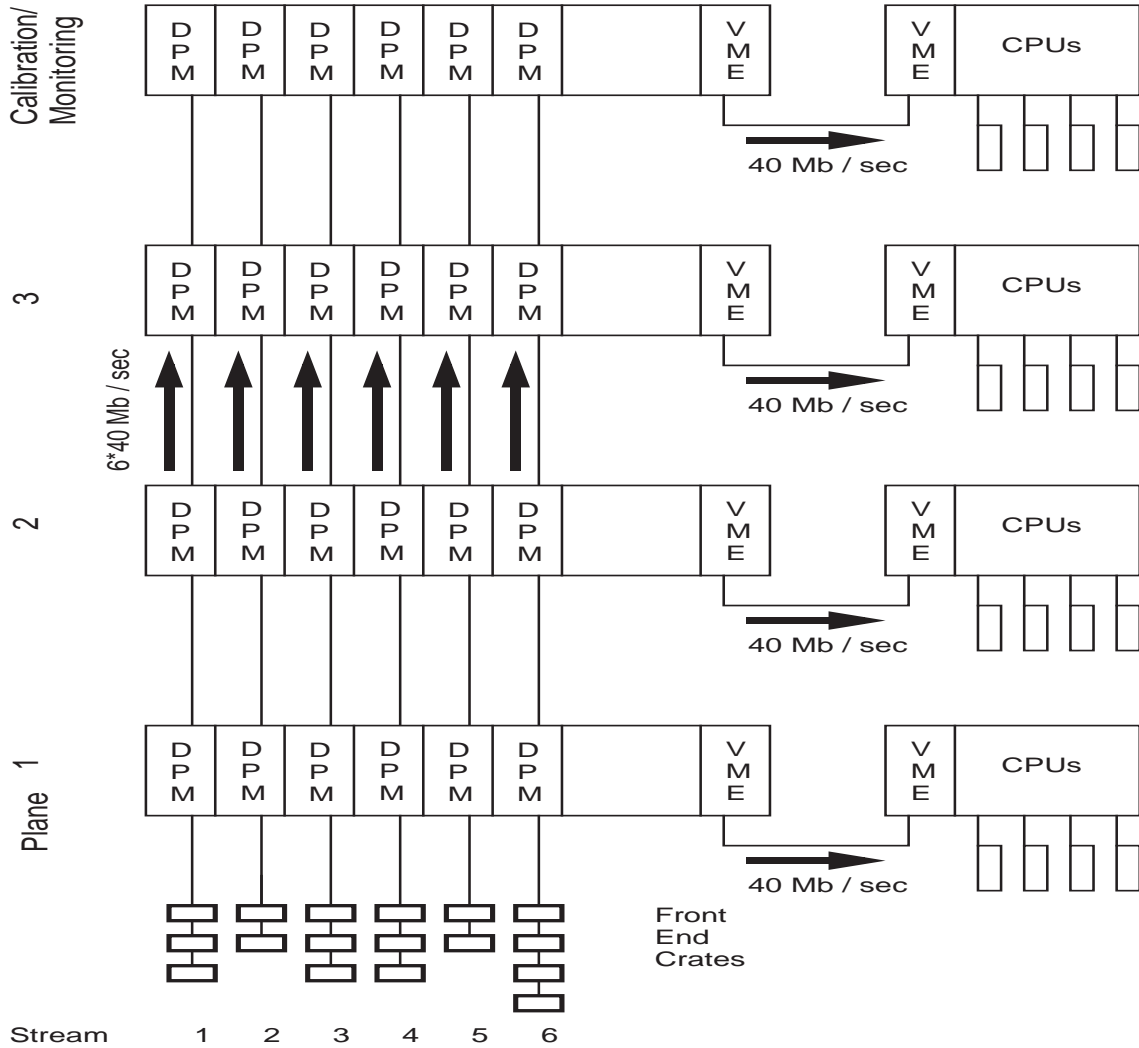


Figure 24: The KTeV Data Acquisition System.

6.4 Detector Performance Monitoring

From the previous discussions of experimental and detector requirements it is clear that all detector systems must be monitored continuously to ensure that they are live and functioning. A particularly dramatic example of the need for continuous monitoring is in the photon veto system, where a coherent failure of *just two live seconds* (2 spills) per year of operation is enough to break the inefficiency budget. There are of course several methods to trap such coherent failures, and a more significant (and more likely) concern would be more subtle longer term failures. In order to guard against such failures, every photomultiplier channel in the photon, hadron, muon veto systems will be optically flashed every second. Both RICH radiator tanks will be optically flashed every second as well in order to monitor the RICH photomultiplier arrays.

In addition to monitoring and calibration flashes, large control and calibration data sets will be acquired in parallel with the $K^+ \rightarrow \pi^+ \nu \bar{\nu}$ trigger. These data sets will be used to monitor the efficiency and performance of the RICH and magnetic spectrometers. These fully redundant spectrometers can continuously cross-monitor each other in the minimal bias data sets. Probe photons and muons from $K^+ \rightarrow \pi^+ \pi^0$ and $K^+ \rightarrow \mu^+ \nu_\mu$ decays will be employed to directly *measure* the photon and muon inefficiency of the respective veto systems. Measurement of veto inefficiencies directly from the data are crucial to demonstrate that backgrounds are under control to the required level. The direction and energy of a probe photon in $K^+ \rightarrow \pi^+ \pi^0$ decays can be calculated from the measured kinematics of the charged pion and one π^0 photon under a m_{π^0} and m_{K^+} mass constraint. Likewise, two-body kinematics from the magnetic and RICH spectrometers and a K^+ mass constraint provides a clean sample of probe muons from $K^+ \rightarrow \mu^+ \nu_\mu$ decays.

The Brookhaven experiment E787 employed this kinematic technique to measure the photon inefficiency profile shown in figure 20 from $K^+ \rightarrow \pi^+ \pi^0$ decays. Since the Brookhaven experiment detected kaon decays at rest, the maximum photon energy probed in figure 20 is 205 MeV, which of course is sufficient for that method. The sample of in-flight $K^+ \rightarrow \pi^+ \pi^0$ decays in CKM will provide tagged photons over the full relevant CKM energy range, up to ~ 10 GeV. The CKM experiment requires π^0 and muon rejection at the 2×10^{-7} level and 1×10^{-5} level respectively. Probe data samples at these levels can be collected every frequently, which will provide a continuous monitor of the photon and muon veto systems throughout the complete data set.

Detector interaction backgrounds will be measured and monitored periodically throughout the run by systematically increasing the amount of material at key detector stations such as the KEAT system and the kaon RICH. These special data sets will be used to directly test our models and understanding of detector scattering and interactions. Acquisition of these control and calibration data sets is critical to the success of the experiment, and significantly contribute to the required data acquisition specifications.

7 Simulation Results

We have performed Monte Carlo simulations to evaluate the acceptance, to estimate rates, and to study backgrounds in CKM. Most of these simulations have been performed with a Monte Carlo written specifically for CKM. Some specialized issues have been addressed by feeding events from this Monte Carlo into GEANT. Over time it is likely that we will rely more heavily on GEANT, but thus far it has been more efficient to proceed in this fashion.

7.1 Monte Carlo Overview

The CKM Monte Carlo generates beam K^+ 's with a central momentum of 22 GeV and with distributions in position, angle, and momentum corresponding to the beam design of Doornbos. It swims these particles from the upstream end of the beam RICH detector until they decay, and it subsequently swims all the daughter particles to the face of the forward veto calorimeter. The beamline upstream of the momentum spectrometer, which is upstream of the beam RICH, is not simulated beyond the generation of a Gaussian distributed value for momentum centered at 22 GeV. In the simulation of the detector important effects such as pion decay in flight, multiple Coulomb scattering and single Coulomb scatters (Mott scattering), hadronic elastic scattering, and bremsstrahlung are included. Some parameters used in this simulation are listed in table 18. For estimates of some backgrounds which involve inelastic hadronic interactions we have relied on the FRITIOF generator [84] to produce hadrons and photons which are then fed into this Monte Carlo.

The CKM Monte Carlo simulates the RICH detectors in some detail. Particles are stepped through the gas volume and in each step individual Cherenkov photons are generated. Of course, we do not generate photons which are not detected, so the number generated is a Poisson with the expected mean (from $N_{pe} = N_0 L \sin \theta_C$ with $N_0 = 150 \text{ cm}^{-1}$). In each step through the RICH multiple scattering occurs and for pions a decay to a muon is allowed with the appropriate probability. If a pion decays, then the muon is stepped forward; in the RICH it will generate photons at a different Cherenkov angle. The RICH simulation also includes chromatic dispersion by smearing the angle of each photon. The photons are then registered in a hexagonal array with the same configuration as the SELEX RICH phototube array. In the pion RICH a circular dead region is included to eliminate the hits from beamline π^+ 's. All quantities derived from the RICHs are based on a fit to the center location of hit cells. The fit does not use extra information from any other source (such as track directions from tracking chambers). Randomly located noise hits are also included at a level of 1 per event, significantly worse than anticipated in practice.

Tracking detectors are currently simulated by recording the particle's position smeared by a Gaussian resolution appropriate to that detector. Thus far no *a posteriori* track reconstruction is performed on events and no account is made for noise hits. This is a clear area for improvement, but we do not anticipate major difficulties because of the wealth of information available to constrain track hypotheses.

The effect of the spectrometer magnet on tracks is simulated as a 200 MeV p_T -kick in the horizontal plane. The momentum from the spectrometer is calculated from the smeared hit positions. While we have thus far only included Gaussian smearing of hits, large mismeasurements due to large scatters in matter (such as an elastic scatter of a pion in a chamber) are simulated.

Photons from kaon decays or other sources are swum by the Monte Carlo. The probability of detecting photons as a function of the photon energy is stored in a table. (Our assumptions for the photon veto systems are listed in table 4. When a photon reaches one of the three veto detectors (vacuum veto, forward veto, or beam hole veto), a weight is recorded which is the probability of not detecting that photon. If a photon misses all three detectors, a probability of unity is stored. Also, if a photon is within 10 cm of the charged particle at the face of the forward veto calorimeter, it is assumed to be lost (weight = 1). If an event has multiple photons, the weights of each are multiplied to provide a weight for the full event. In this way the expected veto-detector response is folded with the energy and position distributions for different classes of events (such as $K^+ \rightarrow \pi^+ \pi^0$ and $K^+ \rightarrow \mu^+ \nu_\mu \gamma$) to obtain a veto probability appropriate to each class of events. We are careful to insure that the observed charged particle in the events satisfy the cuts we make, since any bias from the cuts on the z distribution of events, energy or angle of π^0 's, etc., can affect the rejection probability.

Description	Value
Beam (magnetic) momentum resolution	0.5%
Beam RICH gas (10 m CF ₄ at 0.63 atm)	
Focal length	20 m
Index of refraction ($n - 1$)	2.9×10^{-4}
N_0 (as in $N_{pe} = N_0 L \sin^2 \theta_C$)	150 cm^{-1}
Fraction of radiation length	6.9%
Beam RICH mirror (4 mm glass)	
Fraction of radiation length	3.3%
Silicon vacuum trackers (300 μm Si)	
Position resolution (x and y)	15 μm
Fraction of radiation length/station	0.32%
K^+ Elastic cross section [†] (Si nucleus)	80 mb
K^+ Elastic slope parameter (Si nucleus)	106 GeV^{-2}
Straw vacuum trackers (5-layer mylar straws)	
Position resolution (x and y) per station	120 μm
Fraction of radiation length/station	0.22%
π^+ Elastic cross section [†] (C nucleus)	50 mb
π^+ Elastic slope parameter (C nucleus)	63 GeV^{-2}
Spectrometer Magnet	
Transverse momentum kick	200 MeV
Scintillating fiber tracker	
Position resolution (x and y) per station	120 μm
Fraction of radiation length/station	0.7%
Vacuum window	
Fraction of radiation length	0.12%
Pion RICH gas (20 m Ne at 1 atm)	
Focal length	20 m
Index of refraction ($n - 1$)	6.4×10^{-5}
N_0 (as in $N_{pe} = N_0 L \sin^2 \theta_C$)	150 cm^{-1}
Fraction of radiation length	5.8%

[†] Includes both the nuclear and nucleon components.[83]

Table 18: Parameters used in the Monte Carlo detector simulation.

An important aspect of CKM is the redundancy provided by the magnetic momentum spectrometer and the RICH velocity spectrometer. For a correct mass hypothesis they should give similar results. Since they make measurements of the momenta of both the beam K^+ and daughter π^+ with independent hardware, it is fair to combine them. We rely on the same tracking detectors to determine the angle θ between the K^+ and π^+ independent of how we obtain the momenta, so we do not average the missing masses. But we can average the momenta from each source and then calculate a combined missing mass value based on the averaged momenta. Figure 25 shows the result for $K^+ \rightarrow \pi^+ \pi^0$ decays for the missing mass for the three cases.

In addition to the Monte Carlo described above, a preliminary simulation of CKM has been made with GEANT in order to address some focused questions. GEANT's full simulation of physics processes such as Compton scattering, pair production, bremsstrahlung, energy loss, and decays enable the study processes that are not being addressed otherwise, such as photons interacting with pion RICH material.

Our GEANT simulation currently includes the kaon RICH, the vacuum vessel and its associated veto system, the pion RICH filled with neon (and its mirror) and the Forward Veto System. A dipole magnetic field of 6 kG is simulated in the vacuum vessel. We expect that this simulation will evolve in detail as our understanding of the apparatus and background issues mature.

The input to the GEANT Monte Carlo is a list of kaon decays with decay vertex and daughter momenta specified. These decays have already been accepted by analysis cuts based on simulation in the CKM Monte Carlo and written to a file for input to GEANT. For example, analysis cuts on the π^+ track in $K^+ \rightarrow \pi^+ \pi^0$ events provide a rejection of 2×10^{-6} as described in section 7.3.1. Thus, with ten million simulated GEANT events of this type, we can study photon veto and loss mechanisms for background effects below the 10^{-12} level of sensitivity.

In practice we have not simulated the full shower development of photons and electrons in the vacuum and forward veto systems. Rather, primary and daughter photons and electrons are both subjected to the photon veto efficiency profile listed in table 4. This is a conservative underestimate of the veto efficiency for electrons and positrons that result from the interaction of primary decay photons. Decay photons and photon shower products that intercept the Forward Veto System within a 10 cm radius of the charged pion track are assumed to be lost by association with the pion track cluster.

7.2 $K^+ \rightarrow \pi^+ \nu \bar{\nu}$ Acceptance

The Monte Carlo generates the $K^+ \rightarrow \pi^+ \nu \bar{\nu}$ decay using the K_{e3} matrix element and form factor. The acceptance for $K^+ \rightarrow \pi^+ \nu \bar{\nu}$ is determined by calculating the fraction of decays which pass our cuts. The detector geometry of course plays a role in the acceptance, but the detector is sized so little acceptance is lost on apertures. For example, the pion RICH has a pion Cherenkov threshold of about 12 GeV and the number of photoelectrons detected is not adequate to be useful below about 14 GeV. Consequently our acceptance is limited by a minimum pion momentum of 14 GeV, but for pions above 14 GeV the maximum transverse excursion is small enough that we can afford to collect almost all of them. Equally important are cuts we have devised to reject backgrounds. Two closely related examples are a cut on the reconstructed vertex location (the apparent K^+ decay position as determined by the point of closest approach of the K^+ and π^+ tracks) and on the angle between the K^+ and π^+ tracks. We require this measured decay angle to be larger than 2.5 mrad, because below that the vertex resolution (along the beam direction, z) degrades quickly. Figure 26 shows the resolution obtained on vertex z -position for $K^+ \rightarrow \pi^+ \nu \bar{\nu}$ events. We cut on the vertex location, specifically requiring it to be 5 meters away from the nearest tracking detectors, because interactions or large scatters in those detectors are a major potential sources of background. Having made these

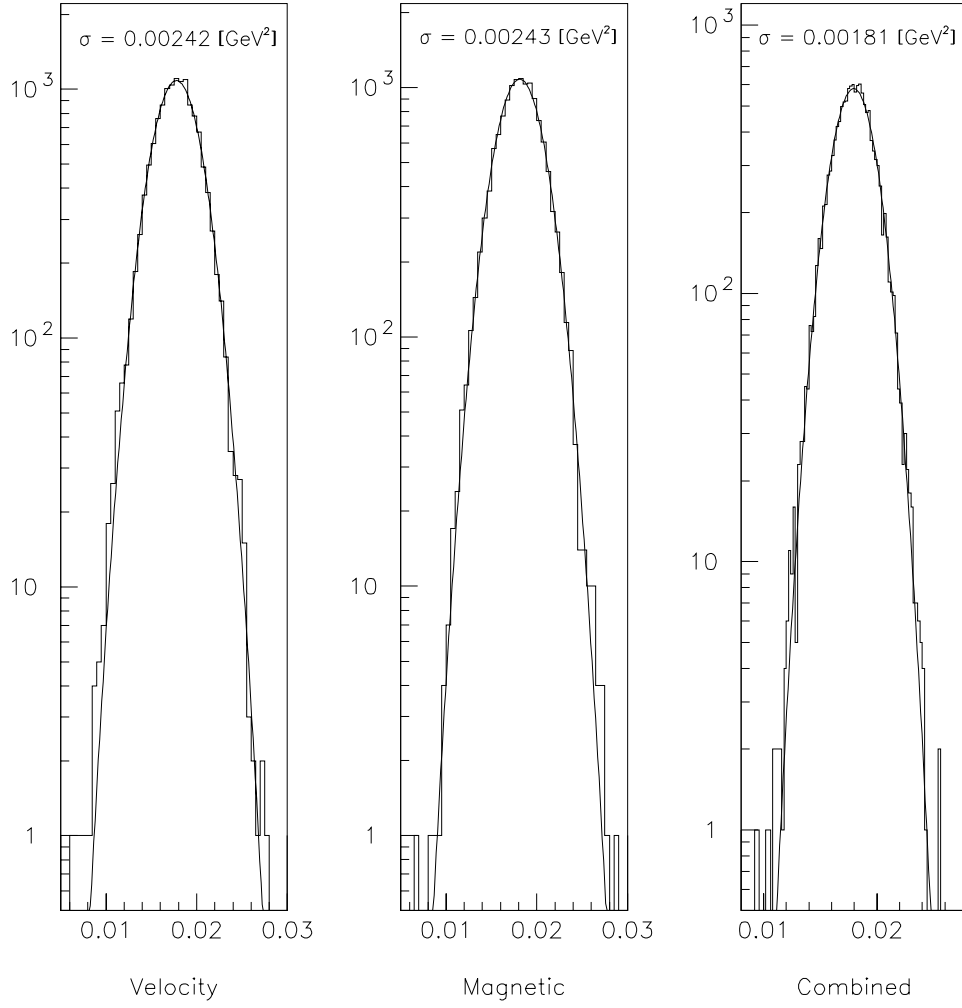


Figure 25: The resolution in missing mass squared in $K^+ \rightarrow \pi^+ \pi^0$ decays for the three methods of determining it as described in the text. About 20,000 events are shown.

two cuts, the subsequent loss in acceptance from the inner aperture of the straw chambers is small.

We have developed a set of cuts based primarily on background rejection considerations while trying to maintain good acceptance for $K^+ \rightarrow \pi^+ \nu \bar{\nu}$. They fall into five categories:

- Aperture cuts. These simply require accepted charged particles to remain inside the outer detector boundaries and outside the beam hole region.
- RICH cuts. These are designed to insure good results from the RICH detectors. They consist of:
 1. Beam RICH: between 6 and 20 hits (photoelectrons).
 2. Pion RICH: 8 or more hits, with at least one in each quadrant of the fit ring.
 3. Both RICHs: a cut on the quality of fit.
- Vertex cuts. These primarily reject backgrounds from interactions in detector material. They consist of:
 1. $\theta > 2.5$ mrad, a requirement that the reconstructed angle between the K^+ and π^+ be large enough to permit good vertex z measurement.
 2. $20 \text{ m} < z_{\text{vertex}} < 40 \text{ m}$, a requirement that the reconstructed vertex position be 5 m from the nearest material. The fitted sigma vertex resolution as seen in figure 26 is 18cm. The relatively large cut of 5 m ensures that the tails visible in figure 26 are eliminated.
 3. $\text{DOCA} < 0.6 \text{ cm}$, the reconstructed distance of closest approach between the K^+ and π^+ must be less than 0.6 cm, as shown in figure 27.
 4. $\sqrt{x_{\text{vertex}}^2 + y_{\text{vertex}}^2} < 10 \text{ cm}$, the vertex location should be near the beam.
- Spectrometer cuts. These cuts primarily require the magnetic spectrometer and velocity spectrometer measurements to agree. Since the pion mass hypothesis is assumed for the velocity spectrometer, these cuts have the effect of rejecting muons based on RICH information, along with other event pathologies (e.g., π^+ decay in flight, large scatters or energy loss in some areas, etc.). They consist of:
 1. Beam particle momentum: $|p_{\text{magnetic}} - p_{\text{RICH}}|/p_{\text{RICH}} < 0.025$
 2. Non-bend plane track angle match through downstream spectrometer magnet: $\Delta|\theta_y| < 1.5 \text{ mrad}$
 3. Secondary (decay) particle momentum: $|p_{\text{magnetic}} - p_{\text{RICH}}|/p_{\text{RICH}} < 0.05$
 4. Missing mass: $|M_{\text{magnetic}}^2 - M_{\text{RICH}}^2| < 0.01 \text{ GeV}^2$ (see figure 28)
 5. $14 < p_{\text{RICH}} < 20 \text{ GeV}$
- Signal region. This selects the region of phase space between the $K_{\mu 2}$ and $K_{\pi 2}$ peaks and consequently rejects those decays based on two-body kinematics. The selection is based on the missing mass value from combining the momentum spectrometer and velocity spectrometer information: $0 < M_{\text{combined}}^2 < 0.008 \text{ GeV}^2$

For $K^+ \rightarrow \pi^+ \nu \bar{\nu}$ decays within the decay volume, the set of cuts previously described accept 1.83% of events. If we are ultimately able to include events below the $K_{\pi 2}$ peak, the acceptance can be more than doubled. Figure 29 shows the missing mass distribution for $K^+ \rightarrow \pi^+ \nu \bar{\nu}$ events pass all cuts (except on missing mass).

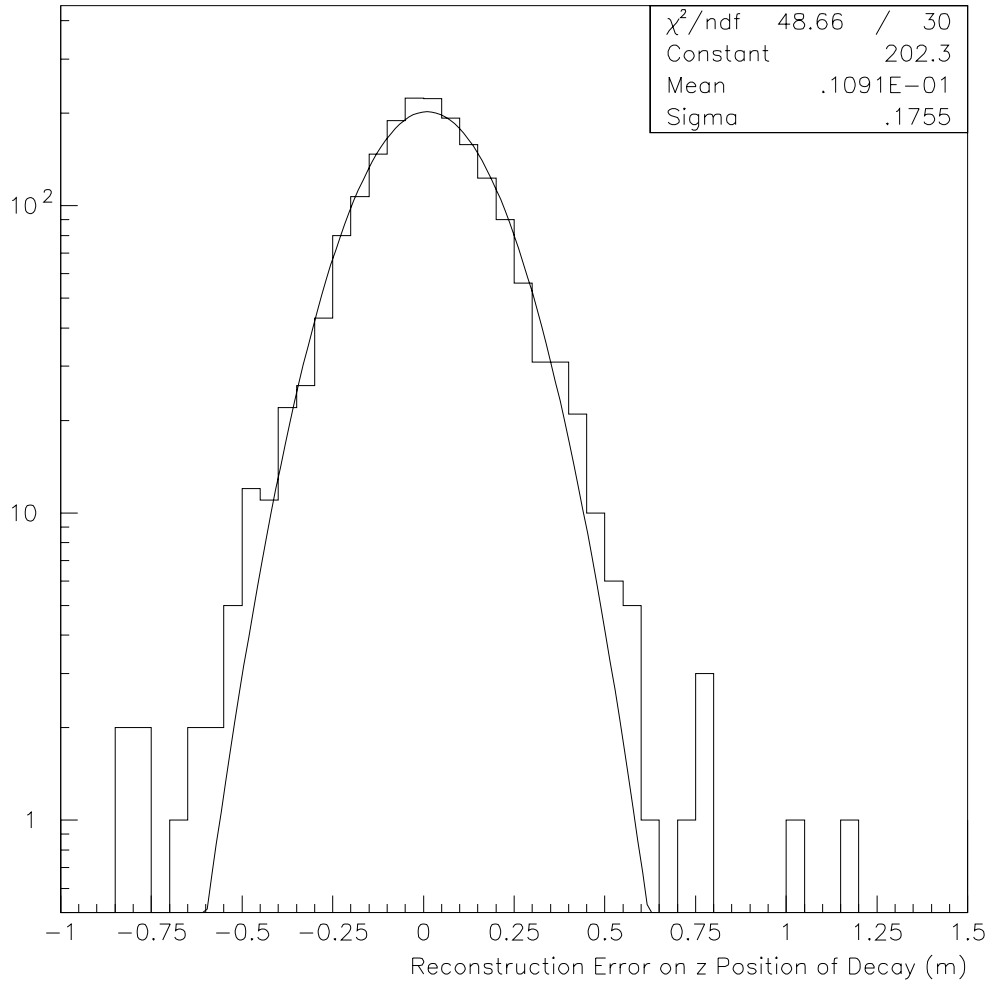


Figure 26: Distance between measured vertex location and actual decay position in $K^+ \rightarrow \pi^+ \nu \bar{\nu}$ events. The fitted resolution sigma is $\sim 18\text{cm}$, with non-Gaussian tails originating from hard scatters included in the tracking simulation.

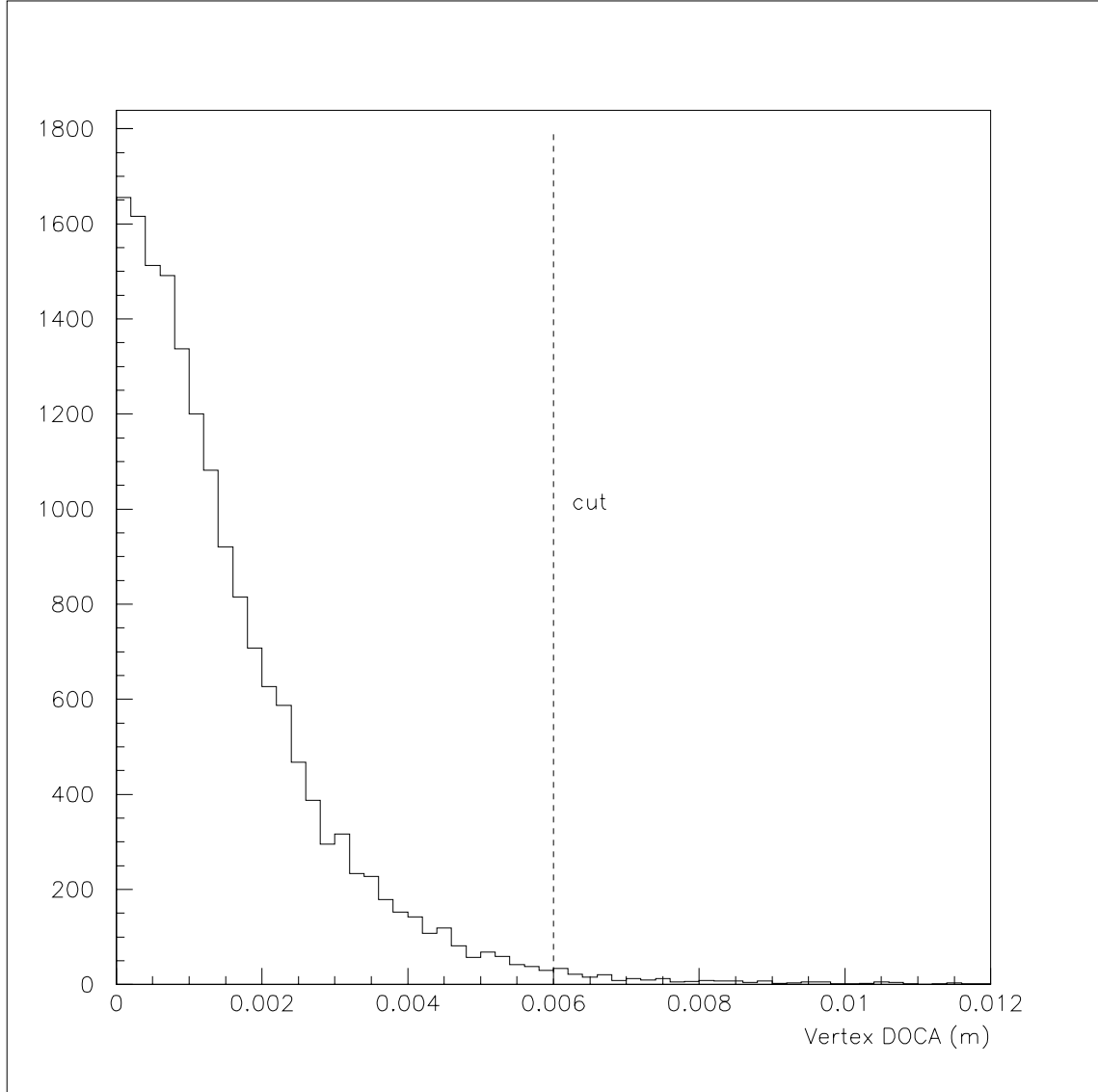


Figure 27: Measured distance of closest approach ($DOCA$) for the K^+ and π^+ in $K^+ \rightarrow \pi^+ \nu \bar{\nu}$ events.

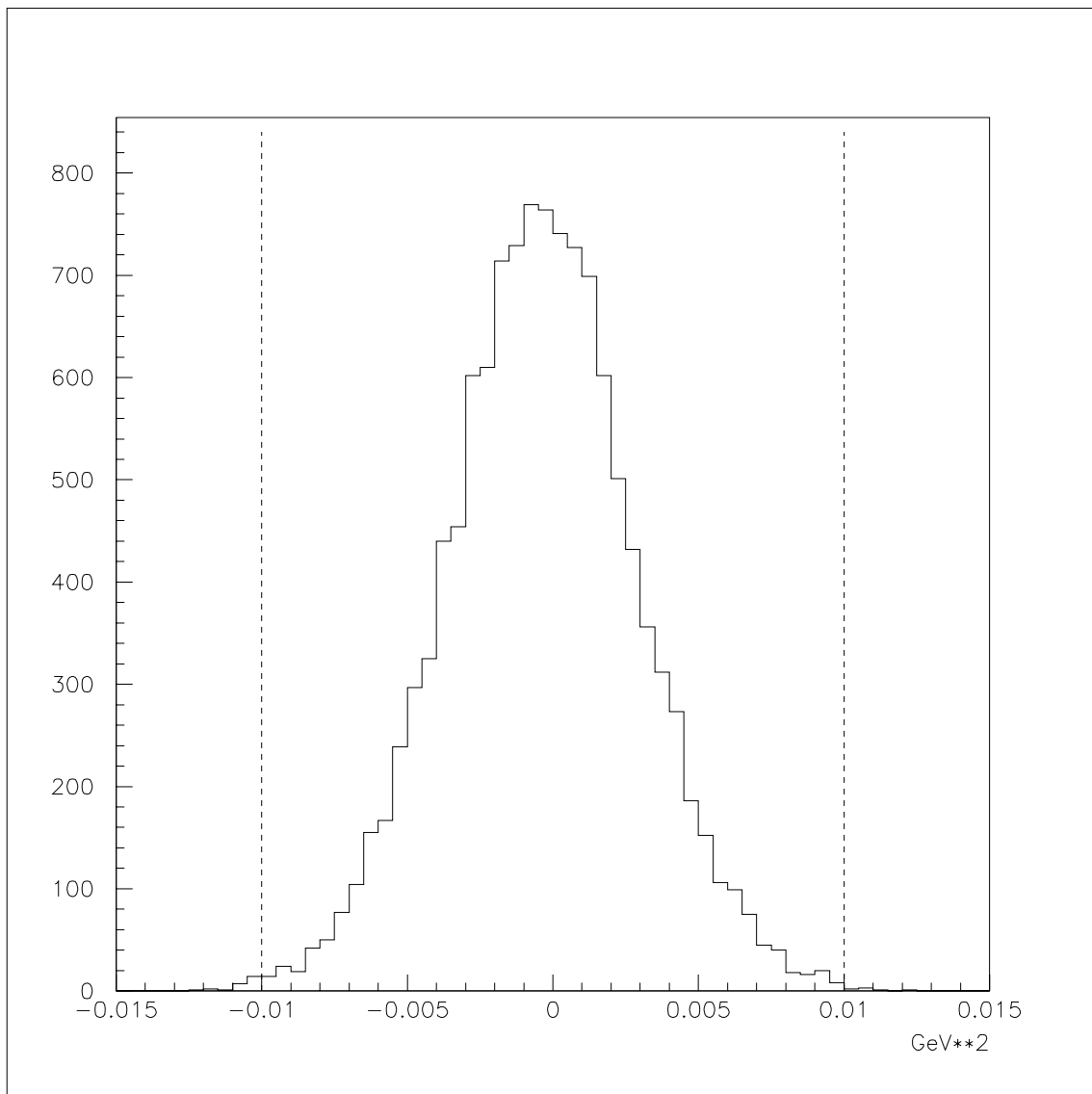


Figure 28: Difference in measured missing mass squared from the momentum and velocity measurements ($M_{\text{magnetic}}^2 - M_{\text{RICH}}^2$) for $K^+ \rightarrow \pi^+ \nu \bar{\nu}$ events.

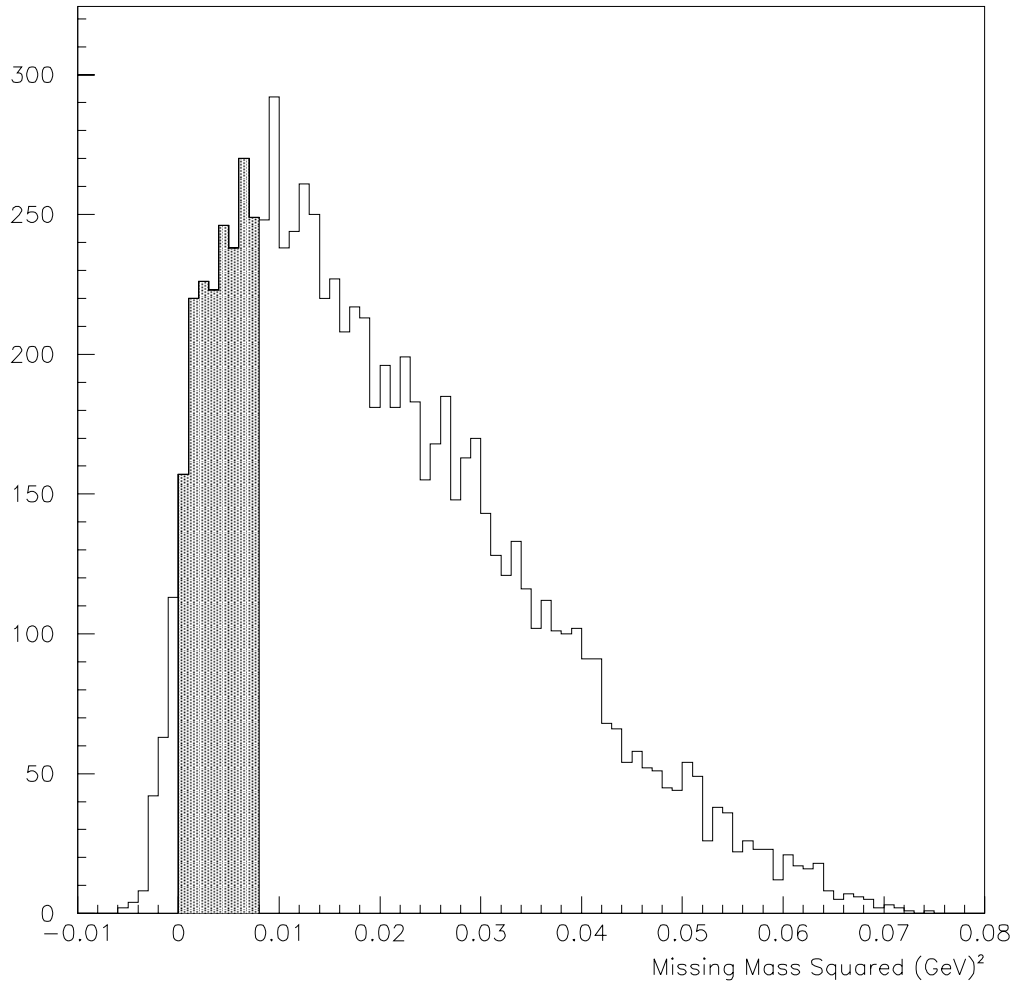


Figure 29: Measured missing mass squared (M^2_{combined}) in $K^+ \rightarrow \pi^+ \nu \bar{\nu}$ events. The signal region is shaded.

Loss Mechanism	Inefficiency
Trigger deadtime:	15%
MVS π/μ separation cuts:	5%
UMS/DMS tracking:	5%
Accidental losses at analysis: (Balance after trigger deadtime losses.)	5%
Double K^+ ambiguity in kRICH:	5%
Total miscellaneous inefficiency:	30%

Table 19: Miscellaneous inefficiency table.

Inefficiencies due to trigger deadtime, accidental losses, etc, are not simulated in this Monte Carlo. These loss mechanisms listed in table 19 have been discussed in previous sections, and correspond to an additional acceptance loss of $\sim 30\%$. Taking this into account, the final $K^+ \rightarrow \pi^+ \nu \bar{\nu}$ acceptance is about 1.25%. This is the number used in this proposal to calculate the CKM sensitivity.

7.3 Kaon Decay Backgrounds

For the signal region considered here, between the $K_{\mu 2}$ and $K_{\pi 2}$ peaks, only three kaon decays are potentially significant sources of background to a $K^+ \rightarrow \pi^+ \nu \bar{\nu}$ search. They are the two decays making up these peaks and the radiative tail of the lower missing mass peak. That is, we must consider $K^+ \rightarrow \pi^+ \pi^0$, $K^+ \rightarrow \mu^+ \nu_\mu$, and $K^+ \rightarrow \mu^+ \nu_\mu \gamma$.

As a matter of convention we will quote background estimates in terms of an “effective branching ratio.” This quantity must depend inversely on the acceptance for $K^+ \rightarrow \pi^+ \nu \bar{\nu}$ because a smaller signal acceptance means it will require more K^+ ’s into the experiment, which in turn increases the number of background events. The effective branching ratio multiplied by the single event sensitivity for $K^+ \rightarrow \pi^+ \nu \bar{\nu}$ gives the number of expected events from that background. Since the deadtime and losses listed in table 19 are common to both the $K^+ \rightarrow \pi^+ \nu \bar{\nu}$ signal and backgrounds, we use the pre-loss $K^+ \rightarrow \pi^+ \nu \bar{\nu}$ acceptance for in the background estimates.

7.3.1 $K^+ \rightarrow \pi^+ \pi^0$ Background Study

The $K^+ \rightarrow \pi^+ \pi^0$ decay is the most serious kaon decay background for CKM. Its suppression depends critically on excellent π^0 rejection and on excellent kinematic reconstruction (i.e., measurement of the beam K^+ and daughter π^+ momenta and the angle between them) in order to exploit the two-body kinematics.

An attractive feature of K^+ decays in-flight is the boost of most photons to relatively high energies. Even though a small fraction (about 0.1%) of photons may have exceedingly low energy, below 20 MeV (the minimum for $K^+ \rightarrow \pi^+ \pi^0$ decays at rest), we are assured that the other photon has energy of 2 GeV or more. This is a simple consequence of starting with a 22 GeV K^+ and requiring the π^+ energy to be less than 20 GeV. As a result the sum of the energies of the two photons must be 2 GeV or more.

We have estimated the π^0 rejection in $K^+ \rightarrow \pi^+ \pi^0$ via Monte Carlo by using a sample of $K^+ \rightarrow \pi^+ \pi^0$ decays that pass all cuts, except the $0 < M_{\text{combined}}^2 < 0.008 \text{ GeV}^2$ cut which needlessly lowers statistics. For these events both photons are swum from the point of the K^+ decay until they intercept veto detectors. Then a weight, equal to the probability of not rejecting the

photon, is determined for the particular veto system it hit based on the energy of the photon. Photon veto probabilities are listed in table 4 for each veto system. The two weights are multiplied together to get the probability of not vetoing that event. Over a large event sample we determine the appropriate π^0 rejection for this class of events.

Some photons, only rarely, may miss all veto detectors; this can occur if the decay occurs far downstream of the required $20\text{ m} < z_{\text{vertex}} < 40\text{ m}$ fiducial region. In such events a wide-angle photon can miss both the vacuum veto and the forward veto by exiting the pion RICH at a large angle. This type of event only occurs when the vertex position is badly mismeasured, not as a result of simple resolution smearing. In particular, large hadronic elastic scattering of the π^+ in the first straw chamber can create this type of mismeasurement. This effect is included in the Monte Carlo. Any such photons are given a weight of unity.

Another source of photons being missed is coalescence with the π^+ in the forward veto detector. It may or may not ultimately be possible to make a cut on electromagnetic energy deposited close to a π^+ , but for now we have made the conservative assumption that any photon within 10 cm of the π^+ is lost.

Two topologies of $K^+ \rightarrow \pi^+\pi^0$ events limit π^0 rejection in CKM: (1) those with one photon below 20 MeV that is unlikely to be vetoed and (2) those with one photon within 10 cm of the π^+ . In both cases the π^0 rejection depends on vetoing the other photon. Our Monte Carlo result for π^0 rejection in $K^+ \rightarrow \pi^+\pi^0$ events is 1.6×10^{-7} .

We have considered some additional scenarios not simulated in the MC and have used GEANT to estimate them. A photon may also convert to an e^+e^- pair as it traverses tracking planes, the vacuum window, the RICH gas and mirror, and any other material the detector presents to it. In most cases the rejection will not be degraded because the e^+e^- pair will reach the veto detector and deposit energy very much as the photon would have. Also, if a relatively energetic photon converts in the pion RICH gas, it is likely to be detected by the RICH itself. However, in a small number of cases, typically where the photon had little energy, the e^+e^- pair may be lost. We have investigated these losses using GEANT (see section 7.4). Our conclusion is that the effect of these losses enters below the 10^{-7} level in π^0 rejection.

Also, in $K^+ \rightarrow \pi^+\pi^0$ the π^0 may Dalitz decay, giving a photon and e^+e^- pair instead of two photons. Most of the comments above concerning external conversion apply here as well. However, almost all external conversions will occur downstream of the spectrometer magnet, while all the relevant Dalitz decays will occur upstream of the magnet. Consequently the effect of the magnetic field on the e^+e^- pair will be more important for these events. An example of such a Dalitz event is shown in figure 32. This issue has also been addressed using GEANT with the result that Dalitz decay also enters below the 10^{-7} level in π^0 rejection.

We have simulated 5×10^6 $K^+ \rightarrow \pi^+\pi^0$ decays. The analysis cuts we make were listed in section 7.2. Figure 30 shows the missing mass distribution for events passing all cuts (except the requirement on missing mass itself). Ten events appear in the signal region $0 < M_{\text{miss}}^2 < 0.008\text{ GeV}^2$. From this we can estimate our overall $K^+ \rightarrow \pi^+\pi^0$ rejection in terms of an effective branching ratio:

$$B_{\text{eff}} = \left(\frac{1}{\epsilon_{\pi\nu\nu}} \right) (B(K^+ \rightarrow \pi^+\pi^0)) (\text{fraction } K^+ \rightarrow \pi^+\pi^0 \text{ passing cuts}) (\pi^0 \text{ rejection}) \quad (17)$$

$$B_{\text{eff}} = \left(\frac{1}{0.018} \right) (0.21) \left(\frac{10}{5 \times 10^6} \right) (1.6 \times 10^{-7}) = 3.7 \times 10^{-12}. \quad (18)$$

Mismeasurement of the angle θ between the K^+ and π^+ , due primarily to hadronic elastic scattering in the trackers, is a limiting contribution to the kinematic rejection of events. Inelastic hadronic interactions may also corrupt events. These have not been included in the $K^+ \rightarrow \pi^+\pi^0$ simulation

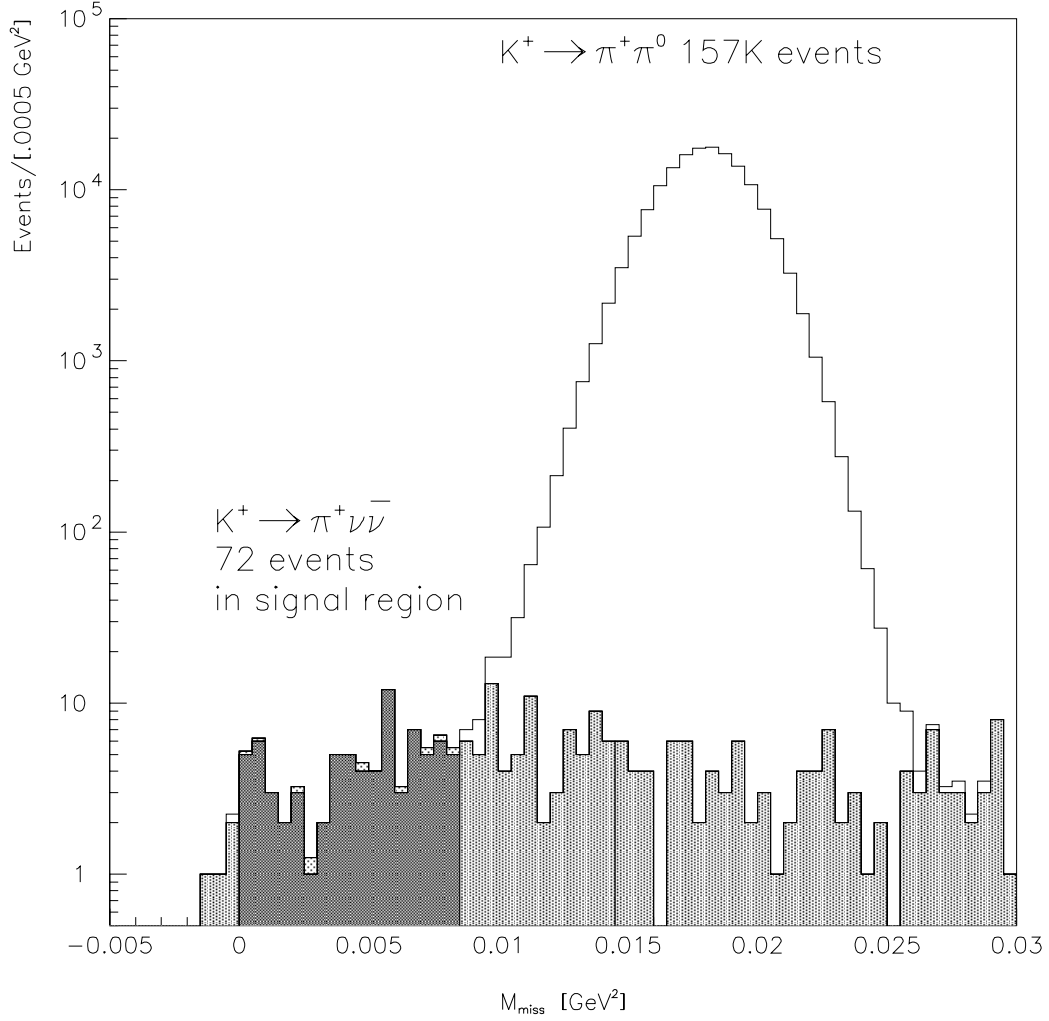


Figure 30: Missing mass squared (M_{combined}^2) for $K^+ \rightarrow \pi^+ \pi^0$ events passing all cuts superimposed on the signal (light shading). The sensitivity shown in this plot corresponds to the experimental sensitivity of 72 $K^+ \rightarrow \pi^+ \nu \bar{\nu}$ events in our mass window (single event sensitivity of 1.4×10^{-12}) which are indicated with the dark shading.

thus far. We believe the contribution of inelastic interactions to backgrounds should be significantly less than elastic scatters.

Several features of inelastic events will provide additional rejection. If the K^+ interacts inelastically in the last tracker, evidence via extra hadrons will show up in the Beam Interaction Veto System. The energy of the K^+ will be reduced in the interaction before it decays, so that the DMS and beam RICH will have overestimated the momentum of the K^+ when it decays. This has the effect of increasing the calculated missing mass and moving it farther from our signal region. If the daughter π^+ interacts inelastically in the first vacuum straw chamber, it will lose energy before its momentum is measured, so the effect will be a mismeasurement on the low side. This again favors background rejection since it increases the missing mass and moves it farther from the signal region. And of course, such an inelastic interaction will produce additional particles in the detector that will provide significant rejection. Needless to say, the contribution to $K^+ \rightarrow \pi^+ \pi^0$ backgrounds from inelastic interactions needs to be addressed in a more quantitative fashion and that is our plan. However, it is unlikely to compete with the processes we have simulated.

7.3.2 $K^+ \rightarrow \mu^+ \nu_\mu$

The most common K^+ decay is $K^+ \rightarrow \mu^+ \nu_\mu$ and it is a potentially serious background to $K^+ \rightarrow \pi^+ \nu \bar{\nu}$. As a two-body decay, it can be rejected kinematically. Also, CKM will have powerful rejection against muons because of both the pion RICH and the muon veto system. Potential background arises primarily when either the beam K^+ or the μ^+ scatters at large angle and introduces a mismeasurement of the angle between the K^+ and μ^+ . In fact, the probability of a large hadronic scatter of the K^+ is significantly larger than a large μ^+ Mott scatter. The locations where such scatters are dangerous are in the last tracking plane the K^+ traverses and in the first tracking plane the μ^+ traverses (scatters in other locations do not induce a mismeasurement of the angle between the K^+ and μ^+). Consequently these trackers must be very low-mass devices. Cuts on vertex quality are highly effective in rejecting such events.

One issue in analyzing these events is how to include the RICH rejection of muons. The traditional method would be to use the momentum measurement from the magnetic spectrometer to estimate the expected Cherenkov ring radius of a pion, and then to reject events when the measured ring is not consistent with this value. Here we choose to use the RICH information to calculate the event kinematics under the assumption that the observed particle is a pion. Then we can compare these (velocity spectrometer) kinematic quantities to the same quantities based on the magnetic spectrometer and reject events where they differ significantly.

This may seem at first an unnatural way to perform the analysis. Perhaps it would be if $K^+ \rightarrow \mu^+ \nu_\mu$ were the only source of events (other than $K^+ \rightarrow \pi^+ \nu \bar{\nu}$). We make this choice because we wish to use measurements from the velocity spectrometer to improve our kinematic resolution by combining that information with measurements from the magnetic spectrometer. For decays such as $K^+ \rightarrow \pi^+ \pi^0$, where the assumed mass hypothesis is correct, the improvement in kinematic resolution is significant. When the mass hypothesis is wrong, the kinematic quantities will differ wildly and we can reject the events on that basis. Figure 31 shows the momentum and missing mass determined from both sources for a sample of $K^+ \rightarrow \mu^+ \nu_\mu$ decays and their differences.

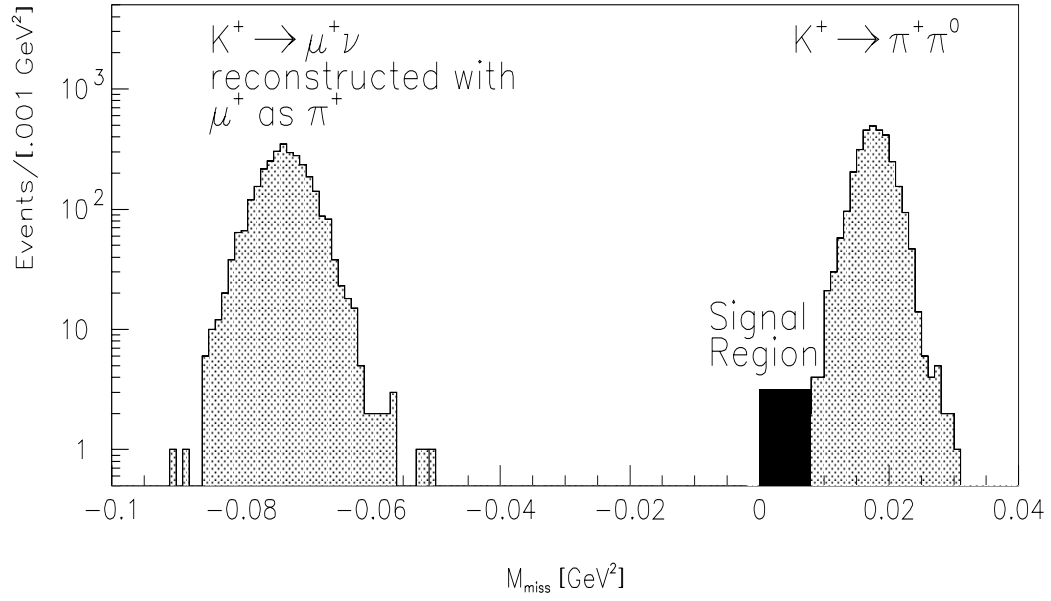


Figure 31: Missing mass of $K^\pm \rightarrow \mu^\pm \nu_\mu$ decays where the muon is reconstructed under the pion mass hypothesis.

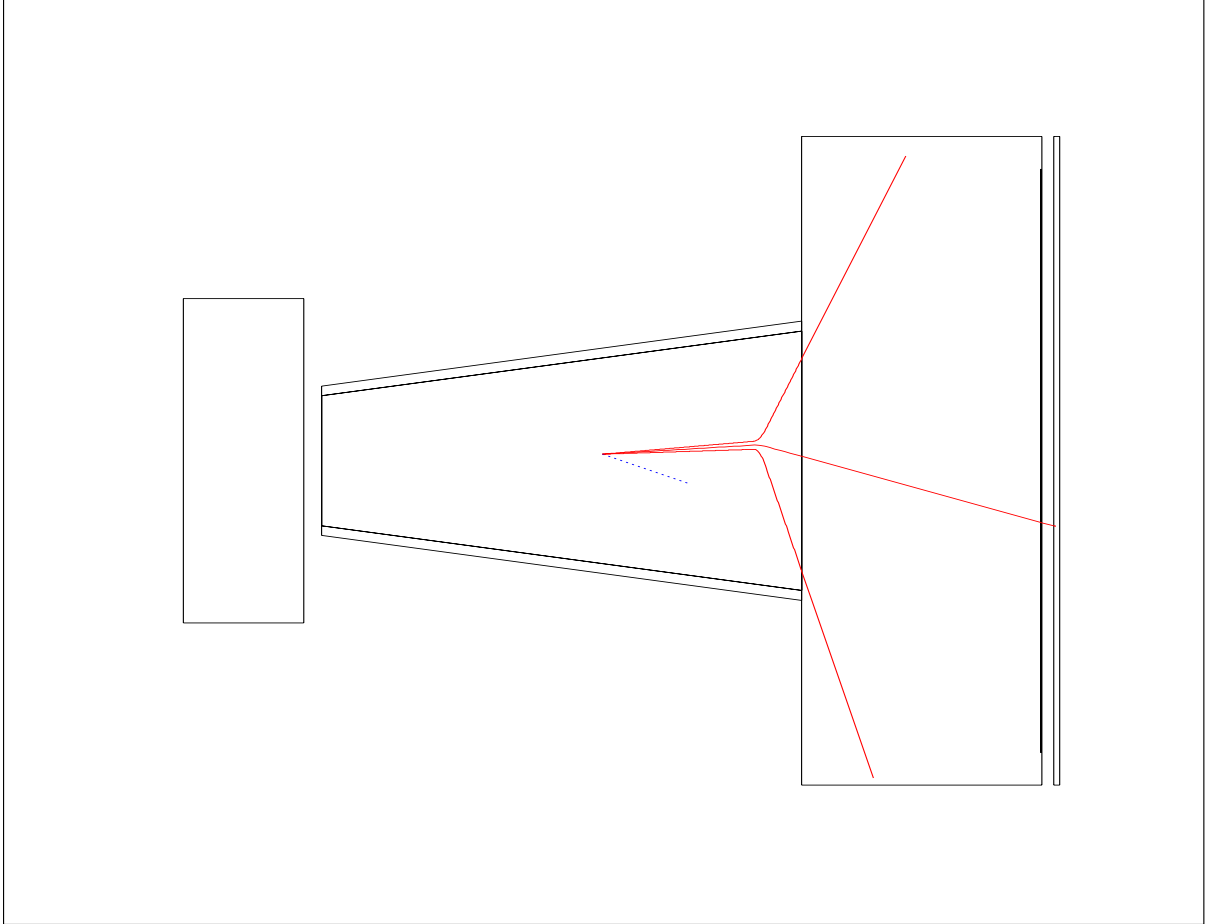


Figure 32: A GEANT simulation of a common Dalitz decay topology where the electron and positron tracks are kicked out of the photon veto system coverage by the $200 \text{ MeV}/c$ p_T -kick magnet. Fortunately the rejection of the remaining photon together with the low Dalitz decay branching fraction set the scale of this problem topology to be low at the outset.

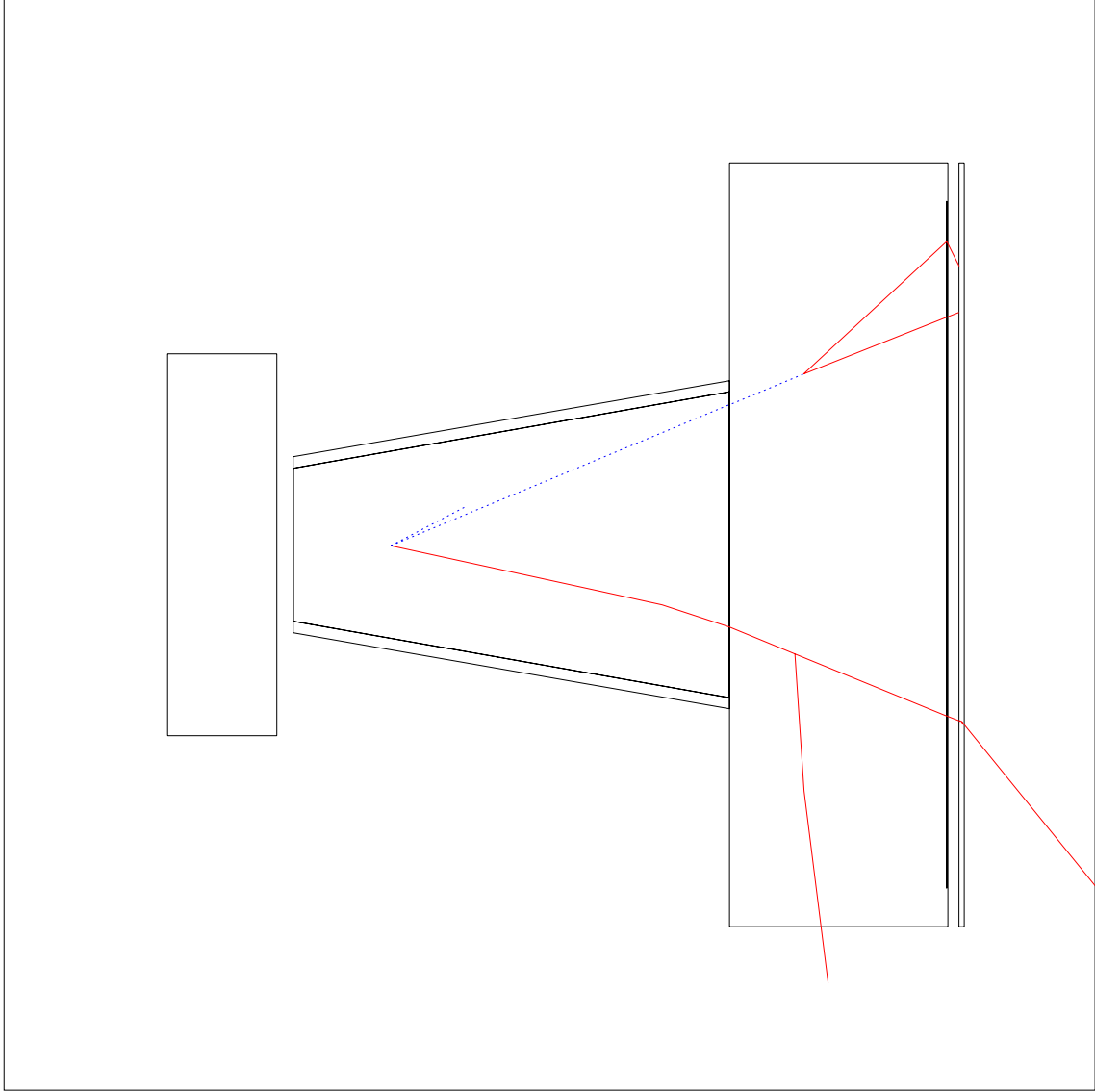


Figure 33: A typical GEANT event where one of the decay $K^+ \rightarrow \pi^+\pi^0$ photons converts in the pion RICH gas. Photons are dot-trajectories and charged particles are dashed-trajectories. The photon entering the pion RICH volume is seen to convert in the neon gas, and the charged pion (lower track) produces a hard delta-ray in the neon gas as well.

An important part of our rejection of $K^+ \rightarrow \mu^+ \nu_\mu$ comes from the muon rejection of the Muon Veto System. We will use the conservative value of 1×10^{-5} for muons in the range of 14 to 20 GeV.

To reach a simulation sensitivity of 10^{-12} we would need to simulate 5×10^8 events based on this level of muon rejection. Instead we have simulated a smaller number of $K^+ \rightarrow \mu^+ \nu_\mu$ decays in which large scatters are forced, due to hadronic elastic scattering for the K^+ and single Coulomb (Mott) scattering for the μ^+ . We have simulated these two scenarios separately, running 2×10^6 events of the first kind and 1×10^6 events of the second, much less likely, kind. We apply the cuts listed in section 7.2 to determine the fraction of events of either type which satisfy all analysis cuts and fall inside the signal region. No background events appear at this level. The probability of an elastic K^+ scatter in the last silicon plane is 1.2×10^{-4} and the probability for a Mott scatter in the first straw chamber is 3.6×10^{-5} . (The Mott cross section goes as $1/q^4$ and this probability corresponds to a small angle cut-off of 2 mrad in the center of mass.) Thus, the effective branching ratio limit on this background is:

$$B_{\text{eff}} = \left(\frac{1}{\epsilon_{\pi\nu\nu}} \right) (B(K^+ \rightarrow \mu^+ \nu_\mu)) (\text{fraction } K^+ \rightarrow \mu^+ \nu_\mu \text{ events passing cuts}) (\text{muon rejection}) \quad (19)$$

$$B_{\text{eff}} = \left(\frac{1}{0.018} \right) (0.64) \left[(1.2 \times 10^{-4}) \left(\frac{\leq 1}{2 \times 10^6} \right) + (3.6 \times 10^{-5}) \left(\frac{\leq 1}{1 \times 10^6} \right) \right] (1 \times 10^{-5}) < 3.4 \times 10^{-14}. \quad (20)$$

7.3.3 $K^+ \rightarrow \mu^+ \nu_\mu \gamma$ Background Study

The $K^+ \rightarrow \mu^+ \nu_\mu \gamma$ decay with branching fraction 5×10^{-3} is potentially dangerous because it is not a two-body decay. That is, the presence of the photon has the effect of removing the constraint of two-body kinematics. It can populate the signal region we have defined. Some addition rejection is available because of the photon, but that rejection is limited by a couple of factors: (1) the photon tends to have low energy and (2) the photon tends to be colinear with the μ^+ so that our non-coalescence criterion (10 cm separation at the forward photon veto) may not be satisfied; of course the spectrometer magnet helps by deflecting the muon. Our calculated rejection for the $K^+ \rightarrow \mu^+ \nu_\mu \gamma$ photon is 6×10^{-2} .

We have simulated 2×10^6 $K^+ \rightarrow \mu^+ \nu_\mu \gamma$ events in CKM. At this level no events pass all analysis cuts. Thus, the effective

$$B_{\text{eff}} = \left(\frac{1}{\epsilon_{\pi\nu\nu}} \right) (B(K^+ \rightarrow \mu^+ \nu_\mu \gamma)) (\text{fract } K^+ \rightarrow \mu^+ \nu_\mu \gamma \text{ pass cuts}) (\gamma \text{ rejection}) (\mu \text{ rejection}) \quad (21)$$

$$B_{\text{eff}} = \left(\frac{1}{0.018} \right) (5 \times 10^{-3}) \left(\frac{\leq 1}{2 \times 10^6} \right) (6 \times 10^{-2}) (1 \times 10^{-5}) < 8.3 \times 10^{-14}. \quad (22)$$

7.4 Photon loss mechanisms in detector material

Decay photons from $K^+ \rightarrow \pi^+ \pi^0$ and $K^+ \rightarrow \mu^+ \nu_\mu \gamma$ that are born in the vacuum decay volume must traverse the material of the downstream spectrometer and the pion RICH before intercepting the Foward Veto System. Since the walls of the pion RICH are inactive, it is possible for decay photons to get lost in the pion RICH through conversion, scattering, and energy loss mechanisms. In principle the pion RICH itself can contribute to the identification of conversion electrons and positrons if they are produced above Cherenkov threshold (41 MeV) and within the angular acceptance of the RICH. To be conservative we have ignored this potential rejection power in evaluating this loss mechanism.

Figure 33 shows one such $K^+ \rightarrow \pi^+\pi^0$ decay in our GEANT simulation, with one of the photons from the π^0 decay interacting in the gas inside the pion RICH detector. Despite the clear presence of events of this nature, ten million GEANT events were simulated and only two events were not vetoed. These two events were lost to the nominal inefficiencies listed in table 4, and not to material interactions in the pion RICH. This inefficiency level of $\sim 2 \times 10^{-7}$ is consistent with the $K^+ \rightarrow \pi^+\pi^0$ background estimate described early based on a weighted Monte Carlo technique. Further investigation into the loss mechanisms for photons will be performed using this simulation.

7.5 Beam-Detector Interaction Backgrounds

Hadronic interactions of a beam K^+ or π^+ , or of a daughter π^+ from a K^+ decay, can create backgrounds in a $K^+ \rightarrow \pi^+\nu\bar{\nu}$ search. Hadronic interactions were identified as a problem in the 1989 Main Injector Workshop report [39] on $K^+ \rightarrow \pi^+\nu\bar{\nu}$ in-flight (which referred to “window scattering events”) and were deemed to be the limiting background for an in-flight $K^+ \rightarrow \pi^+\nu\bar{\nu}$ search. While further improvement is planned in our simulation of these effects, we have gone far beyond any previous effort to understand how they affect an in-flight $K^+ \rightarrow \pi^+\nu\bar{\nu}$ search.

It should be emphasized that hadronic scattering in $K^+ \rightarrow \pi^+\pi^0$, $K^+ \rightarrow \mu^+\nu_\mu$, and $K^+ \rightarrow \mu^+\nu_\mu\gamma$ decays was accounted for in the background estimates already discussed. Here we are concerned with other background scenarios where a hadronic interaction causes an event to fake $K^+ \rightarrow \pi^+\nu\bar{\nu}$. To study these problems, we have used the same Monte Carlo described earlier to swim particles and to simulate the CKM detector. However, as a starting point (generator) for inelastic hadronic interactions we have used the FRITIOF program [84]. This is a standard program for hadron-nucleus interactions which is part of the Lund Monte Carlo family.

We have taken steps in the CKM design to minimize hadronic interactions in critical locations by putting tracking detectors inside vacuum and minimizing the mass of those detectors. As will be discussed below, the most dangerous location for inelastic hadronic interactions is in the last beam vacuum tracker. To achieve extra rejection for these events, the CKM design includes a special veto device (Beam Interaction Veto System) immediately downstream of the last beam tracker. Most hadronic interactions will create extra particles, and the Beam Interaction Veto System is designed to detect the low-energy, wide-angle charged and neutral hadrons coming from hadronic interactions in the last beam vacuum tracker.

7.5.1 Charge-Exchange

The most complicated potential background occurs when a beam K^+ hadronically interacts in material upstream of the decay volume to produce a high momentum K_L which subsequently decays via $K_L \rightarrow \pi^+e^-\nu$ inside the decay volume. The resulting π^+ comes from a three-body kaon decay with two effectively massless partners, so kinematically it is similar to $K^+ \rightarrow \pi^+\nu\bar{\nu}$. The extra electron may provide a veto signature, but in rare cases the electron may be missed. It is conventional to refer to this as the charge-exchange background.

Because the K_L is long-lived, the offending K^+ interaction can occur far upstream of the detector. However, in that case it is necessary for the interaction also to create another charged particle to provide the requisite hits in the beam vacuum trackers. Interactions in the beam RICH may accomplish this, but if the K^+ interacts at an early point in the beam RICH it is unlikely to satisfy the minimum requirement of 6 RICH hits. Also, these far-upstream interactions will be the easiest to reject based on tracking and vertex quality cuts. Far more dangerous is an interaction in the last beam tracker. Our cuts have been designed with effects such as this in mind. In particular the vertex $DOCA < 0.6$ cm cut and $20 \text{ m} < z_{\text{vertex}} < 40 \text{ m}$ (no vertex with 5 m of nearby material)

provide powerful rejection.

To pose a potential threat to CKM the K_L must have momentum above about 16 GeV, a fact we have determined with Monte Carlo studies. Fortunately this process is suppressed in CKM because any K^0 produced in an interaction with momentum close to the beam K^+ momentum is likely to carry the \bar{s} quark from the K^+ . This is equivalent to saying the dilution factor D is near unity in $K^+ \rightarrow K^0$ for high momentum K^0 's. It is $(1 - D)$ that figures in the background process in CKM. In that case it will mostly decay to $\pi^- e^+ \nu$ rather than $\pi^+ e^- \nu$ provided the decay occurs within the first several K_S lifetimes. For a typical case in CKM, a 19 GeV K^0 has $c\tau\gamma$ of about 1 m, so $\pi^+ e^- \nu$ decays are suppressed for decays within 10 m or so of the point of production.

The rejection of this background has been calculated in three pieces, all starting with a set of FRITIOF generated $K^+ \rightarrow K^0$ interactions. One piece is the probability for an event of this type to satisfy our analysis cuts on the K^+ and π^+ . Another piece is the probability for a photon, charged pion, or proton, to reach the Beam Interaction Veto System. The third piece is the probability that the electron in the event can be detected and provide the basis of a veto.

Initially we generated events in which the interaction took place anywhere in the material upstream of the decay volume. Figure 34 shows the z distribution of such events, with a flat region from -14 m to -4 m showing interactions in the beam RICH gas, a spike at -4 m corresponding to the beam RICH mirror, and two smaller spikes at -2 m and 0 m indicating the locations of the vacuum trackers. We verified that any background contribution from this source was dominated by interactions in the most downstream material. Specifically, applying only our vertex cuts to the events shown in figure 34 removes all events where the interaction occurred at upstream of the last beam vacuum tracker.

In fact the 2 m gap between the beam RICH and the vacuum trackers was introduced specifically to move beam RICH interactions upstream to a location where they were readily suppressed. A simulation of 2×10^6 events was run. After all cuts 277 events appear in the signal region. The Beam Interaction Veto System detects particles emerging from the last beam tracker at relatively large angles. Its purpose is to flag events where hadronic interactions occur in that tracker. We use the extra hadrons generated by FRITIOF to estimate the efficacy of this device in the same events. Using FRITIOF, we count photons with energy above 20 MeV into the BIVS, and hadrons reaching the BIVS within a 5 nsec time window (the limiting factor for detecting soft charged hadrons is not their energy, which is adequate, but the delay in their arrival because $\beta < 1$). Since detection of these types of particles should be fairly efficient, we can estimate the inefficiency of this device from the fraction of events where no associated particle intercepts the BIVS to be 3.5%.

The extra electron in these events can also be detected in most cases, providing additional rejection. A potential danger is that the very low-energy electrons will not be detected. They emerge from the decay at large laboratory angles and strike the Vacuum Veto System. For electron rejection we have followed the assumptions outlined in the discussion in section 3.4.5. That is, below 2 MeV an electron is lost, between 2 and 20 MeV it is detected with 90% efficiency, between 20 and 40 MeV it is detected with 99% efficiency, and above that the efficiency is the same as for photons. To estimate a rejection factor we have used the energy spectrum of the electrons weighted by these factors. The resulting rejection is 2×10^{-3} .

To estimate the effective branching ratio of this background we also need to account for the following factors: (1) the events are induced by undecayed beam K^+ 's (17% of 22 GeV K^+ 's decay in decay volume.) (2) the interaction probability in the relevant tracker is 4.0×10^{-4} , (3) the fraction of inelastic K^+ interactions that produce a K_L with sufficient momentum to induce this scenario (16 GeV from studying the events) is 0.012, (4) the K_L decay rate is a factor of 4.2 lower than the K^+ , (5) the mean momentum of the relevant K_L 's is about 19 GeV rather than 22 GeV, and (6) the $K_L \rightarrow \pi^+ e^- \nu$ branching ratio is 0.39/2. The various factors may be combined to provide an

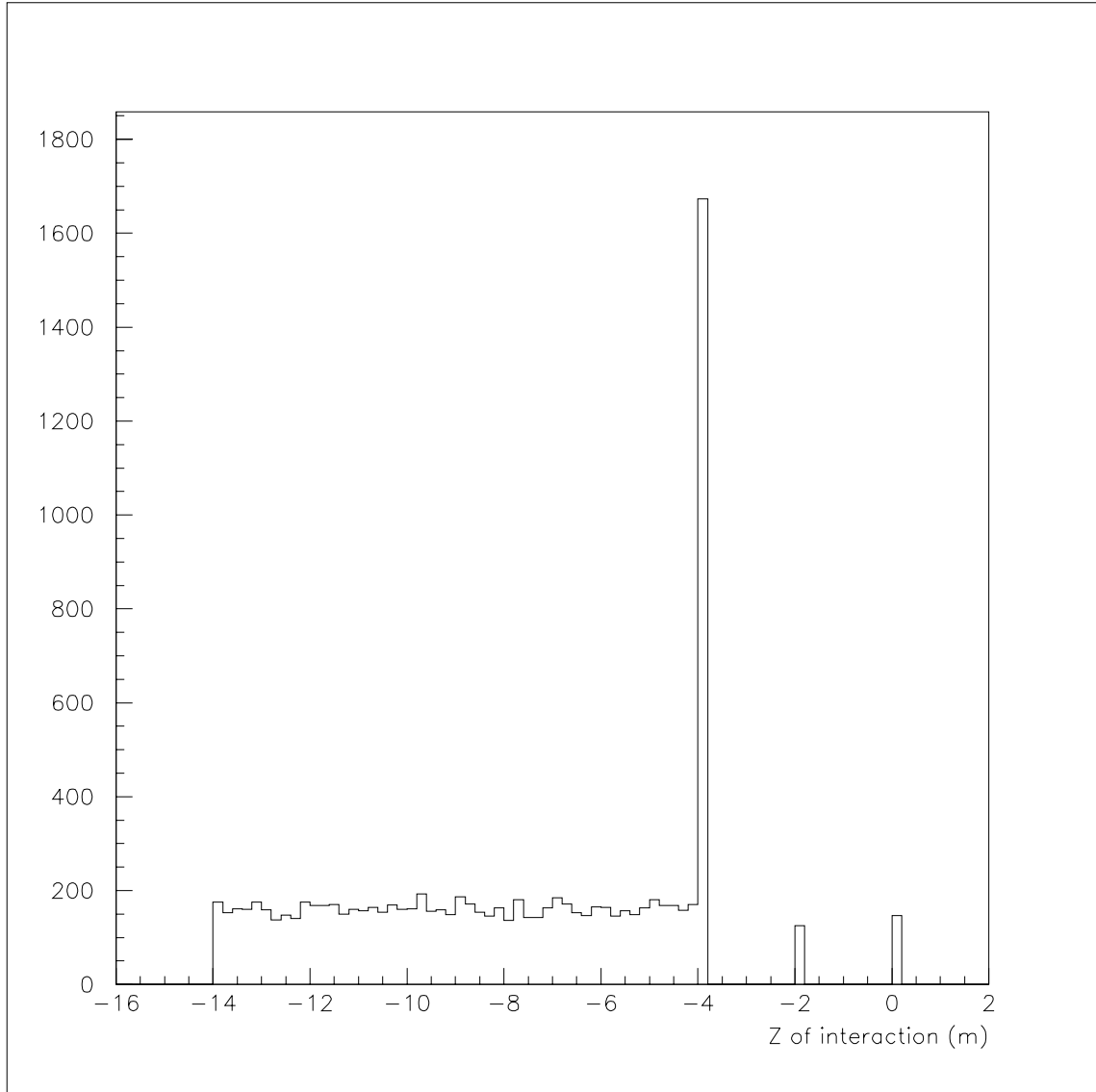


Figure 34: The location of 10,000 hadronic interactions in beamline material. In the z scale of this figure (not the same as figure 10) the beam RICH spans the range $-14\text{ m} < z < -4\text{ m}$, with the mirror located at $z = -4\text{ m}$. The two beam vacuum trackers are located at $z = -2\text{ m}$ and $z = 0$.

estimate of the effective branching ratio of this background scenario:

$$B_{\text{eff}} = \left(\frac{1}{0.018}\right) \left(\frac{1}{0.17}\right) (4 \times 10^{-4})(0.012) \left(\frac{0.17}{4.2}\right) \times \left(\frac{22}{19}\right) \left(\frac{0.39}{2}\right) \left(\frac{277}{2 \times 10^6}\right) (2 \times 10^{-3})(0.035) < 1.4 \times 10^{-13}. \quad (23)$$

We regard this as an upper bound because we have not included the suppression due to the dilution factor (the $(1 - D)$ effect). This will be significant since events which pass our vertex quality cuts are strongly biased toward the upstream part of the decay volume.

7.5.2 Other Interactions in Detectors

Other “window scattering” scenarios, i.e., hadronic interactions in the material immediate upstream and downstream of the decay volume, must be considered. The dominant scenario would be an inelastic beam K^+ interaction in either the last beam vacuum tracker or the first straw chamber that produces a fast forward π^+ which is a candidate for the π^+ from a signal event. For now we assume there is a beam hole in the first downstream straw chamber so K^+ ’s cannot interact in it. For K^+ interactions in the last beam vacuum tracker (KEAT) plane, substantial rejection comes from cuts on vertex quality and location ($DOCA < 0.6$ cm cut and $20 \text{ m} < z_{\text{vertex}} < 40 \text{ m}$, i.e., no vertex with 5 m of nearby material). Indeed, the only situation that leads to such an egregious mismeasurement of the vertex location occurs when the π^+ hadronically scatters in the first straw chamber so that the direction of the π^+ is corrupted.

This class of events is dominated by charge-exchange processes in the KEAT material where a fast forward pion is created as well as a moderate energy K^0 . In these events additional rejection comes from the BIVS because extra particles such as the exchange K^0 are usually produced along with the π^+ .

We have generated 2×10^5 events with a π^+ with momentum greater than 14 GeV, the minimum value allowed for the $K^+ \rightarrow \pi^+ \nu \bar{\nu}$ analysis, and a production angle less than 15 mrad. (The angular acceptance of the CKM detector, as simulated here, is about 13 mrad, defined by the size of the first straw chamber at a distance of 30 m from the production point. A typical hadronic p_T of 300 MeV at a momentum of 14 GeV corresponds to a 21 mrad production angle, which over the 30 m to the first straw tracker is 64 cm, far beyond the edge of the chamber.) In the Monte Carlo we force the π^+ to elastically scatter in the first straw tracker, an effect that should occur with probability of 2.8×10^{-4} . The estimation procedure for this background is similar to that for the charge exchange case. The additional pieces of information needed are: (1) the probability of an inelastic K^+ interaction producing a π^+ with $p > 14$ GeV with $\theta < 15$ mrad, which is 7.5×10^{-3} according to FRITIOF, (2) in this Monte Carlo sample events pass all cuts on the K^+ and π^+ and fall inside the signal region, and (3) the BIVS/VVS inefficiency for this class of interactions is at most 2.75%. Consequently, the effective branching ratio of this background scenario is:

$$B_{\text{eff}} = \left(\frac{1}{0.018}\right) \left(\frac{1}{0.17}\right) (4.0 \times 10^{-4})(7.5 \times 10^{-3})(2.8 \times 10^{-4}) \left(\frac{106}{2 \times 10^5}\right) (0.0275) < 4.0 \times 10^{-12}. \quad (24)$$

The interaction of a beam π^+ in the last vacuum tracker could also create a π^+ in the acceptance of the CKM detector. This is removed by the requirement placed on beam RICH hits. A pion far off-momentum (at about 6 GeV) could fake a K^+ , but it could not produce a 14 GeV pion in an interaction.

7.5.3 Beam Gas Interactions

An interaction of a K^+ with residual gas in the vacuum decay volume can produce a π^+ that falls into the acceptance of the CKM detector. Vertex quality cuts will not assist in rejecting these events. The best protection, of course, is a good vacuum. We assume 10^{-6} torr, which has been achieved in KTeV. Any such interaction will also produce other observable particles, and most beam gas interactions can be rejected on that basis.

The K^+ interaction length in air at 1 atm is about 470 m, so at 10^{-6} torr it is smaller by a factor of $10^{-6}/760 = 1.3 \times 10^{-9}$. Hence, the interaction probability in 30 m is

$$(1.3 \times 10^{-9}) \left(\frac{30}{470} \right) = 8.4 \times 10^{-11}. \quad (25)$$

We have simulated 12,000 beam gas interactions, using FRITIOF to generate K^+ interactions that produce a π^+ with $p > 14$ GeV. Of all K^+ interactions in FRITIOF, 2.5% produce such a π^+ . The interactions are generated flat in z between the last vacuum tracker and the first straw tracker. The events are subjected to the standard cuts, with 70 passing. Also, 48% of the interactions produce π^0 's for which the veto probability is effectively unity. The effective branching ratio of this background is then:

$$B_{\text{eff}} = \left(\frac{1}{\epsilon_{\pi\nu\nu}} \right) \left(\frac{1}{K^+ \text{ decay}} \right) (\text{prob interact})(\text{frac } p_\pi > 14 \text{ GeV})(\text{frac pass cuts})(\pi^0 \text{ rejection}) \quad (26)$$

$$B_{\text{eff}} = \left(\frac{1}{0.018} \right) \left(\frac{1}{0.17} \right) (8.4 \times 10^{-11})(0.025) \left(\frac{70}{12000} \right) (0.52) < 2.1 \times 10^{-12}. \quad (27)$$

We consider this to be a conservative upper limit since charged hadrons from beam gas interactions will also be used to veto.

7.6 Accidental Background Sources

By accidentals background we mean any process by which two beam particles conspire to fake $K^+ \rightarrow \pi^+ \nu \bar{\nu}$. The two beam particles must be close in time, yet one must go undetected. Both K^+ and π^+ will be detected by the beam RICH as well as the beam trackers, so the *a priori* probability is small for conditions to exist for an accidental background event to occur. Even if a K^+ or π^+ enters the decay volume undetected, there is no problem unless it decays. If a π^+ decays, it almost always produces a muon, for which CKM has enormous rejection. The detected K^+ must also decay, since we will veto events with beam particles in-time with $K^+ \rightarrow \pi^+ \nu \bar{\nu}$ candidates. We can project the K^+ trajectory from the beam vacuum trackers to the scintillating fiber tracker which spans the beam and make a requirement that no beam particle consistent with a non-decayed K^+ appear. Even if the scintillating fiber tracker suffers some level of inefficiency, the Charged Veto Plane will also have a shot at it, making a complete miss unlikely.

Thus we are led to conclude two K^+ decays are the most plausible candidate accidental background. To be outside the scope of prior estimates, the event must be confused by associating the π^+ from one decay (the undetected K^+) with the the detected K^+ , whose decay products must escape completely unnoticed. One can imagine a $K^+ \rightarrow \mu^+ \nu_\mu$ decay where the muon is very low-energy in the laboratory. Then the undetected K^+ should decay via $K^+ \rightarrow \pi^+ \pi^0$ or $K^+ \rightarrow \pi^+ \pi^+ \pi^-$ in order to provide a π^+ candidate. However, one can see from figure 3 that $K^+ \rightarrow \pi^+ \pi^+ \pi^-$ cannot produce a π^+ with $p > 14$ GeV, so we will focus on $K^+ \rightarrow \pi^+ \pi^0$.

So, we need: (1) the probability of detecting only one of two K^+ 's that enter CKM close in time, (2) the probability that one will decay with no observed products, and (3) the probability that

a $K^+ \rightarrow \pi^+\pi^0$ decay will pass all cuts when its kinematics are corrupted by using the wrong beam K^+ .

It is reasonable to take the probability of a second K^+ in-time with the first to be about 1 nsec / 30 nsec, roughly the timing resolution divided by the time between K^+ 's on average. Also, we expect a tracking inefficiency of about 0.1% for beam particles due to algorithm inefficiencies (silicon is intrinsically very efficient). Also, we will reject events in which the beam RICH has too many hits, above 20, which rejects about half of these events. Thus, we take factor (1) to be 1.7×10^{-5} .

For factor (2) we have simulated $K^+ \rightarrow \mu^+\nu_\mu$ events to determine the fraction of decays where a muon (for which the minimum momentum is 1 GeV in 22 GeV K^+ decays) below RICH threshold misses both the Vacuum Veto System and the Forward Veto System. This is a conservative estimate since we do not utilize available tracker information. With this fraction, 9.5%, we estimate factor (2) to be $(0.21)(0.64)(0.095) = 0.013$. The first factor is the decay probability upstream of the scintillating fiber tracker and the second is the branching ratio.

To evaluate factor (3) we have used the Monte Carlo and simply calculated all quantities from one $K^+ \rightarrow \pi^+\pi^0$ decay mixed with another beam K^+ . We have generated 5×10^6 such events and found that 1288 events pass all cuts on the (wrong) K^+ and π^+ and fall in the signal region. Of course the π^0 in these events provides addition rejection. We have determined the π^0 rejection for these events using the same method described earlier. The rejection is not as good as in a correctly measured event, since there is some probability that the decay occurs farther downstream than $z = 25$ m, making it possible for photons to escape at wide angles out the side of the pion RICH. The π^0 rejection of these events is found to be 3.3×10^{-4} .

These factors can be combined to obtain an estimate of the effective branching ratio of the accidentals background:

$$B_{\text{eff}} = \left(\frac{1}{\epsilon_{\pi\nu\nu}} \right) (B(K^+ \rightarrow \pi^+\pi^0)) (\text{prob miss 2nd } K) \times (\text{prob miss } K^+ \rightarrow \mu^+\nu_\mu) (\text{frac pass cuts}) (\pi^0 \text{ rejection}) \quad (28)$$

$$B_{\text{eff}} = \left(\frac{1}{0.018} \right) (0.21)(1.7 \times 10^{-5})(0.012) \left(\frac{1288}{2 \times 10^6} \right) (3.3 \times 10^{-4}) = 5.1 \times 10^{-13}. \quad (29)$$

Clearly this is in many respects an imperfect estimate. The point of it is that with reasonable assumptions a plausible accidental scenario does not pose a problem. That does not prove some scenario which has been overlooked cannot pose a problem, but it indicates that accidentals do not seem to be an area of special danger.

7.7 Background Summary

We collect the background estimates made in earlier sections in table 20. Our conclusion is that $K^+ \rightarrow \pi^+\pi^0$ decays and tracker-window beam interactions are the most challenging. We must clearly work hard to maintain our specs for kinematic resolution, photon veto rejection, and the ability to veto particles associated in beam interactions with detector material.

At this point we will identify the two areas where our background simulations seem to us the weakest:

1. We do not simulate the tracking problem. That is, we do not generate hits in trackers along with noise hits and then reconstruct tracks. When this is done mistakes can occur that we do not account for in the current methodology. Also, non-Gaussian resolution effects need to be investigated and may need to be included.

Background Source	Effective BR ($\times 10^{-12}$)
$K^+ \rightarrow \mu^+ \nu_\mu$	< 0.04
$K^+ \rightarrow \pi^+ \pi^0$	3.7
$K^+ \rightarrow \mu^+ \nu_\mu \gamma$	< 0.09
$K^+ A \rightarrow K_L X$ followed by $K_L \rightarrow \pi^+ e^- \nu$	< 0.14
$K^+ A \rightarrow \pi^+ X$ in trackers	< 4.0
$K^+ A \rightarrow \pi^+ X$ in residual gas (10^{-6} torr)	< 2.1
Accidentals (2 K^+ decays)	0.51
Total	< 10.6

Table 20: Background estimates in terms of effective branching ratio.

2. We have not compared FRITIOF results to those of another hadronic interaction generator. We have found however that the predictions of FRITIOF generally agree with published measured inclusive data for K^0 production and π^+ production. We do not expect the range of possible errors to be large, but comparisons with other generators are an obvious check we have not yet carried out. The estimate of the $K^+ \rightarrow \pi^+ \pi^0$ background does not rely on FRITIOF in any way.

We expect the quality of our studies will be improved over time and that we will be able to assuage the concerns of a skeptical reviewer before any metal is cut.

Finally, it should be emphasized that an important aspect of CKM is the ability to enhance interaction-induced backgrounds in a controlled way by increasing the material in the path of particles. This provides an extremely powerful tool for measuring backgrounds.

8 Cost, Schedule and Staffing Estimates

8.1 Costs

In the absence of detailed of engineering designs it is impossible to give precise cost estimates. Despite this, we have made an effort to estimate the capital costs for the detector elements of the CKM experiment based on the recent experience of the KTeV project, the SELEX experiment, and experiment 871 and Brookhaven. The costs below do not include engineering costs, SWF, or contingency. These estimates at this point serve only as a guide for the detector costs of the CKM experiment.

8.1.1 Beam Time Stamp System Costs

The beam time stamp fiber tracker cost is estimated based upon our understanding of the per channel costs for the Dzero fiber tracker. The cryogenic infrastructure is a significant expense for this system that unfortunately cannot be shared with the other two VLPC systems in the apparatus due to the distance between them. We are considering other scintillator-based taggers for the BTS and the CVP described below to reduce this cost. For the purposes of the proposal however, we are including the cost of three separate sets of cryogenic infrastructure for the BTS, the DMS fiber-plane, and the downstream Conversion Veto Plane (CVP).

Beam Time Stamp System			
Item	Unit cost	No. of Unit	Total
VLPC	\$25/ch	600	\$15K
Preamp & TMC	\$50/ch	600	\$30K
Fiber plane & supports	\$10K	1	\$10K
Cryogenic infrastructure	\$250K	1	\$250K
Optical cables	\$10K	1	\$10K
Vacuum components	\$20K	1	\$20K
Total cost			\$335K

Table 21: Cost Breakdown of the Beam Time Stamp System.

8.1.2 Upstream Magnetic Spectrometer Costs

The upstream magnetic spectrometer cost is estimated based upon the Selex silicon system for detectors and our understanding of the per channel costs for the CDF SVX3 electronics. The magnet is part of the beamline and costed there.

Upstream Magnetic Spectrometer			
Item	Unit cost	Amount	Total
Silicon Detector plane.	\$10K/plane	4	\$40K
SVX3 readout.	\$5/channel	16K	\$80K
Vacuum system/supports.	\$50K	1	\$50K
Magnet	FNAL stock	1	—
Total Cost			\$170K

Table 22: Cost Breakdown for the Upstream Magnetic Spectrometer.

8.1.3 Kaon RICH Costs

The kaon RICH cost is estimated based upon the Selex RICH and our assumed TMC per channel cost for a time measurement on each channel.

8.1.4 Kaon Entrance Angle Tracker Costs

The kaon entrance angle tracker costs are estimated on the same basis as the upstream magnetic spectrometer.

8.1.5 Beam Interaction Veto System and Vacuum Veto System Costs

The beam interaction veto system and Vacuum veto system are both lead scintillator shower counters with design and costs based upon work done by KAMI. The vacuum tank cost is an extrapolation based upon the KTeV vacuum decay tank.

Kaon RICH			
Item	Unit cost	Amount	Total
Optics and Vessel	\$60K	1	\$60K
Gas System	\$70K	1	\$70K
Phototubes	\$350	549	\$188K
High Voltage	\$50	549	\$27K
TMC readout	\$25	549	\$14K
Total Cost			\$359K

Table 23: Cost Breakdown for the Kaon RICH.

Kaon Entrance Angle Tracker			
Item	Unit cost	Amount	Total
Silicon Detector plane.	\$10K/plane	2	\$20K
SVX3 readout.	\$5/channel	8K	\$40K
Vacuum system/supports.	\$50K	1	\$20K
Total Cost			\$80K

Table 24: Cost Breakdown for the Kaon Entrance Angle Tracker.

Beam Interaction Veto System			
Item	Unit cost	Amount	Total
Plastic Scinti.(5 mm t)	\$6k/ton	5 ton	\$30K
Lead Sheet (1 mm t)	\$3k/ton	9 ton	\$27K
WLS Fiber (1 mm ϕ)	\$0.8/m	70 km	\$56K
Photo tube (2" ,Linear)	\$350/tube	200	\$70K
QIE-TMC readout	\$75/channel	200	\$15K
High Voltage	\$50/channel	200	& 10K
Structures.			\$20K
Total Cost			\$228K

Table 25: Cost Breakdown for the Beam Interaction Veto System.

Vacuum Veto System			
Item	Unit cost	Amount	Total
Plastic Scinti.(5 mm t)	\$6k/ton	40 ton	\$240K
Lead Sheet (1 mm t)	\$3k/ton	80 ton	\$240K
WLS Fiber (1 mm ϕ)	\$0.8/m	600 km	\$480K
Photo tube (2" ,Linear)	\$350/tube	1320	\$460K
Photo tube (2" , FM)	\$1000/tube	120	\$120K
QIE-TMC readout	\$75/channel	1440	\$108K
High Voltage	\$50/channel	1440	\$72K
Vacuum tank etc.			\$1000K
Total Cost			\$2720K

Table 26: Cost Breakdown for the Vacuum Veto System.

8.1.6 Downstream Magnetic Spectrometer Costs

The downstream magnetic spectrometer costs are estimated based upon on the BNL E791/E871 straw tube system. The maximal system is costed, 4 stations of xx'yy'uu'vv' straw planes in the vacuum and a full coverage xx'yy' fiber station downstream of the vacuum window. The spectrometer magnet cost is based upon the cost of the KTeV magnet.

Downstream Magnetic Spectrometer			
Item	Unit cost	No. of Unit	Total
Straw Drift tubes	\$50/ch	8000	\$400K
Straw vacuum flanges	\$100K	4	\$400K
Straw Preamps & TMC	\$75/ch	8000	\$600K
VLPC fiber readout	\$25/ch	4000	\$100K
VLPC Preamp & TMC	\$50/ch	4000	\$200K
Fiber plane etc.	\$50K/module	1	\$50K
Optical cables	\$50K/module	1	\$50K
Spectrometer Magnet	\$300K	1	\$300K
Total cost			\$2100K

Table 27: Cost Breakdown of the Downstream Magnetic Spectrometer System.

8.1.7 Pion RICH Costs

The kaon RICH costs is estimated based upon the Selex RICH and our assumed TMC per channel cost for a time measurement on each channel.

8.1.8 Forward Veto System (Shashlik) Costs

The forward veto system costs is estimated based upon the Phenix shashlik calorimeter. We have done the breakdown of costs based upon the total cost of their system [62]. Electronics costs are

Pion RICH			
Item	Unit cost	Amount	Total
Optics and Vessel	\$150K	1	\$150K
Gas System	\$100K	1	\$100K
Phototubes	\$350	3000	\$1050K
High Voltage	\$50	3000	\$150K
TMC readout	\$25	3000	\$75K
Total Cost			\$1525K

Table 28: Cost Breakdown for the pion RICH.

based upon KTeV experience with QIE and our assumed TMC cost.

Forward Veto System (Shashlik)			
Item	Unit cost	Amount	Total
Plastic Scinti.(4 mm t)	\$100k/ton	1.2 ton	\$120K
Lead Sheet (1.5 mm t)	\$50k/ton	2.4 ton	\$120K
WLS Fiber (1 mm ϕ)	\$2.3/m	22 km	\$50K
Photo tube (2" ,Linear)	\$350/tube	1242	\$435K
QIE-TMC readout	\$75/channel	1242	\$93K
High Voltage	\$50/channel	1242	\$62K
Mechanical structures	\$100K	1	\$100K
Total Cost			\$980K

Table 29: Cost Breakdown for the Forward Veto System, (assuming Shashlik).

8.1.9 Conversion Veto Plane Costs

The conversion veto plane costs are estimated on the same basis as the upstream magnetic spectrometer.

8.1.10 Muon Veto System Costs

The muon veto system cost is estimated based upon our understanding of the costs of appropriate scintillator and phototubes. The electronics costs are on the same basis as the beam and vacuum veto systems.

8.1.11 Hole Veto System, SHASHLIK design, Costs

The hole veto system cost is estimated on the same basis as the forward veto system.

8.1.12 Summary of Detector Cost Estimates

The summary and total of all costs enumerated above is in Table 33.

Conversion Veto Plane			
Item	Unit cost	No. of Unit	Total
VLPC	\$25/ch	600	\$15K
Preamplifier & TMC	\$50/ch	600	\$30K
Fiber plane & supports	\$10K	1	\$10K
Cryogenic infrastructure	\$250K	1	\$250K
Optical cables	\$10K	1	\$10K
Total cost			\$315K

Table 30: Cost Breakdown of the Conversion Veto Plane System.

Muon Veto System			
Item	Unit cost	Amount	Total
Plastic Scinti.(1 cm)	\$100	1000	\$100K
Fe Slabs (4 cm * 2 m * 2 m)	\$4K	25	\$100K
Photo tube (2" ,Linear)	\$100/tube	1000	\$100K
QIE-TMC readout	\$75/channel	1000	\$75K
High Voltage	\$50/channel	1000	\$50K
Mechanical structures	\$50K	1	\$50K
Total Cost			\$475K

Table 31: Cost Breakdown for the Muon Veto System.

Hole Veto System, SHASHLIK design			
Item	Unit cost	Amount	Total
Plastic Scinti.(4 mm t)	\$100k/ton	—	\$20K
Lead Sheet (1.5 mm t)	\$50k/ton	—	\$10K
WLS Fiber (1 mm ϕ)	\$2.3/m	—	\$5K
Photo tube (2" ,Linear)	\$350/tube	50	\$18K
QIE-TMC readout	\$75/channel	50	\$4K
High Voltage	\$50/channel	50	\$3K
Mechanical structures	\$100K	1	\$10K
Total Cost			\$70K

Table 32: Cost Breakdown for the Hole Veto System.

Summary of Detector Cost Estimates	
Detector System	Sub-cost.
BTS System	\$335K
UMS System	\$170K
Kaon RICH	\$359K
KEAT System	\$80K
BIV System	\$228K
VVS System	\$2720K
DMS System	\$2100K
Pion RICH	\$1525K
FVS System	\$980K
MVS System	\$475K
CVP System	\$315K
HVS System	\$70K
Trigger System	\$300K
DAQ System	\$700K
Total	\$10357K

Table 33: Cost estimate of the CKM detector systems.

8.1.13 Fermilab Facility Cost Estimates

We are told that the estimated cost for the RF separated beamline totals \$4000K. There will be costs associated with siting the experiment. Any estimate of these costs awaits a definite location for the experiment and a siting plan.

8.2 Milestones

The major milestones required to achieve the publication of a measurement of the magnitude V_{td} with the CKM experiment are identify in this section. These are serial activities as arranged here so the total time required will be no less than the sum of the times given here. The actual time line will be longer than this total; contingent upon the availability of funds, technical resources and the beam line. The pace of work we assume here is a full lab effort, as was achieved for KTeV and is now underway for the CDF and Dzero upgrades.

8.2.1 First stage (physics) approval — 0.5 years

This proposal seeks an approval based upon the physics interest in the measurement of the $K^+ \rightarrow \pi^+ \nu \bar{\nu}$ branching ratio and sufficient confidence in the decay in flight technique we are advocating to justify the investment required to produce a complete design and cost estimate for the experiment. We hope that the PAC and the laboratory will look favorably upon this proposal in a timely manner.

8.2.2 Second stage (technical and budgetary) approval — 1.5 year

Our plan is to produce a complete design and cost estimate for the experiment and obtain second stage approval before proceeding further. This will require design work involving both physicists and engineers. All the detector technologies we are considering are proven in that they have been, or will be, used successfully in previous experiments. We need to do detector development and engineering but not detector research. Some construction and testing of prototypes to establish the actual performance characteristics of critical detector systems will be required.

8.2.3 Experiment construction — 2 years

This proposal requires a new experimental apparatus. The plan is to site the experiment in an existing experimental area so no new civil construction should be required to house the apparatus. This apparatus can be constructed and brought to the point where it is ready for beam in 2 years after second stage approval of the design if the project is given levels of lab support and effort comparable to present major laboratory projects.

The beam line for this experiment is a new laboratory facility. The design of the beam line is currently organized as a project in the Beams Division. As one of the first users of this new beam line we see our role as defining technical requirements for the beam and participating at an appropriate level in it's design, construction and commissioning. We have not considered the cost and schedule of the beam line in this proposal beyond this level of participation.

8.2.4 Engineering run — 0.5 years

A new apparatus will require one or more iterations in order to achieve and demonstrate the required sensitivity per hour of beam with the required background rejection. The model of operation of the Main Injector, with beam available most of the time, will allow us to intermix engineering data taking, analysis and detector modifications as necessary in order to achieve the design goals in a time optimum manner.

8.2.5 Data taking — 2 years

With our present understanding of the acceptance and rate capability of the apparatus we are proposing it will take two years of data taking to achieve a single events sensitivity of 1.4×10^{-12} or

72 $K^+ \rightarrow \pi^+ \nu \bar{\nu}$ events at a branching ratio of 1×10^{-10} . The number of protons required to produce the required kaon flux amount to 15% of the Main Injector initial design intensity. This proposal is not a significant impact, in terms of proton economics, on either the production of anti-protons for the collider program or on the Main Injector neutrino program. Its fundamental rate limitations are its own capabilities to handle kaon flux.

8.2.6 Analysis and publication — 1.5 years

This experiment is designed with a software filter for the last level of trigger decision. The model is to use an initial version of the off-line analysis to implement this level of trigger decision. As such, the analysis of these data will begin with the engineering data. Based upon experience from previous experiments of this type we estimate 1.5 years of analysis time will be required after data taking ends before we will be in position to publish a result for the $K^+ \rightarrow \pi^+ \nu \bar{\nu}$ branching ratio.

8.3 Staffing

Our list of proponents is dominated by physicists with significant experience in doing rare and ultra-rare kaon decay experiments of this kind. When the university and laboratory groups represented fill out with younger physicists and students we will have a significant fraction of the physics staff required to carry out this experiment. We will need to grow by at least a few more university groups in order to have the necessary physics strength to carry this experiment through to completion. One or two of these groups will need to be or become large enough and strong enough to undertake significant technical roles in the design and construction of the experiment.

We have had some discussions with potentially interested groups. There seems to be no lack of interest in CKM. university groups have difficulty in joining an effort, such as ours, before it gains official recognition. First stage approval of this proposal is all we believe we require in order to strengthen our collaboration up to a level sufficient to produce a complete and credible design and cost for the experiment. The staffing of the experiment at the engineering and technical levels will require negotiation with the laboratory at an appropriate time.

9 Conclusion

The measurement of the $K^+ \rightarrow \pi^+ \nu \bar{\nu}$ branching ratio to the 10% level of statistical precision which we are proposing is a critical next step in advancing our understanding of the source of CP violation in nature.

The decay in flight technique we advocate is a departure from all previous experiments searching for $K^+ \rightarrow \pi^+ \nu \bar{\nu}$. With this technique we believe that we can make a large advance in sensitivity and achieve the first measurement with precision of the rate of this important process.

The goal we set for CKM was to observe 100 $K^+ \rightarrow \pi^+ \nu \bar{\nu}$ events with less than 10% background in two years of data taking. This proposal achieves 72 signal events with less than 7.6 background events with the experiment described here. This corresponds to 1.4×10^{-12} single event sensitivity and we assume a signal branching ratio of 1×10^{-10} . 100 events provide a total error on V_{td} of 10%, 72 events provide a 10.5% measurement. With further refinements as the experimental design evolves we still hope to achieve this goal. Either way this experiment will make the definitive measurement of V_{td} we are after.

The Gilman HEAPAP sub-panel report recommends that: "...experiments with intense K and muon beams 'be approved' on the recommendation of the members of a single advisory body to

the Division of High Energy Physics when full proposals are available". We fully support this recommendation.

A first stage approval of this proposal is necessary for two reasons; to give us access to sufficient resources to allow us to proceed with a complete design and cost estimate for this experiment and to attract more groups to the experiment. With these inputs to second stage Fermilab approval in place we will be prepared to face whatever committee is convened to review our proposal in a national forum.

10 Acknowledgements

The evolution of this proposal has and continues to be fueled by lively and fruitful discussion with our colleagues in BNL-787. In particular, discussions with L. Littenberg and M. Diwan of Brookhaven National Laboratory have been very helpful and insightful. We also wish to acknowledge many useful and formative discussions with our KAMI colleagues who face similar technical challenges. Most notable among these is the design of an ultra-hermetic photon veto system, where we have adopted the KAMI design pioneered by K. Arisaka and his colleagues at UCLA. Our studies and consideration of fiber readout technology have been helped greatly by discussions with Alan Bross, Ron Ray and their D0 colleagues at Fermilab. In addition, we wish to thank S. Striganov of IHEP/Protvino for GEANT simulations studies crucial to the design of the Muon Veto System. The physics reach of this proposal relies entirely on the existence of a high purity charged kaon beam. We are grateful for the efforts of our CP/T colleagues and the Fermilab Beams Division who have been studying the feasibility and have been leading the R&D effort for this beam line.

References

- [1] G. Buchalla and A.J. Buras, Phys. Rev. **D54**, 6782 (1996).
- [2] D. Rein and L.M. Sehgal, Phys. Rev. **D39**, 3325 (1989).
- [3] J.S. Hagelin and L.S. Littenberg, Prog. Part. Nucl. Phys. **23**, 1 (1989).
- [4] M. Lu and M. Wise, Phys. Lett. **B324**, 461 (1994).
- [5] S. Fajfer, Nuovo Cim. 110 A, 397 (1997).
- [6] S. Adler, et.al., Phys. Rev. Lett. **79**, 2204 (1997).
- [7] Inami and C.S. Lim, Prog.Theor. Phys. **65**, 297 (1981).
- [8] J. Ellis and J.S.Hagelin, Physics Letter **B192**, 201 (1983).
- [9] J. Ellis and J.S. Hagelin, Nucl. Phys. **B217**, 189 (1983).
- [10] C.O. Dib, I. Dunietz and F.J. Gilman, Mod. Phys. Lett. **A6**, 3573 (1991).
- [11] W. Marciano and Z. Parsa, Phys. Rev. **D53**, R1 (1996).
- [12] G. Buchalla and A.J. Buras, Nucl. Phys. **B412**, 106 (1994).
- [13] A. J. Buras hep-ph/9711217, TUM-HEP-299/97, October 1997 (To appear in the proceedings of the Symposium on Heavy Flavours, Santa Barbara, July 7-11,1997).

- [14] $\bar{\rho} = \rho[1 - \lambda^2/2]$, $\bar{\eta} = \eta[1 - \lambda^2/2]$ with ρ and η the usual Wolfenstein parameters. L. Wolfenstein, Phys. Rev. Lett. **51**, 1945 (1983).
- [15] A. J. Buras and R. Fleischer, hep-ph/9704376, April 1997 (To appear in “Heavy Flavors II”, World Scientific, 1997).
- [16] Tsuyoshi Nakaya, (To appear in the proceedings of the Symposium on Heavy Flavours, Santa Barbara, July 7-11,1997).
- [17] L. Littenberg, public communication.
- [18] J. Bijnens, G. Ecker, J. Gasser, Nucl. Phys. B396, 87 (1993).
- [19] D. A. Bryman, P. Depommier, C. Leroy, Phys. Reports 88 (1982) 151.
- [20] J. Heintze *et al.*, Nucl. Phys. B149, 365 (1979).
- [21] Y. Akiba *et al.*, Phys. Rev. D32, 2911 (1985).
- [22] V. S. Demidov *et al.*, Sov. J. Nucl. Phys. 52, 1006 (1990).
- [23] M. R. Convery, Princeton University, UMI-97-07305, Ph.D. Thesis (1996).
- [24] M. R. Convery, Proceeding of the 1996 Minneapolis DPF Conference.
- [25] C. Milstene *et al.*, presented at the Fermilab Main Injector Workshop, May 1997, hep-ex/9803033.
- [26] The second DAFNE physics handbook, v. 1, IFNF, Frascati, 1995.
- [27] E. Shabalin, Pis'ma Zh.Eksp.Theor.Fiz., **22**, 117 (1975).
- [28] C. Alliegro, et al., Phys. Rev. Lett. **68**, 278 (1992).
- [29] S. Adler, et al., Phys. Rev. Lett. **79**, 4756 (1997).
- [30] L. Okun, Leptons and Quarks, North Holland (1982).
- [31] H. Leutwyler, M. Roos, Z. Phys. **C25** 25 (1984).
- [32] T. Kycia, B. Nefkens et al., AGS proposal E927 for the Crystal Ball experiment, September 1996.
- [33] Paul Mackenzie and Andreas Kronfeld, Fermilab, private communication.
- [34] S. Adler, et al., Phys. Rev. Lett. **79**, 4079 (1997).
- [35] A.A. Belkov, et al., Phys. Lett. **B249**, 325 (1990).
- [36] C. Bruno, J. Prades, Z. Phys. **C57** 585 (1993). S. Herzlich, J. Kalinowski, Nucl. Phys. **B381**, 501 (1992).
- [37] G. D'Ambrosio and G. Isidori, Int. Journal of Modern Physics **A79**, 1 (1998).
- [38] Review of Particle Properties, R.M. Barnett et al., Physical Review **D54** 1, (1996).

- [39] “Report of the Working Group on K^+ Decay in-Flight”, Collins, et al., from the “Proceedings of the Workshop on Physics at the Main Injector”, May 16th, 1989.
- [40] The first large phototube based RICH system that we are aware of was employed in the SPHINX experiment. D. Vavilov et al. *Yad. Fiz* **57**, 241 (1994) (in Russian), translation, *Phys.At.Nucl*, **57**, 227 (1994).
- [41] E. Cheu *et al.*, “An Expression of Interest to Detect and Measure the Direct CP Violating Decay $K_L \rightarrow \pi^0 \nu \bar{\nu}$ and Other Rare Decays at Fermilab Using the Main Injector,” Fermilab-Pub-97-321-E.
- [42] T. Inagaki *et al.*, “Measurement of the $K_L \rightarrow \pi^0 \nu \bar{\nu}$ decay,” KEK proposal, (June 1996).
- [43] B. Rossi and K. Greisen, *Rev. Mod. Physics*, textbf13, 240 (1941).
- [44] Evidence for the decay $K^+ \rightarrow \pi^+ \nu \bar{\nu}$ E787 Collaboration (BNL-KEK-Princeton-Osaka-TRIUMF-Alberta): S. Adler, et al *Phys.Rev.Lett.* 79 (1997) 2204-2207
- [45] L. Littenberg, BNL E787, private communication.
- [46] J. Doornbos et al, “Optics design of 25 GeV/c RF separated K^+ beam”, Fermilab TM in preparation.
- [47] The “MIST” workshop was held in May of 1997 and focused on the fixed target physics opportunities with the Fermilab Main Injector. Proceeding of the Workshop on Fixed Target Physics at the Main Injector, G.J. Bock and J.G. Morfin, ed., Fermilab-Conf-97/279 (1997).
- [48] Discussions with Phil Martin and Chandra Bhat at the “Workshop on Fixed Target Physics at the Main Injector”, May 1-4,1997.
- [49] BNL E777, C. F. Campagnari, Ph.D. thesis, Yale University (1988).
- [50] A. Brenner et al, *Phys.Rev.* D26,1497,(1982).
- [51] A.J.Malensek,Fermilab FN-341, Oct.1981.
- [52] A. Citron et al, *Nucl. Instr. and Meth.* 155(1978)93-96 and A. Citron et al, *Nucl. Instr. and Meth.* 164(1979) 31-55.
- [53] W.K.H. Panofsky, Stanford Report HEPL-82 (1956).
- [54] B.W. Montague, CERN Internal Report PS/Int.AR/PSep/60-1 (1960).
- [55] W. Schnell, CERN 61-5 (1961).
- [56] AGS 1965 rf sep.beam to 80” Bubble Chamber 12.8 GeV/c.
- [57] P. Bramham et al, *Physics Letters* 15, 290 (1965).
- [58] P. Bernard et al, *Proc.Int.Conf. on High-Energy Accelerators*, Cambridge (1967), 190.
- [59] P. Bernard et al, CERN 68-29,1-61 (1968).
- [60] A. Moretti, Feasibility of RF Separator Cavities for the CP/T experiment presented at Workshop on Fixed Target Physics at the Main Injector

- [61] T. Kobilarcik, Fermilab external beam's group, private communication.
- [62] Herman White's presentation to the to January 1998 Fermilab PAC meeting.
- [63] G. Thomson, Private communication.
- [64] P. Mathew, et al. NIM article in preparation on the SELEX silicon tracker system.
- [65] D.C. Christain et al., FERMILAB-PUB-93-160, Jun 1993, Nucl.Instrum.Meth. **A345**, 62 (1994).
- [66] M.P. Maia et al., Nucl.Instrum.Meth.,**A326**, 496 (1993).
- [67] J. Engelfried et al., FERMILAB-CONF-97/210, accepted for publication in Nucl. Instr. and Meth.
- [68] J. Engelfried et al., to be published in Nucl. Instr. and Meth.
- [69] A. Bideau-Mehu, PhD Thesis University Brest (France) 1982, unpublished
- [70] J.Koch *Über die Dispersion des Lichtes in gasförmigen Körpern innerhalb des ultravioletten Spektrums*. Ark. Mat. Astr. Fys. 9(1913) Nr. 6, 1-11.
- [71] R. Abjean, A. Bideau-Mehu and Y. Guern, Nucl. Instr. and Meth. A 292 (1990) 593-594
- [72] Hamamatsu Photomultiplier Catalog.
- [73] J. Ritchie, BNL E871, private communication.
- [74] R. Ruchti, Nuclear Physics **B44** (Proc. Suppl.), 308 (1995).
- [75] First results on the spaghetti calorimeter projective prototype., A. Contin et al., Nucl.Instrum.Meth.A315:354-361,1992 (No.8)
Recent results from the spaghetti calorimeter project. R. Wigmans, Nucl.Instrum.Meth. **A315**,299 (1992) (No.8)
Results of prototype studies for a spaghetti calorimeter. D. Acosta et al., Nucl.Instrum.Meth. **A294**, 193 (1990).
Performance of a scintillating fibers/lead calorimeter. By SPACAL Collaboration (A. Ereditato for the collaboration). 1990. In *San Miniato 1990, Experimental apparatus for high energy particle physics and astrophysics*143-155.
- [76] A scintillator - lead photon calorimeter using optical fiber readout. H. Fessler et al., Nucl.Instrum.Meth. **A240**, 284 (1985).
Lead scintillator electromagnetic calorimeter with wavelength shifting fiber readout. G.S. Atayan et al., Nucl.Instrum.Meth. **A320**, 144 (1992).
- [77] The H1 lead / scintillating fiber calorimeter. H1 SPACAL Group (R.D. Appuhn et al.). DESY-96-171, Aug 1996. 24pp. Nucl.Instrum.Meth. **A386**, 397 (1997).
Hadronic response and e / pi separation with the H1 lead / fiber calorimeter. H1 SPACAL GROUP (R.D. Appuhn et al.). DESY-95-250, Dec 1995. 33pp. Nucl.Instrum.Meth. **A382**, 395 (1996).

Performance of an electromagnetic lead / scintillating fiber calorimeter for the H1 detector. H1 SPACAL Group (T. Nicholls et al.). DESY-95-165, Sep 1995. 16pp. Nucl.Instrum.Meth. **A374**, 149 (1996).

[78] Draft preprint in preparation, courtesy of S. White, BNL.

[79] Fermilab Technical Memo in preparation.

[80] A vme 32-channel pipeline tdc module with tmc lsis. IEEE Trans.Nucl.Sci. bf431799(1996). Conceptual design of straw tube readout with tmc. By SDC Collaboration (Y. Arai et al.). SDC-91-00063, Aug 1991. 39pp.

[81] Atlas detector at LHC/CERN design report.

[82] The performance of a high speed pipelined photomultiplier readout system in the fermilab KTEV experiment. By Juliana Whitmore (Fermilab). FERMILAB-CONF-97-272, Aug 1997. 6pp. To be published in the proceedings of 7th Pisa Meeting on Advanced Detector: Frontier Detectors for Frontier Physics, La Biodola, Isola d'Elba, Italy, 25-31 May 1997.

[83] A. Schiz et al, Phys.Rev. D21,3010,(1980).

[84] Computer Physics Communications, North-Holland Volume 71 (1992) P. 173